Università degli Studi "Roma Tre"

DIPARTIMENTO DI MATEMATICA E FISICA

MASTER'S THESIS IN PHYSICS

Dark Matter Direct Detection with DarkSide-50: Analysis of Early Data.

Student: Laura Marini

Supervisor: Prof. Stefano Maria Mari

External supervisor: Prof. Luca Grandi

Academic Year 2012 - 2013

Science is made up of data, like a house of stones.
But a pile of data is not science any more than a heap of stones is a house.

Henri Poincaré, *Science and Hypothesis*, 1902

Contents

Introduction

The nature of Dark Matter (DM) is one of the most important open problems in modern cosmology and particle physics. The existence of DM is known because of its gravitational effects at both galactic and galactic cluster scales, and it has accounted for the missing matter in the Universe. However, beside its obvious implications on an astrophysical scale, DM is not less important for particle physics because of its connection with theories that go beyond the Standard Model such as Supersymmetry and extra dimensional models. Although its nature remains undisclosed, among a wide range of candidates, there is a growing indication that the galactic halo could be permeated by hypothetical particles called WIMPs, with mass of the order of 100 GeV. WIMPs stands for Weakly Interacting Massive Particles, and includes candidates from different models but all sharing some common features: they are cold, interact only by weak and gravitational forces and are massive compared to standard particles.

Even though WIMPs are extremely difficult to detect, there are many experiments underway to this attempt. The experimental effort for the search of DM goes in different directions: from direct and indirect detection to the searches for new physics with accelerators. Direct detection experiments aim to identify the recoil energy released by WIMPs during the interaction with target nuclei; indirect experiments survey the sky looking for signs of annihilation or decay of DM particles, whereas accelerators concentrate their attention on the production of light colorless supersymmetric particles in colliders.

Direct observation of WIMP-nucleus collisions plays a key role in DM searches, but it also poses significant challenges, as the expected signals are low in energy and very rare. DarkSide is a project for WIMP observation in a dual-phase liquid argon time-projection chamber (LAr-TPC) specifically designed to overcome the difficulties of these challenges. LAr-TPCs can reach high sensitivities thanks to the detection of

both scintillation light and ionization generated by recoiling nuclei, which allows 3D position reconstruction and an effective background rejection. DarkSide-50 is the youngest member of the direct detection DM experiment family. It is the second of a three-phase program started with the prototype DarkSide-10 and will end with the multi-tonne detector DarkSide-G2.
DarkSide-50 is located deep underground at the Gran Sasso National Laboratory of the I.N.F.N., in Italy. With its 3500 m water equivalent of rock, the Gran Sasso protects the detector from cosmic rays. A limiting background for DarkSide-50, as much as for all DM detectors, is the production in its active volumes of nuclear recoils from the elastic scattering of radiogenic and cosmogenic neutrons. To rule out this background, DarkSide-50 is surrounded by a boron-doped liquid scintillator acting as an active, high-efficiency neutron detector, and a water tank serving as a Cherenkov detector for muons, but also as a passive shielding for neutrons and gammas. Despite this multi-detector background rejection system, in order to reach a low, or better null, background level in the WIMP parameters region, there is still a lot of offline analysis to be done.

The main purpose of this thesis is to introduce the general problem of the existence of DM and present the DarkSide experiment as the instrument that could give a possible solution to it. The first chapter has the purpose of illustrating the motivations that led to the search of DM and its possible candidates. Then, in the second chapter, the expected WIMP energy spectrum and signal is given, together with an overview of the most important direct detection techniques. A brief preface for the DarkSide-50 experiment follows in the third chapter, while the fourth is dedicated to the analysis of DarkSide early data and its interpretation in the direct detection DM scenario through the exclusion plot. Here, the problem of background rejection is discussed in depth and, in particular, an original study on radioactive background is carried out, first analyzing alpha particle signals in the detector, then, using the delayed coincidence method, ^{222}Rn activity. Finally, a feasibility study on the ^{39}Ar spike is presented, using the same early data to simulate an alternative running mode for the detector. The ^{39}Ar spike consists in adding ^{39}Ar to the LAr actually present into the TPC in order to increase the event rate. The intent is proving the background rejection performance for very high statistics and attempting to obtain some predictions for the second generation DarkSide experiment.

Chapter 1

Dark Matter

1.1 Evidence for Dark Matter

The history of Dark Matter (DM) begins in 1930 when the first data implying non luminous matter was collected. The dutch astronomer J. Oort, while studying the Doppler shift in stars spectra within the galactic disk, concluded that the mass of visible stars alone could not explain the amount of gravitating matter implied by the measured velocities [1].
Soon after, in 1933, the Swiss astronomer F. Zwicky came to the same conclusion noticing some incoherence in the mass estimate of the Coma galaxy clusters [2]. These observations achieved with galaxy rotation curves were confirmed later on by other studies on gravitational lensing and Cosmic Microwave Background (CMB).
In any case, it was not the first time that unobserved matter was predicted by observing the effects of this mass on the visible neighbors: for example in 1846 U. Le Verrier anticipated the existence of a new celestial object with which to explain the deviation of Uranus orbit from the one calculated accounting only for visible mass. Following Le Verrier's directions, G. Galle discovered the planet Neptune [3].
From 1930 up to now, a lot of effort has been put into the DM field, and some upper limits and estimation have been evaluated, but our knowledge of DM still has not changed very much since the first observations. What we do know now is that there is a huge part of the Universe that we cannot see nor study until the DM mystery is solved. As a matter of fact the most precise measurement of the CMB, combined with the results from large scale structure observations, indicates

that baryonic matter, that makes up stars and galaxies, only contributes to 4.9% of the mass/energy density of the Universe. On the other hand, DM represents 26.8% and dark energy, a mysterious force thought to be responsible for accelerating the expansion of the Universe, accounts for 68.3% [4]. This is a more than valid reason to further investigate one of the most important, open and challenging problems in modern cosmology and particle physics.

1.1.1 Galaxy Rotation Curves

The earliest, and perhaps still most convincing evidence for DM on galactic scales come from the observation of galaxy rotation curves. These curves are basically graphs of stars and gas circular velocities as a function of their distance from the galactic center and usually they are obtained by observing the 21 cm wavelength line of hydrogen[1].
It is supposed that circular velocities follow Newtonian dynamics, thus we can write them as a function of the radius of the individual stars with respect to the galaxy center. For an object in a Keplerian stable orbit, the rotational velocity can be written as

$$v(r) \propto \sqrt{\frac{M(r)}{r}} \tag{1.1.1}$$

where M(r) is the mass included in a radius r. Instead, extensive studies have been performed on spiral galaxies proving that the velocity of stars outside an optical disk of radius R does not drop as $R^{-1/2}$, according to Newtonian physics, but it is approximately constant up to a radius of 12 kpc, so that the estimated mass density needs to vary as R^{-2} outside the matter distribution. In order to explain this behavior, the halo mass density has to vary as $M(r) \propto r$, as shown in figure 1.1.1.

Although there is agreement on the shape of DM halos at large distances (out towards, and even far beyond, the edge of visible disks), there is not a general consensus on the innermost regions of galaxies profiles. Recent studies indicate the presence of shallow, or even flat cores, while numerical simulations of halos suggest

[1] At 1420 MHz, this radiation from hydrogen penetrates the dust clouds and gives a more complete map of the hydrogen than that of the stars themselves since their visible light won't penetrate the dust clouds

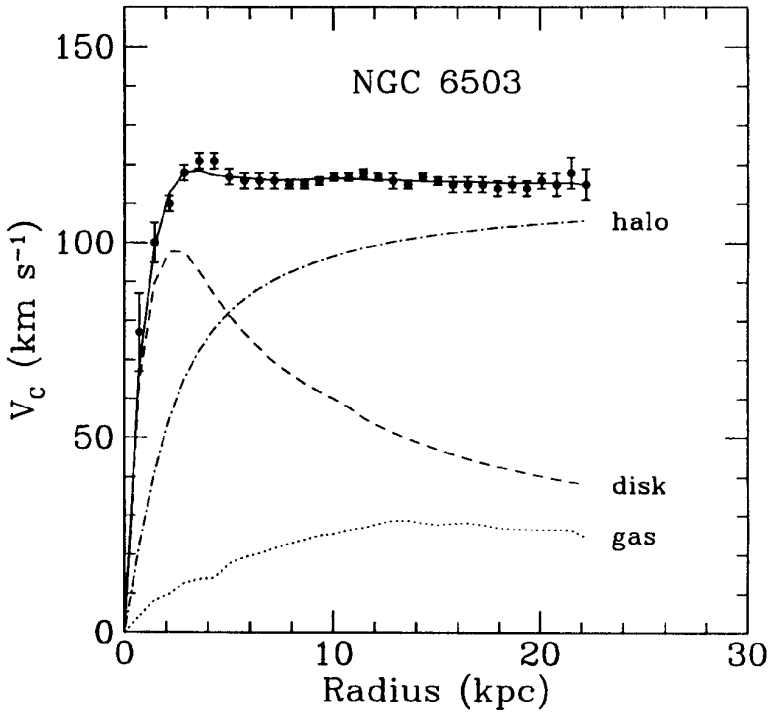

Figure 1.1.1: *Galactic rotation curve for NGC 6503 showing disk and gas contribution plus the dark matter halo contribution needed to match the data.*

steeper, or even cuspy, density profiles.

In spite of the uncertainties on velocity profiles in the innermost regions, rotation curves of disk galaxies provide strong evidence of a spherical DM halo. Studies on the stars of Galaxy M31, performed by H. W. Babcock in 1939 [5], exhibit for example such a high rotational velocity around the galaxy center that it would allow stars to escape the gravitational field if DM did not exist.

The first hint of DM on a bigger scale comes from the measurements of velocity dispersion of galaxy clusters. Indeed, the mass of Coma galaxy cluster implied by luminosity did not match the mass predicted using Clausius virial theorem for which kinetic and potential energy of a system moving in a limited space are strictly related. The discrepancy was of about one order of magnitude and this led to the conclusion that some non luminous matter, responsible for most of the mass distribution must exist.

1.1.2 Standard Cosmological Model

Before proceeding further with the description of gravitational lensing and CMB effects, a brief introduction to standard cosmology is needed. Most cosmologists, indeed, agree on the Big Bang scenario which describes the Universe as a system evolving from a highly compressed state that existed around 10^{10} years ago. To create a cosmological model that satisfies the properties of the Universe as we observe it now, it is necessary to have an equation that relates the geometry of the Universe with its matter and energy content, a metric describing the symmetries of space-time and finally an equation of state to specify the physical features of the matter and energy content. The first of these requirements is satisfied by Einstein's field equation. To solve Einstein's equations one has to specify the symmetries of the problem. Assuming the properties of isotropy and homogeneity (confirmed by observation of the CMB) the most general metric describing space-time is that of Robertson-Walker [6], which in polar coordinates is

$$ds^2 = dt^2 - a(t)^2 \left[\frac{dr^2}{1 - Kr^2} + r^2(d\vartheta^2 + sin^2\vartheta \; d\varphi^2) \right] \tag{1.1.2}$$

where $a(t)$ is the factor of expansion, (r, ϑ, φ) are the adimensional comovement coordinates and $K = (-1, 0, +1)$ is the curvature parameter: -1 for an open Universe, 0 for a flat Universe and $+1$ for a closed one.
Solving the Einstein equation with this metric leads to Friedmann's equations, the first of which describes the rate of expansion

$$\left(\frac{\dot{a}}{a}\right)^2 = \frac{8\pi G_N}{3}\rho - \frac{K}{a^2} \tag{1.1.3}$$

where $H = \dot{a}/a$ is the Hubble parameter. In case of a flat Universe ($K = 0$), from equation 1.1.3, the energy density equals the critical density $\rho_c \equiv 3H^3/8\pi G_N$ that represents the boundary between perpetual expansion or collapse after a period of expansion. In addition, the critical density is often used to express the abundance of a substance $\Omega_i = \rho_i/\rho_c$, where ρ_i represents the abundance of a specific element. The various Ω_i evolve differently with time but a general expression for the expansion

Figure 1.1.2: *Image of Abell 2218 cluster. Real galaxies do not have this shape: they are usually elliptical or spiral shaped they just appear this way because of lensing.*

rate is given by Ref. [9]

$$\frac{H^2(z)}{H_0^2} = \left[\Omega_X(1+z)^{3(1+\alpha X)} + \Omega_K(1+z)^2 + \Omega_M(1+z)^3 + \Omega_R(1+z)^4\right] \quad (1.1.4)$$

where z is the redshift, M and R are respectively labels for matter and radiation, $\Omega_K = -K/a_0^2H_0^2$ and X refers to a generic substance of state equation $p_X = \alpha_X\rho_X$.

1.1.3 Gravitational Lensing

Galaxy rotation curves are not the only tool with which to estimate matter. The mass of clusters and galaxies can also be determined via gravitational lensing, which effects can be observed in figure 1.1.3 and the measurement of which gave results in favor of DM.

Gravitational lensing consists of measuring changes in the light path or equivalently, from Einstein's general theory of relativity, in the space-time structure produced by the presence of matter. Massive objects can, in fact, modify the space-time around them to the point that an observer can see curved or multiple images of the object's

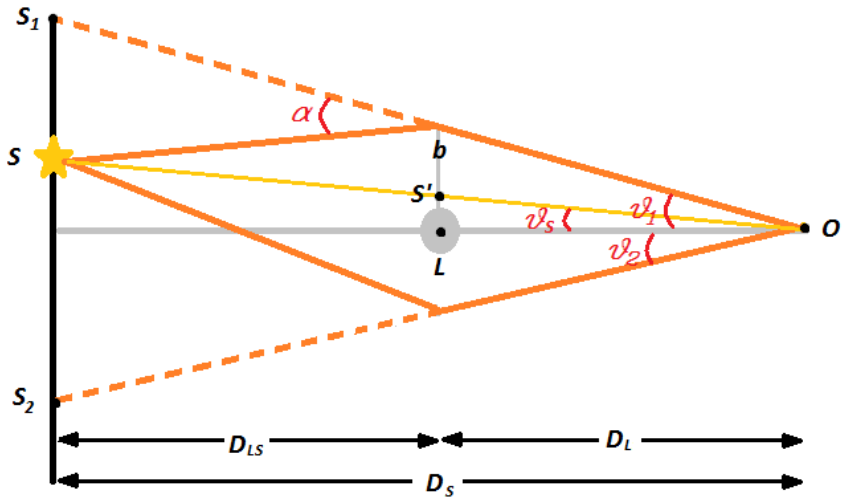

Figure 1.1.3: *The two images S1 and S2 of a source S formed from gravitational lensing by a point mass L.*

background.
The gravitational deflection α of photons passing by a point mass M at a distance b is

$$\alpha = \frac{4G_N M}{c^2 b} \tag{1.1.5}$$

The gravitational deflection of light implies that massive objects may act as gravitational lenses. As a consequence of this effect the light source S in figure 1.1.3, whose rays pass close to a massive point L, is seen by the observer O shifted from its original position. In this schematic representation of gravitational lensing θ_S, θ_1 and θ_2 are respectively the angles between the observer-object axis and the real source S and the apparent sources S_1 and S_2. From equation 1.1.5

$$\alpha D_{LS} = D_S(\vartheta_1 - \vartheta_S) \tag{1.1.6}$$

$$\vartheta_S = \vartheta_1 - \frac{4G_N M}{c^2 b}\frac{D_{LS}}{D_S} = \vartheta_1 - \frac{4G_N M}{c^2}\frac{D_{LS}}{D_S D_L \vartheta_1} \tag{1.1.7}$$

where D_L, D_{LS} and D_S are respectively the distances observer-object, object-source

and observer-source. In the collinear case in which $\vartheta_S \to 0$

$$\vartheta_1 \equiv \vartheta_E = \left(\frac{4G_N M}{c^2} \frac{D_{LS}}{D_S D_L} \right)^{1/2} \tag{1.1.8}$$

where ϑ_E is the angle of the so called Einstein ring meaning that the observer sees S as a ring of light centered on the line of sight. This simplified method can be applied to objects extended in space, in which case the result is much more complex.
In any case, gravitational lensing is a valid method with which to calculate the mass of astrophysical objects. The discrepancy in mass estimated in this way and the one that accounts for luminous matter only leads again to the conclusion that non luminous matter may exist in galaxy clusters.

1.1.4 Cosmic Microwave Background

On the scales of galaxies and clusters it is difficult to estimate the total amount of DM that pervades the Universe. However, on the cosmological scale, this is feasible by means of the information extracted from the Cosmic Microwave Background (CMB) (see figure 1.1.4).

In 1965 A. Penzias and R. Wilson [7] discovered that the Earth is immersed in mi-

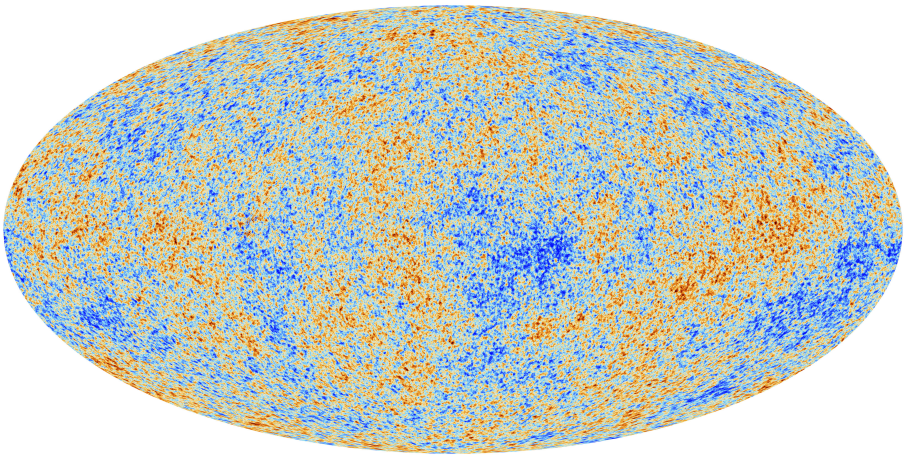

Figure 1.1.4: *Detailed map of CMB temperature fluctuations (relic radiation from the Big Bang) from ESA and Planck Collaboration.*

crowave radiation. The CMB has been found to be highly isotropic, with a precision of 10^{-5}, and follows the spectrum of a blackbody corresponding to a temperature of $T = 2.726$ K. The analysis of CMB anisotropies allows for testing cosmological models and setting stringent constraints on them, given that they are connected to the formation of the first structures of the Universe.
Given a cosmological model with a fixed number of parameters, the best fit of the parameters is determined from the peaks of the N-dimensional likelyhood surface. From this simple method, at least in principle, one can extract values such as baryonic and matter density. Recent results [4] give

$$\Omega_b h^2 = 0.02214 \pm 0.00024 \qquad \Omega_{nb} h^2 = 0.1187 \pm 0.0017 \tag{1.1.9}$$

where h is the rescaled Hubble parameter of which the most recent value is $h = 0.678 \pm 0.012$ [8]. The value of $\Omega_b h^2$ is consistent with the predictions from Big Bang nucleosynthesis, but is one order of magnitude smaller than the total matter density.

1.2 Candidates for Dark Matter

Even when all baryonic forms such as dust, brown and white dwarfs, neutron stars and black holes are taken into account, it still appears that a considerable fraction of non-baryonic matter is needed to justify all the observations listed in the previous sections. This remains true even after taking into account the so-called MACHOs (Massive Compact Halo Objects), objects that can only be seen by gravitational lensing. For this reason, since the time in which the existence of DM was speculated for the first time, there has been a proliferation of different theories and DM candidates.
Paragraph 1.2.1 will briefly illustrate two theories not based on the existence of DM. Then, subsection 1.2.2 will present an overview of the Standard Model (SM) for Particle Physics, which is the limit at which all other models have to converge.
The most popular DM candidates are Weakly Interacting Massive Particles (WIMPs), predicted by theoretical extension of the SM such as LSP in Supersymmetry and Kaluza-Klein (K-K) resonance particles in the Universal Extra Dimension theory.

WIMPs-like particles coming from these different models have, however, some common features: they have masses in the range GeV to TeV and they interact weakly with matter.
Before proceeding with the description of some of the possible DM particles, it is fundamental to give some guidelines that all the good candidates have to follow: in fact, the existence of cold dark matter (CDM) has been demonstrated by simulations of the large-scale structure of the Universe with the only requirements being that they are cold and weakly interacting. Accordingly, DM candidates must have these basic requirements:

- matching the appropriate relic density;
- being cold and neutral;
- being consistent with Big Bang nucleosynthesis;
- leaving stellar evolution unchanged;
- being compatible with self interaction, γ-ray constraints and other astrophysical bounds;
- being possible to prove experimentally;

1.2.1 MOND and Gravitational Theories

There are models which manage to fulfill most of the issues that brought up the picture of a Universe full of DM, without the need to postulate it.
One of these is the MOND theory [10] (Modified Newtonian Dynamics) from M. Milgram, which assumes that the law of gravity is different from the Newtonian form

$$a_G = GM/r^2 + \sqrt{GMa_0}/r \tag{1.2.1}$$

According to this theory the force of attraction would be greater then what we would normally think and therefore it would have to be compensated by a faster rotational velocity of astrophysical objects.
Another theory that treads the same path is the one supposing the existence of a time-dependent gravitational constant $G(t)$. This constant would have a large effect on the genesis of galaxies.

Up to now none of these theories have been proved.

1.2.2 Standard Model of Particle Physics

In the past the SM of Particle Physics accounted for all observed particles and was able to predict new particle that then were discovered, such as the bosons $W^{\pm}$, Z_0 and H_0. Despite its success it is clear now that this model is only the limit at low energy of a more fundamental theory.
In the SM, the fundamental constituents of matter are fermions: quarks and leptons. The interaction among fermions are mediated by gauge bosons. In particular, for strong interaction the mediators are gluons, for electroweaks interactions are $W^{\pm}$, Z_0 and γ. The interaction of the Higgs bosons H_0 give mass to all other particles. In general leptons and quarks are arranged into three generations of SU(2) doublets

$$\begin{pmatrix} \nu_e \\ e^- \end{pmatrix} \quad \begin{pmatrix} \nu_\mu \\ \mu^- \end{pmatrix} \quad \begin{pmatrix} \nu_\tau \\ \tau^- \end{pmatrix} \tag{1.2.2}$$

$$\begin{pmatrix} u \\ d' \end{pmatrix} \quad \begin{pmatrix} c \\ s' \end{pmatrix} \quad \begin{pmatrix} t \\ b' \end{pmatrix} \tag{1.2.3}$$

Each particle has a corresponding antiparticle with the same mass and opposite quantum numbers. The quarks that are primed are weak eigenstates related to mass eigenstates by the Cabibbo-Kobayashi-Maskawa (CKM) matrix.

$$\begin{pmatrix} d' \\ s' \\ b' \end{pmatrix} = \begin{pmatrix} V_{ud} & V_{us} & V_{ub} \\ V_{cd} & V_{cs} & V_{cb} \\ V_{td} & V_{ts} & V_{tb} \end{pmatrix} \begin{pmatrix} d \\ s \\ b \end{pmatrix} \tag{1.2.4}$$

For more information about this topic see reference [11].
In any case, DM and dark energy do not find an explanation within the SM of particle physics, meaning that not only in astrophysics, but also in particle physics there is a need for some kind of new physics beyond the SM. In fact, the SM has weakpoints on both experimental and theoretical sides, like the oscillation mechanism of neutrinos that led to discover that they do have mass, the hierarchy problem and the issue of unification of all forces.

The only SM particles that have ever been considered possible candidates for DM are neutrinos. They are indeed weakly interacting, stable fundamental particles and moreover they do not carry any electric charge, so they do not emit nor absorb light. Neutrinos are predicted to be massless by the standard model, but there is strong evidence that they have a finite mass. However, even though neutrinos appear to be a plausible candidate for DM, they have soon been ruled out because of the upper limit of their relic density. From the analysis of CMB anisotropies combined with large scale structure data this upper limit on neutrinos relic density is, at 95% confidence limit,

$$\Omega_\nu h^2 \leq 0.0067 \tag{1.2.5}$$

which means that neutrinos are not abundant enough to be a possible dominant component of DM. Moreover neutrinos are relativistic and therefore they cannot belong to CDM.
As a result, the DM particle hypothesis necessarily implies an extension of the SM.

1.2.3 Sterile Neutrinos

Next in the list of candidates, present in most extensions of the SM, is the sterile neutrino [12]. The hypothesis of a new kind of neutrino comes from the necessity to explain the anomalies observed in neutrino experiments, in the context of the standard 3 neutrino framework. However the results from LEP on the Z boson show that there are only three neutrinos which couple to the Z boson, and therefore the fourth neutrino, if it indeed exists, does not interact weakly and this is why is called sterile neutrino.
Sterile neutrinos can be introduced by a minimal extension of the SM adding three right-handed neutrinos, which are singlets under the SM gauge group. Sterile neutrinos in principle can have any mass because its generation has different possibilities: a Dirac mass term generated by a Higgs doublet, a Majorana mass term generated by a Higgs triplet or a Majorana mass term generated by higher-dimensional operator. In any case, for DM neutrinos, the mass scale is bounded from several considerations about stability and lifetime of the Universe, which favor relatively light (keV scale) neutrinos. In order to provide more quantitative information, assuming that the Dirac mass M_D is tiny compared with the Majorana mass M, i.e. $M_D \ll M$, the

active and sterile mass eigenstates can be written in function of the mixing angle $\theta = M_D/M$:

$$|\nu_a\rangle = \cos\theta|\nu_L\rangle + \sin\theta|\nu_R\rangle \tag{1.2.6}$$

$$|\nu_s\rangle = -\sin\theta|\nu_L\rangle + \cos\theta|\nu_R\rangle \tag{1.2.7}$$

If the sterile neutrino decays mostly into two neutrinos and one anti-neutrino through the exchange of a Z^0 boson, the decay rate and lifetime are respectively

$$\Lambda = \frac{G_F^2 M_S^5}{96\pi^3}\theta^2 \quad \Rightarrow \quad \tau_S = \frac{\hbar}{\Lambda} \sim 10^{20} sec \left(\frac{M_S}{keV}\right)^5 \theta^{-2} \tag{1.2.8}$$

If sterile neutrino constitutes DM then his lifetime has to be $\gg 10^{17} sec$. This is possible only if its mass is of the order of keV. More stringent constraints are imposed on the combination of the masses and mixing angles of the sterile neutrino DM by the non-observation of a DM decay line in X-ray spectra of DM-dominated objects, which give a lower limit on the mass of about 0.3 keV.

1.2.4 Supersymmetry (SUSY)

In the SM of particle physics there is a clear distinction between bosons and fermions. In fact, as mentioned in subsection 1.2.2, bosons are mediators of interactions while fermions are the constituents of matter. It is natural to imagine some sort of "unified" representation of matter and interaction in which symmetry between these two components exists. A theory having this symmetry is called supersymmetry (SUSY).
Beyond the love for matter-interaction symmetry, the fermions-boson symmetry is also a solution to the hierarchical problem of the SM, related to the huge difference between the electroweak and the Plank energy scales. This problem arises in the Higgs boson self energy calculation that, unless the coupling constant is finely tuned, usually leads to divergent results [13]. In particular, while the radiative corrections make fermion masses increase logarithmically, scalar masses increase quadratically

with energy, giving correction at one loop of

$$\delta m_s^2 \sim \left(\frac{\alpha}{e\pi}\right) \Lambda^2 \tag{1.2.9}$$

where Λ is a high-energy cut-off. The radiative corrections to the Higgs mass (which has been measured to be 126.0±0.4 (stat)±0.4 (sys) GeV/c^2 [15]) will destroy the stability of the electroweak scale if Λ is near the Planck mass. However, if one considers that every fermion has a boson partner and vice versa, the radiative corrections of supersymmetric partners would mostly cancel themselves out and the divergence would be removed. In conclusion, the SUSY theory postulates the presence of new particles with a spin different by one half with respect to their SM partners, in such a way that the contribution of fermion loops have opposite sign to the analogous bosonic loops. Equation 1.2.9 becomes

$$\delta m_s^2 \sim \left(\frac{\alpha}{e\pi}\right) \left(\Lambda^2 + m_B^2\right) - \left(\frac{\alpha}{e\pi}\right) \left(\Lambda^2 + m_F^2\right) = \left(\frac{\alpha}{e\pi}\right) \left(m_B^2 - m_F^2\right) \tag{1.2.10}$$

Provided that $|m_B^2 - m_F^2| \leq 1$ TeV, the quadratic divergence to the Higgs mass is cancelled at all orders of the perturbation theory.
Because there is still no evidence and thus no experimental observation of supersymmetric partners of SM particles, they are likely to be very massive and/or they do not interact strongly nor electromagnetically. From these assertions it is obvious that, if SUSY exists, the Universe would be populated by stable, massive and rarely interacting particles, hence good candidates for DM.
The SUSY model that contemplates the smallest number of particles is the Minimal Supersymmetric Standard Model (MSSM). In the MSSM every gauge field has a correlated fermionic superpartner as shown in table 1.2.1

One additional ingredient of the MSSM is the conservation of R-parity which is a multiplicative quantum number defined as

$$R \equiv (-1)^{3B+L+2s} \tag{1.2.11}$$

where B and L are respectively the baryon and lepton numbers and s is the spin. All of the SM particles have R-parity $R = 1$ and all sparticles (i.e. superpartners) have $R = -1$. Thus, as a consequence of R-parity conservation, sparticles can only decay into an odd number of sparticles (plus Standard Model particles). Therefore

SM name	SM particles	Spin	MSSM name	MSSM particle	Spin
gauge fields	g	1	gaugino	$\tilde{g}$	1/2
	W_i	1		$\tilde{W}_i$	1/2
	B	1		$\tilde{B}$	1/2
Higgs	H_1	0	Higgsino	$\tilde{H}_1$	1/2
	H_2	0		$\tilde{H}_2$	1/2
leptons and neutrinos	$\begin{pmatrix}\nu_L\\ e_L\end{pmatrix}$	1/2	sleptons and sneutrinos	$\begin{pmatrix}\tilde{\nu_L}\\ \tilde{e_L}\end{pmatrix}$	0
	$\bar{e_R}$	1/2		$\tilde{e}^*_R$	0
quarks	$\begin{pmatrix}u_L\\ d_L\end{pmatrix}$	1/2	squarks	$\begin{pmatrix}\tilde{u_L}\\ \tilde{d_L}\end{pmatrix}$	0
	$\bar{u_R}$	1/2		$\tilde{u}^*_R$	0
	$\bar{d_R}$	1/2		$\tilde{d}^*_R$	0

Table 1.2.1: *Particle content of the MSSM.*

the lightest sparticles (called LSPs, for Lightest Supesymmetric Particles) are stable and can only be destroyed via pair annihilation, making them an excellent DM candidate.

Among the possible LSPs, the lightest neutralino is so far the best DM candidate. Neutralinos represent the superpartners of neutral bosons B, W_3 (or equivalently Z and γ) and H^0, called binos ($\tilde{B}$), winos ($\tilde{W}_3$) and higgsinos ($\tilde{H}^0_1$ and $\tilde{H}^0_2$) respectively. These superpartners mix into four Majorana fermionic mass eigenstates $\tilde{\chi}^0_1$, $\tilde{\chi}^0_2$, $\tilde{\chi}^0_3$ and $\tilde{\chi}^0_4$, of which the first is the lightest neutralino, simply called χ.

Despite the smallest possible number of particles of the MSSM, this model still has an extremely large number of free parameters, most of which represent masses and mixing angles. In order to predict and study the properties of DM candidate particles, it is crucial to reduce the number of free parameters. This effort is accomplished by making theoretically well motivated assumptions, depending on which one can determine different supersymmetric models including the so called constrained MSSM or mSUGRA and the phenomenologically simplified MSSM. For example, mSUGRA [16] or minimal SUper GRAvity model assumes that breaking occurs through a coupling to gravity and since gravity is flavour-blind, this justifies the assumption that the breaking mass matrices are proportional to the unit matrix. To obtain the mSUGRA scenario, unification at high energy scales is also assumed so that the number of free parameters is cut down also postulating obedience to a

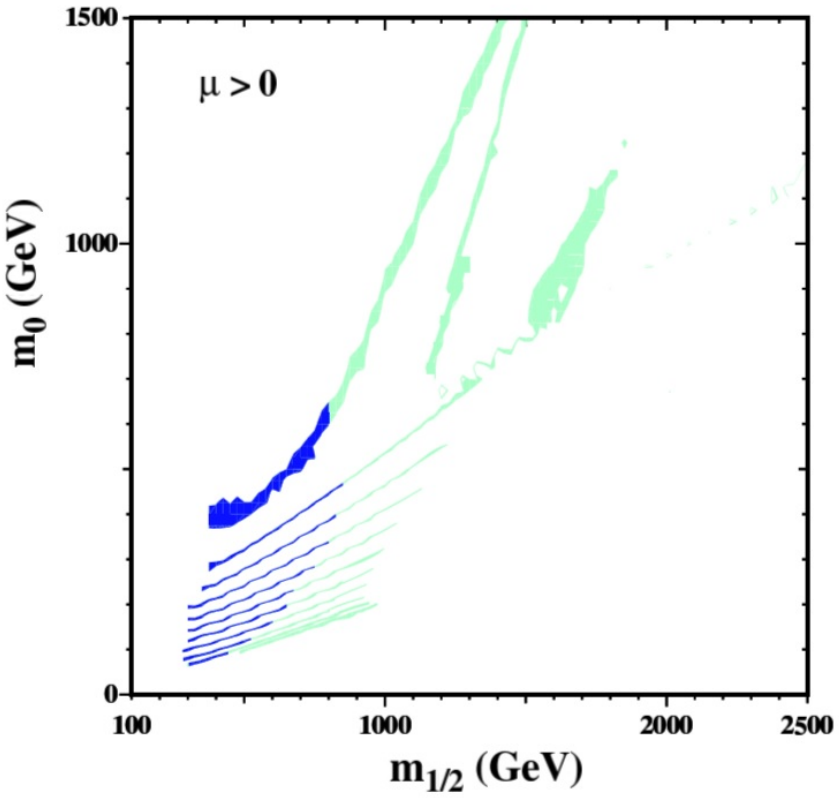

Figure 1.2.1: *Regions of the ($m_{1/2}$, m_0) plane in mSUGRA that are compatible with* $0.094 < \Omega_\chi h^2 < 0.129$ *and laboratory constrains for* $\mu > 0$ *and* $tan\beta$ *=5,10,15,20,25,30,35,40,45,50,55. The darker shade strips are the parts compatible with* $(g-2)_\mu$ *at the 2-*σ *level.*

set of boundary conditions at the Grand Unification scale, thus leaving only five free parameters:

$$\tan\beta,\ m_{1/2},\ m_0,\ A_0,\ \mathrm{sign}(\mu)$$

where $\tan\beta$ is the ratio of the vacuum expectation values of the two Higgs fields, $m_{1/2}$ is the common mass of gauginos and higgsinos, m_0 is the common mass of scalars such as squarks and sleptons, A_0 is a trilinear coupling and $\mathrm{sign}(\mu)$ stands for the conservation of higgsino mass parameter.

Lastly, combining the mSUGRA model to the constraints obtained by using CMB and accelerator data it is possible, as shown in figure 1.2.4, to locate some restricted

regions in the ($m_{1/2}$, m_0) plane.

1.2.5 Extra Dimensional Models

Despite the fact that in our world we experience 3+1 dimensions, called space-time, at higher energy scales it is unreasonable to exclude the existence of extra dimensions. This prospect gained even more importance after 1921, when T. Kaluza introduced the idea of unifying electromagnetism with gravity by identifying the extra components of the metric tensor with the usual gauge fields. The presence of extra dimensions could probably solve the hierarchy problem by taking advantage of the geometry of space-time.
In this new perspective, the 4-dimensional everyday space-time assumes the role of a structure called *brane*, enclosed in a (3+δ+1) space-time dimensions that is named *bulk*. Depending on the model, the extra dimensions can be compactified on circles of some size R, or have very large curvature or even be flat. In any case, in all extra-dimensional theories, all the fields propagating in the bulk have their momentum quantized in units of $p^2 \sim 1/R^2$, so that for every field in the bulk a set of Fourier expanded modes emerge, called Kaluza-Klein (KK) states. In the 4-dimensional space-time, these KK states assume the form of a series of states with masses $m_n = n/R$, where n is the mode number.
The first KK excitation of the hypercharge gauge boson, $B^{(1)}$, captures the attention of DM physics because it is associated to a valid DM candidate: the Lightest Kaluza-Klein Particle (LKP). A calculation of $B^{(1)}$ relic density was carried out by G. Servant and T. Tait [17], considering the constraints set by the amount of DM observed. From this estimation the results are that the mass of the LKP, which is inversely proportional to the compactification radius R, is in the range between 400 and 1200 GeV.

1.2.6 Axions

Axions are hypothetical elementary particles introduced in 1977 in order to solve the strong CP problem in quantum chromodynamics (QCD) [22]. Since axions have been predicted as interacting in an extremely weak way with ordinary matter, they

joined the DM candidates zoo.
Thanks to laboratory searches and astrophysical observations it was possible to estimate the axions mass which turned out to be very light: $\sim 10^{-4}$ eV. Smaller masses would lead to an unacceptably large cosmological abundance while larger masses are ruled out by a combination of constraints from supernova 1987A, laboratory experiments and the search for two-photon decays of relic axions. If axion mass is indeed so small, the relic density is $\Omega_a \sim 1$, and therefore the axion may account for the halo DM. Such axions would be produced in the early Universe with zero momentum by a misalignment mechanism and thus, act as cold DM. Moreover, because of the weak interaction with other SM particles, in the early Universe, axions were not in thermal equilibrium.
Even though the calculation for axion relic density is uncertain, this and the mass estimate help in the not so easy task of finding an acceptable range where these particles satisfy all the constraints from laboratory and direct astrophysical studies. Axions then officially become valid DM candidates.

1.2.7 Superheavy DM candidates

The possible DM candidates are distributed in a wide range of masses, from sub-eV to TeV. This upper limit results from the maximum annihilation cross section, σ_v, for a particle of mass m_{DM}, assuming that DM is a thermal relic of the early Universe. Applying this boundary to the relic density $\Omega_{DM}h^2$ extracted from the CMB, a constraint on the mass $m_{DM} \leq 34$ TeV is obtained.
Abstaining from making this assumption, it is possible to also include, within the DM candidates, superheavy particles, generically called wimpzillas [18]. This scenario assumes that wimpzillas must not have been in equilibrium during freeze-out and, therefore, their relic abundance does not depend upon their annihilation cross section. Furthermore, in order to reproduce the relic DM density observed in the present, wimpzillas need to be stable and their decay and annihilation rate must be very low. The mass of this superheavy particle is usually bigger than 10^{10} GeV and it can go up to 10^{16} GeV, reaching the grand unified masses. Nevertheless, there are theories that predict particles with even higher masses, which in some particular cases can also be strongly interactive. These particles with masses higher than

wimpzillas, take the name of simpzillas [19].
At last, the existence of superheavy DM candidates (both wimpzillas and simpzillas) solve the problem of the observation of the ultra-high energy cosmic rays above the so called GZK cut-off[2] which occurs at about $5 \cdot 10^{19}$ eV and it is due to the slowing interaction of cosmic ray protons with CMB photons. The cross section of this interaction is quite large, so it makes the universe opaque to protons with energy above this limit and that originate at cosmological distances (since there are no known astrophysical sources that can account for such high energy protons). Hence, the decay and annihilation of superheavy DM candidates could be the answer to this problem that has been unsolved for such a long time.

[2]Greisen-Zatsepin-Kuzmin limit.

Chapter 2

Dark Matter Detection

The first chapter has been devoted to the description of some of the many theories that have been hypothesized in order to explain the anomalies observed in astrophysical objects and to overcomel the inconsistency of the SM of particle physics. These theories lead to possible new particles, but they will remain pure speculation until experiments are able to prove what DM really is.
In this chapter a brief overview of detection methods is presented, with particular focus on direct detection. It follows a short description of the current direct detection DM experiments.

2.1 Detection Techniques: Direct and Indirect

Direct and indirect detection are the two basic methods used in DM search. Even though they are very different one from the other, these two methods are complementary in the sense that the succes of either of them would push the use of the other even further for the sake of providing convincing confirmation of the discovery of DM.
Indirect techniques search for secondary products due to decay or annihilation of DM particles in our Galaxy (the galactic center provides one of the best sources of gamma rays from DM annihilation) or in regions of high concentration of DM as, for example, low-surface brightness galaxies (LSB) or dwarf spheroidal galaxies (DSph). In fact, in regions of very high DM density, DM particles and their antipar-

ticles are expected to annihilate themselves into gamma-rays, either directly into a gamma-ray line (with energy equal to the mass of the particle $E_\gamma = M_W c^2$) or a broad spectrum of gamma-rays.
On the other hand, direct search is based on the detection of DM particles passing through a detector and interacting with it. Specifically direct search aims to reveal the energy deposited by DM particles on target nuclei.

2.2 Expected WIMP Direct Detection Signals

First of all, before going into any detailed calculations, it is necessary to mention that WIMPs are expected to have only weak interactions since they do not absorb nor emit light. Therefore, what direct detection experiments seek to measure is not the light emitted by WIMPs themselves, but the recoil energy deposited when a WIMP interacts with a nucleus in the detector, also called recoil energy E_R. The recoiling nucleus will then transfer this energy to electrons or to other nuclei, causing, in the first case ionization or scintillation[1] and in the second case, the production of heat. This section will be dedicated to explaining what the expected signal produced by a WIMP in a detector is and what kind of forecasts it is possible to extract from it. When projecting a DM direct detection experiment, as in any other particle physics experiment, it is necessary to estimate how many events the detector will see after an exposure time T. The expected number of recoils observed by a detector is given by

$$N_{rec} = M_t T R \tag{2.2.1}$$

where M_t is the total mass of the target material and R is the WIMP-nucleus interaction rate. The first and most important estimate that has to be performed is indeed the rate of collision between WIMPs and nucleus. The WIMP-nucleus interaction rate per kilogram of target mass, integrated over all the possible recoils energies and velocities, is given by

$$R = \frac{N_0}{A} \sigma_W \Phi_W \tag{2.2.2}$$

[1]The observed energy is quoted in electron-equivalent energy (keVee).

where N_0/A is the number of target nuclei per kilogram of material[2], σ_W is the cross section for a WIMP-nucleus collision and Φ_W is the WIMP flux.

In the next two paragraphs, the last two terms of equation 2.2.2, which are essential towards obtaining the recoil energy spectrum, are discussed and later on, within this thesis, the final exclusion plot (shown in section 4.4) will be presented.

2.2.1 WIMP-Nucleus Interaction

The total scattering cross section mentioned above, σ_W, may be written in terms of spin independent (mostly scalar) and a spin dependent (mostly axial vector) contributions and a form factor that arise from the finite size of the nucleus. Thus, the full cross section is given by Ref. [20], [21]

$$\sigma_W = \frac{4\mu^2}{\pi}\left[[Zf_p + (A-Z)f_n]^2 + 8G_F^2\frac{J+1}{J}(a_p\langle S_p\rangle + a_n\langle S_n\rangle)^2\right]|F(q)|^2 \quad (2.2.3)$$

where $\mu = M_W M_A/(M_W + M_A)$ is the WIMP-nucleus reduced mass, $f_{p,n}$ and $a_{p,n}$ are respectively the effective spin independent and spin dependent couplings of the WIMPs to the nucleons, Z is the atomic number, J the spin of the target material and finally $\langle S_{p,n}\rangle$ are the expectation values of the nucleon spin within the nucleus. $\mid F(q) \mid$ is the form factor that will be discussed in detail in section 4.4.
As far as the spin dependent cross section is concerned, one has to take into account the fact that the contributions from spin dependent proton and neutron couplings often cancel each other out, so that this cross section depends on the net spin of the nucleus. In particular, nuclei with an even number of protons and neutrons, such as Argon, have no sensitivity on spin dependent interactions, thus this term of the cross section is usually neglected.
It is important in this field to compare results across different experiments using different targets. In order to do so, rates have to be expressed in terms of the WIMP-nucleon spin independent cross section, σ_n[3]. Moreover, for many models, $f_p \sim f_n$, so that the spin independent WIMP-nucleus cross section scales with the

[2] $N_0 \sim 6 \times 10^{23}$ is the Avogadro's number and A is the atomic mass number.

[3] Typical weak cross section on single nucleon (proton or neutron) is of the order of $10^{-45} cm^2 = 10^{-7} pb$.

target nucleus mass atomic number A and the cross section becomes

$$\sigma_W^{SI} \propto \sigma_n A^2 |F(q)|^2 \frac{\mu^2}{\mu_n^2} \tag{2.2.4}$$

where μ_n is the reduced mass of WIMP-nucleon system.
Equation 2.2.4 depends on the atomic mass of the target nuclei as A^4 because $\mu^2/\mu_n^2 \sim A^2$, hence σ_W^{SI} is larger than σ_n by a factor $> 10^6$ resulting of the order of 10^{-39} cm^2. The strong dependence of the target material upon the cross section directly influences the interaction rate and thus its choice is crucial for any dark matter experiment. For example in figure 2.2.1 three recoil energy spectrums for different target materials are displayed.

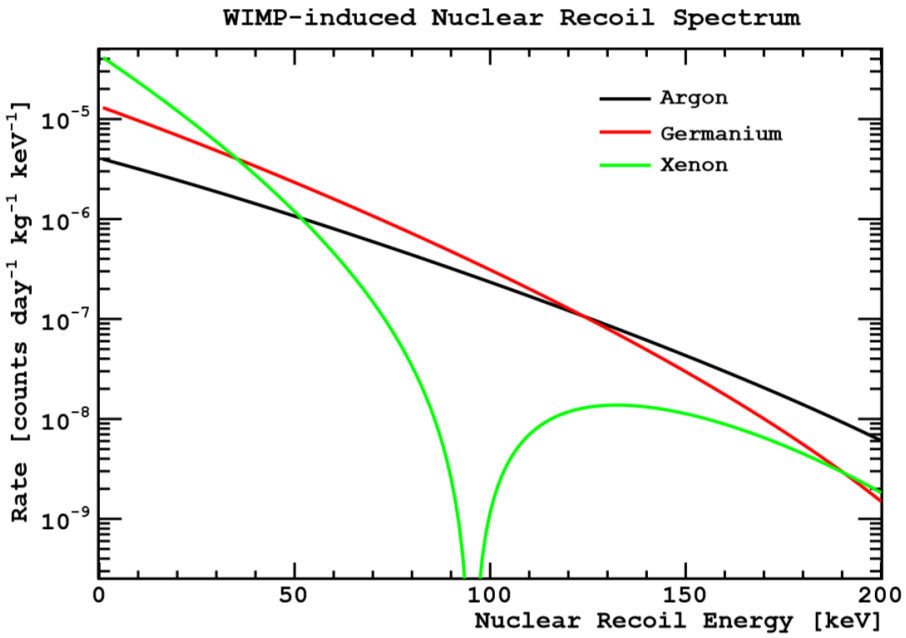

Figure 2.2.1: *Predicted WIMP-induced nuclear recoil rate above threshold, for Xenon, Argon and Germanium targets, for a 100 GeV WIMP with a scattering cross section of 10^{-45} cm^2.*

2.2.2 Dark Matter Distribution and Flux

In general WIMP distribution in galaxies can be estimated by starting from galaxy star rotation curves and implemented by numerical simulations. However the density profile in the region of the galaxy center is still not completely understood, therefore it is impossible to obtain precise simulations but only approximated models. Nevertheless, without forgetting the uncertainties affecting the mass distribution in the halo, the following standard assumptions can be accepted:

- for the local halo density ρ_0 =0.3 GeV cm^{-3}, where ρ_0 is the halo density at the Sun position;
- for WIMP density $\rho_W = \xi\rho_0$, with $\xi < 1$ being the WIMP fraction of the local halo density;
- for WIMP velocity distribution, that it is Maxwellian, characterized by a rms velocity dispersion σ_v and an average velocity of the galactic halo given by $v_0 = \sqrt{3/2}\sigma_v$.

$$f(v) = \begin{cases} k\left(\frac{3}{2\pi\sigma_v^2}\right)^{3/2} e^{\frac{3\vec{v}^2}{2\sigma_v^2}}, & |\vec{v}| \leq v_{esc} \\ 0 & \text{otherwise} \end{cases} \tag{2.2.5}$$

where v is the WIMPs velocity and v_{esc} is the escape velocity above which WIMPs would overcome the gravitational pull and quickly leave the system and k is a normalization factor defined as

$$\frac{1}{k} = \text{erf}(z) - 2ze^{-z^2}/\sqrt{\pi} \tag{2.2.6}$$

where $z = v_{esc}/v_0$. To find the real velocity distribution of WIMPs in the Earth frame, only one ingredient is missing: the Earth's velocity v_E. Actually, considering the fact that the motion of the Earth inside the DM distribution is the combination of the Sun motion in the Galaxy and the orbital terrestrial motion, during the summer the terrestrial orbital velocity adds to the Sun velocity, while during the winter it subtracts from it. This results in a modulation that can be up to 7% considering a non-zero experimental energy threshold. The DAMA experiment [25] seeks to measure this type of modulation instead of the actual WIMP flux.

Adding the contribution of the Earth velocity, the distribution becomes

$$f_D(v) = \frac{vk}{\sqrt{\pi} v_E v_0} \begin{cases} e^{-\frac{(v-v_E)^2}{v_0^2}} - e^{-\frac{(v+v_E)^2}{v_0^2}}, & v \leq v_{esc} - v_E \\ e^{-\frac{(v-v_E)^2}{v_0^2}} - e^{-\frac{v_{esc}^2}{v_0^2}}, & v_{esc} - v_E < v \leq v_{esc} + v_E \\ 0 & v > v_{esc} + v_E \end{cases} \tag{2.2.7}$$

where v is now the DM velocity in the Earth frame. For detailed calculations see reference [21].

Once the velocity distribution has been defined by equation 2.2.7 it is consequential

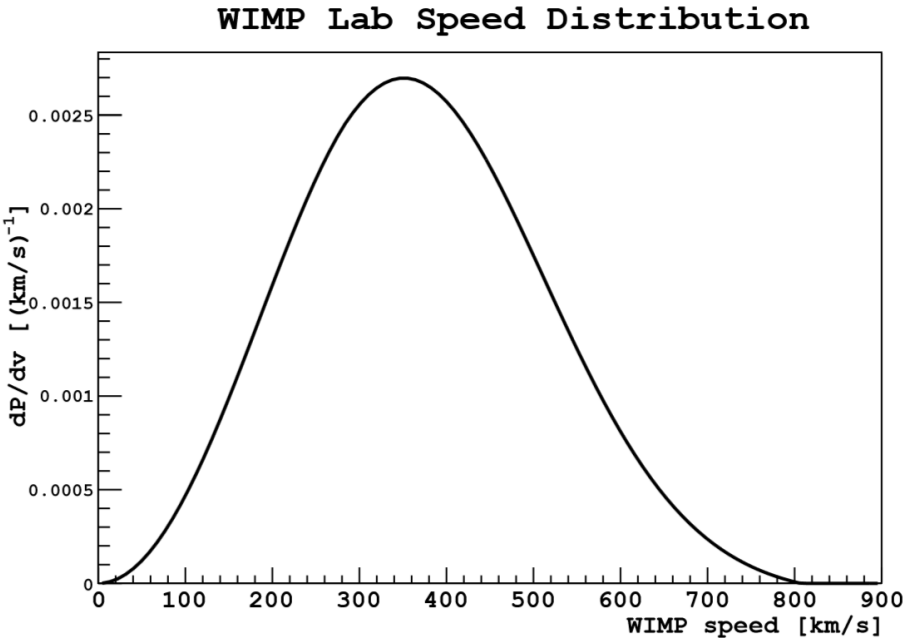

Figure 2.2.2: *Distribution function of DM velocity in the Earth frame.*

to estimate the flux of DM particles integrating the following expression

$$\frac{d\Phi_W}{dv} = \frac{\rho_0}{M_W} v f_D(v) \tag{2.2.8}$$

In order to derive a basic order of magnitude expression for the total WIMPs flux, the mean velocity from figure 2.2.2 which is approximately $\bar{v}$ =360 km/s and a

WIMP mass of about 100 GeV can be used:

$$\Phi_W = \frac{\rho_0}{M_W}\bar{v}. \tag{2.2.9}$$

From equation 2.2.9 a flux of about 10^5 WIMPs cm^{-2} s^{-1} emerges, a huge flux compared to other particles.

2.2.3 Recoils Energy Spectrum

From the knowledge of both the WIMP-nucleus cross section and the velocity distribution, the interaction rate and the recoil spectrum can be finally calculated. The total WIMP rate R_0 is obtained from equations 2.2.2 and 2.2.9

$$R_0 \simeq \frac{N_0}{A}\frac{\rho_0}{M_W}\sigma_W\bar{v} \tag{2.2.10}$$

With a cross section of about 10^{-39} cm^2, the interaction rate R_0 with WIMP flux can be expected to be, at the most, one collision per day per kilogram of target matter but it is also possible that is as low as one interaction per year per ton of detector.
In a detector, if WIMP's initial energy is $E_i = M_W v^2/2$, the recoil energy deposited on nucleus by WIMPs is

$$E_R = E_i r\frac{(1 - cos\theta)}{2} \tag{2.2.11}$$

where r is an adimensional parameter, with the unity as maximum value, related to the WIMP and target nucleus masses:

$$r = \frac{4\mu^2}{M_A M_W} = \frac{4M_A M_W}{(M_A + M_W)^2} \tag{2.2.12}$$

In case of elastic scattering and isotropic center of mass, the differential spectrum of nuclear recoils dR/dE_R can be derived from equation 2.2.2 integrating from a minimum to a maximum WIMP energy or equivalently from a minimum to a maximum WIMP velocity. The minimum velocity for which an interaction can occur is given by $v_{min} = \sqrt{2E_{min}/M_W} = \sqrt{2E_R/(rM_W)}$, while the maximum velocity is the escaping velocity. In the simplest case of a detector in the rest frame of the halo,

with the escaping velocity set to infinite, the differential spectrum is

$$\begin{aligned}\frac{dR}{dE_R}(E_R) &= \int_{E_{min}}^{E_{max}} \frac{dR(E_i)}{E_i r} \\ &= \int_{E_R/r}^{\infty} \frac{1}{(M_W v^2/2)r} \frac{R_0}{2\pi v_0^4} v e^{-v^2/v_0^2} (4\pi v^2 dv) \\ &= \frac{R_0}{(M_W v_0^2/2)r} \int_{v_{min}}^{\infty} \frac{2}{v_0^2} e^{-v^2/v_0^2} v dv = \frac{R_0}{E_0 r} e^{-E_R/E_0 r}\end{aligned} \tag{2.2.13}$$

where $E_0 = M_W v_0^2/2$ is the most probable WIMP incident energy.
Since the energy spectrum falls exponentially, it is critical to have a very low energy threshold in this kind of experiment. Additionally, from equation 2.2.13 it is possible to calculate the mean recoil energy $\langle E_R \rangle = E_0 r$. By replacing r and E_0, it is easily seen that for WIMP masses $M_W \ll M_A$ the mean recoil energy is proportional to M_W^2, while for WIMP masses $M_W \gg M_A$ the $\langle E_R \rangle$ is constant, meaning that heavy WIMPs all yield about the same energy spectrum.

2.3 Overview of Direct Detection Experiments

During the last few years, direct detection experiments provided rather strong limits on the elastic scattering cross section of some of the main DM candidates, ruling out some big regions of the parameter space.
Independently from the details of single designs there are some common requirements that all the WIMP detectors have to fulfill. The previous paragraph displayed what is the expected interaction rate and recoil energy spectrum for a WIMP detector. Using this information and some common sense one can immediatly identify the following general features needed for a WIMP direct detection experiment to be competitive:

- very low energy threshold for nuclear recoils (NR) (the spectrum is nearly exponential, therefore a small gain in threshold corresponds to a significant gain in sensitivity);
- very low radioactive background which means high radiopurity of the materials and therefore selection and cleaning of the materials in order to ensure a raw background below 1 event day^{-1} kg^{-1} keV^{-1};

- underground site for high sensitivity experiments since cosmic rays produce a huge number of counts at low energies;
- rejection of ordinary γ and β background (electron recoils ER) through a specific observable: if such discrimination can be performed, the only background source left is from fast neutrons that can simulate a WIMP interaction;
- sensitivity to a WIMP - specific observable, necessary for an unquestionable WIMP signature.

The sensitivities reached by each experiment are usually reported in an exclusion plot. Every new experiment aims to test those regions of the plane (σ_n, M_W) populated by points corresponding to WIMPs viable candidates and thus to mark out a new line that rules out all the previous ones. The parameters that affect the shape of the exclusion plot are threshold, background spectrum and target mass in such a way that for every given fixed WIMP and nuclear target mass it is possible to determine the nuclear recoil spectrum using equation 2.2.13; the value of the sensitivity corresponding to that particular energy bin, finally establish the upper limit to the cross section σ_n for that specific WIMP mass. The final exclusion plot (figure 2.3.2) is obtained after iterating this procedure over the entire mass range. Among the direct detection experiments searching for WIMPs there are different subgroups characterized by the detection technique upon which they are based. There are three main techniques used to build DM experiments, that can be used alone or combined together as shown in figure 2.3.1: detectors measuring ionization processes, scintillation processes and heating processes.

2.3.1 Ionization

Some DM search projects detect the ionization produced when a particle scatters off the experiment's target nucleus. The recoiling nucleus then ionizes the detector medium producing electrons. This is the technique used by the firsts direct detection experiments. They consist of ultrapure semiconductors like Germanium, protected with a layer of lead and situated in an underground laboratory. Charge readout devices are then used to avalanche electrons from the ionization.
For example CoGeNT[24], 440 g of ultrapure Germanium, installed at the Soudan

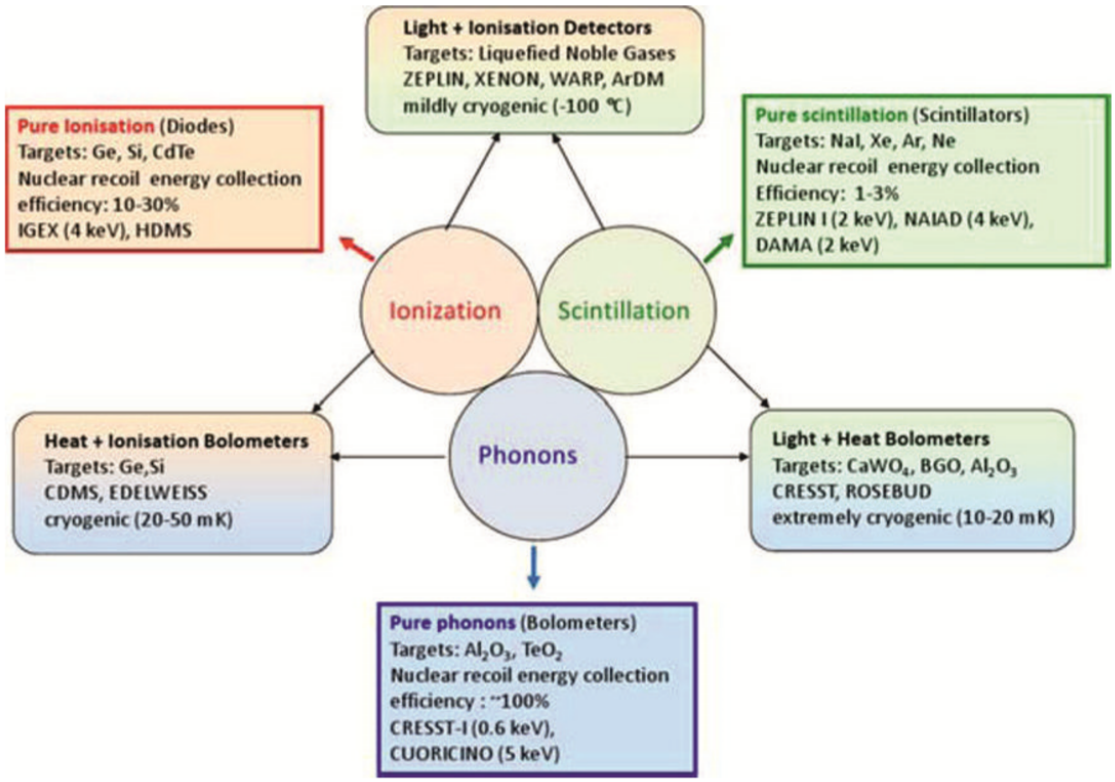

Figure 2.3.1: *The scheme represents the three different read-out methods and the philosophy of double read-out approaches. Representative experiments for each class are indicated.*

Underground labs (PNNL), collected about 3.5 years of data with an effective threshold of 400 eV. The first 56 live days indicated excess events at low energies (<3 keV) and an annual modulation of this excess, that can be a sign of low-mass DM or simply a source of background that has not been understood completely.

2.3.2 Scintillation

Another way to detect WIMPs is by using scintillation processes which are produced by the recoiling nucleus. Scintillating crystals and liquids are used in conjunction with light collectors such as photomultiplier tubes (PMTs) to observe the scintillation light emitted when a particle interacts with a nucleus within the target material, which absorbs energy from the interaction and then releases this energy in the form

of photon emission. Scintillator detectors are able to discriminate between NR and ER background events in the low energy region using pulse shape discrimination (PSD).
An example of this kind of detectors can be the DAMA/LIBRA[25] experiment. Its detector consists of about 250 kg of radiopure NaI (Tl), divided into 25 crystals, for a total exposition of 1.17 tons×year. DAMA observed an annual modulation of WIMP signal in the energy range between 2 and 6 keV at 8.9σ C.L.

2.3.3 Thermal Energy Deposition

Bolometers, or phonon detectors, are used in several dark matter experiments to collect data on thermal energy deposition within different absorbers. This technique detects and measures small temperature changes in the target material caused by energy deposited in the target nuclei from particle interactions, which eventually converts to heat. A bolometer is basically a resistor that is thermally isolated and exposed to the incident radiation (phonons). As the bolometer absorbs the radiation energy, its temperature changes and so the resistance of the device also changes: the amount of energy deposited in the detector can be estimated by measuring the voltage across it. This technique is particularly sensitive in the low WIMP mass region.

2.3.4 Hybrids or Double Read-Out WIMP Detectors

In order to distinguish WIMP-like signals from electron recoils, detectors have to be able to perform a good background rejection. However in single channel devices the discrimination between an event corresponding to an electron recoil and one corresponding to a nuclear recoil is quite difficult. For this reason some dark matter detectors combine two of the techniques described above to improve their resolution and overall sensitivity to WIMP-nucleon interactions. Detectors of this kind have, to date, provided the best limits on WIMP characteristics as shown in figure 2.3.2. In figure 2.3.1 the logic of hybrids devices is represented. Some experiments such as CDMS/CDMS II [26] and ELEDWEISS/EDELWEISS II [27], for example, aim to measure the recoil energy by employing detectors which are highly sensitive to both ionization and phonon signals, reaching in this way energy thresholds of few keV and a good background rejection. These detectors consist of Ge or Si diods operated as

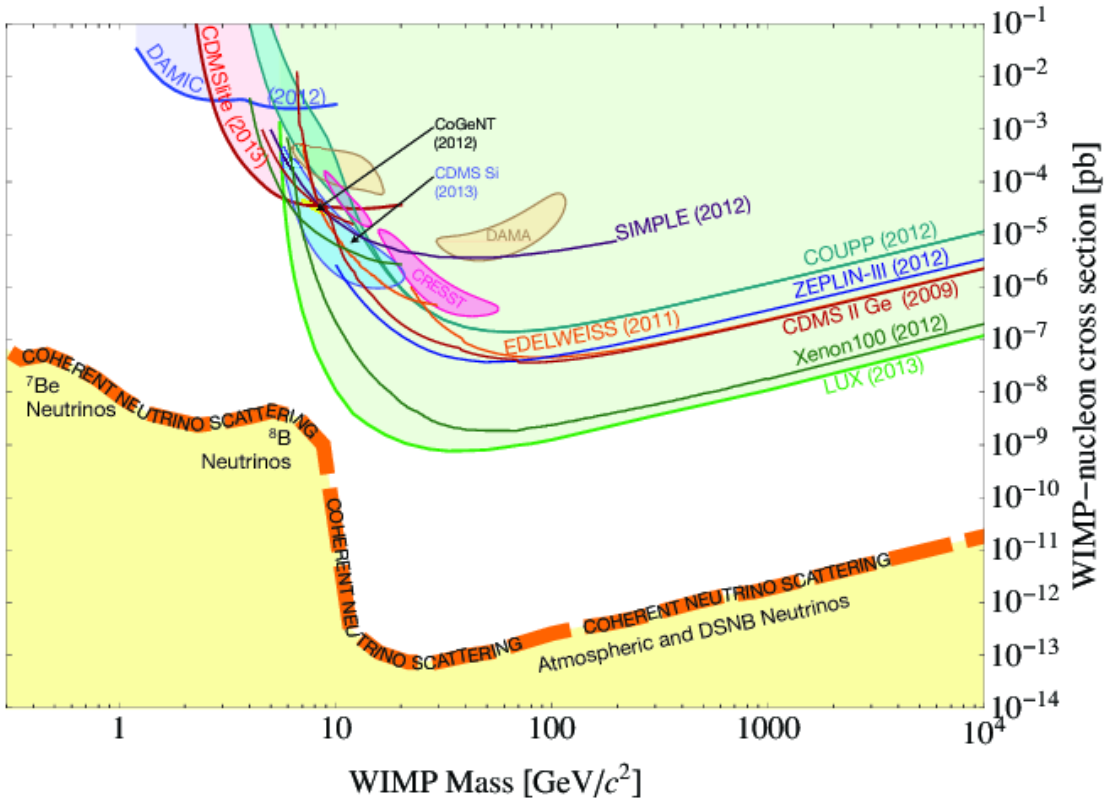

Figure 2.3.2: *Exclusion plot showing the limits reached by means of direct detection dark matter experiments, including the first results from LUX that actually sets the lower limit to DM search. The dashed orange line sets the limit due to atmospheric and solar neutrinos.*

conventional semiconductur devices with the addition of a phonon sensor that can be a properly doped crystal with Ge or a set of superconductive films. Moreover, in order to detect phonons these kinds of detectors need to operate at cryogenic temperatures, usually between 10 and 100 mK. CDMS/CDMS II [28], in particular, is an experiment situated at the Soudan mines and is composed of 19 Ge and 11 Si detectors. CDMS II found three events in the region of interest for WIMPs signals which are above the expected background events and are consistent with WIMPs mass of about 8.6 GeV.

Among the double read out detectors those that employ scintillators to detect the light produced in interactions together with heat sensors are also listed (these de-

Figure 2.3.3: *Calcium tungstate is a scintillator material.When the crystals are excited, here by UV light, they emit light themselves.*

vices are often define "scintillator bolometers"). Again, in order to detect phonons they have to operate at very low temperatures and need to have a sensitivity in light detection within the few-photon range. An experiment that uses this technique is CRESST/CRESST II [29], located at the Gran Sasso National Laboratory (LNGS) and operating at a temperature of about 15 mK. It consists of $CaWO_4$ crystals (figure 2.3.3) in which a particle interaction produces mainly heat in the form of phonons, but also a small amount of scintillation light so that most common backgrounds can be eliminated through their light signal.
The last technique that will be described in this section is the one that benefits from both scintillation and ionization produced by nuclear recoils. Representatives of this kind of experiments are dual phase detectors that make use of noble elements in both liquid and gaseous phases as DM target. These materials are ideal for building large, homogeneous and position-sensitive devices. In such detectors each interaction produces two signals: the first one is due to primary scintillation in the liquid gas produced by a recoil nucleus, while the second one is the secondary

scintillation caused by electrons generated by nuclear recoil ionization processes in the detector bulk and is then drifted, by means of an electric field, in an area where the noble gas is in the gaseous phase. A more detailed description of this process, in the specific case of Argon as a noble gas, can be found in section 4.4.
Experiments using this technique are XENON 100 [30], LUX [31] and DarkSide. LUX in particular is an experiment located at the Sanford Underground Research Facility in South Dakota that uses as its target 368 kg of liquefied ultra-pure Xe. As in the other two experiments listed above, LUX is an ongoing experiment but it has already set the lowest limit on WIMP search claiming a cross section of 7.6×10^{-46} cm^2 at a WIMP mass of 33 GeV/c^2.

Chapter 3

DarkSide-50

The DarkSide project is designed for direct detection of DM particles, using a dual phase Time Projection Chamber (TPC) with Liquid Argon (LAr) targets.
The first prototype of this three-stage program has been DarkSide-10, a 10 kg LAr-TPC inside a passive shield, that provided fundamental measurements such as crucial figure of merit for background rejection, as shown in section 4.2. The current phase is the experiment object of this work of thesis DarkSide-50, the first WIMP-sensitive detector of the DarkSide family, with its 44.1 kg of fiducial mass. This will be the first DM experiment using LAr from an underground gas reservoir, with a content of ^{39}Ar more than 150 times smaller than that of atmospheric Argon (AAr). After it, the next phase will be DarkSide-G2, a LAr-TPC with 3.8 tons of fiducial mass, with the goal of reaching a minimum sensitivity for a WIMP mass of about 100 GeV/c^2, that will allow to see WIMP-nucleon cross sections of about 2×10^{-47} cm^2.
DarkSide-50 is deployed at Laboratori Nazionali del Gran Sasso (LNGS) in Abruzzo, Italy. The experiment is in the hall C of the Underground Laboratories, between the experiments Opera and Borexino as shown in figure 3.0.1. Its underground location gives to DarkSide-50 a great advantage: thanks to 3500 m water equivalent of rock separating the experiment from the external surface, the detector is well shielded from cosmic rays. In the table below (table 3.0.1), a comparison of the background condition on the surface and underground at LNGS [32] is presented.

DarkSide-50 consists in a LAr-TPC, a Neutron Veto and a Muon Veto (figure 3.0.2). The TPC detects both scintillation and ionization channels and provides

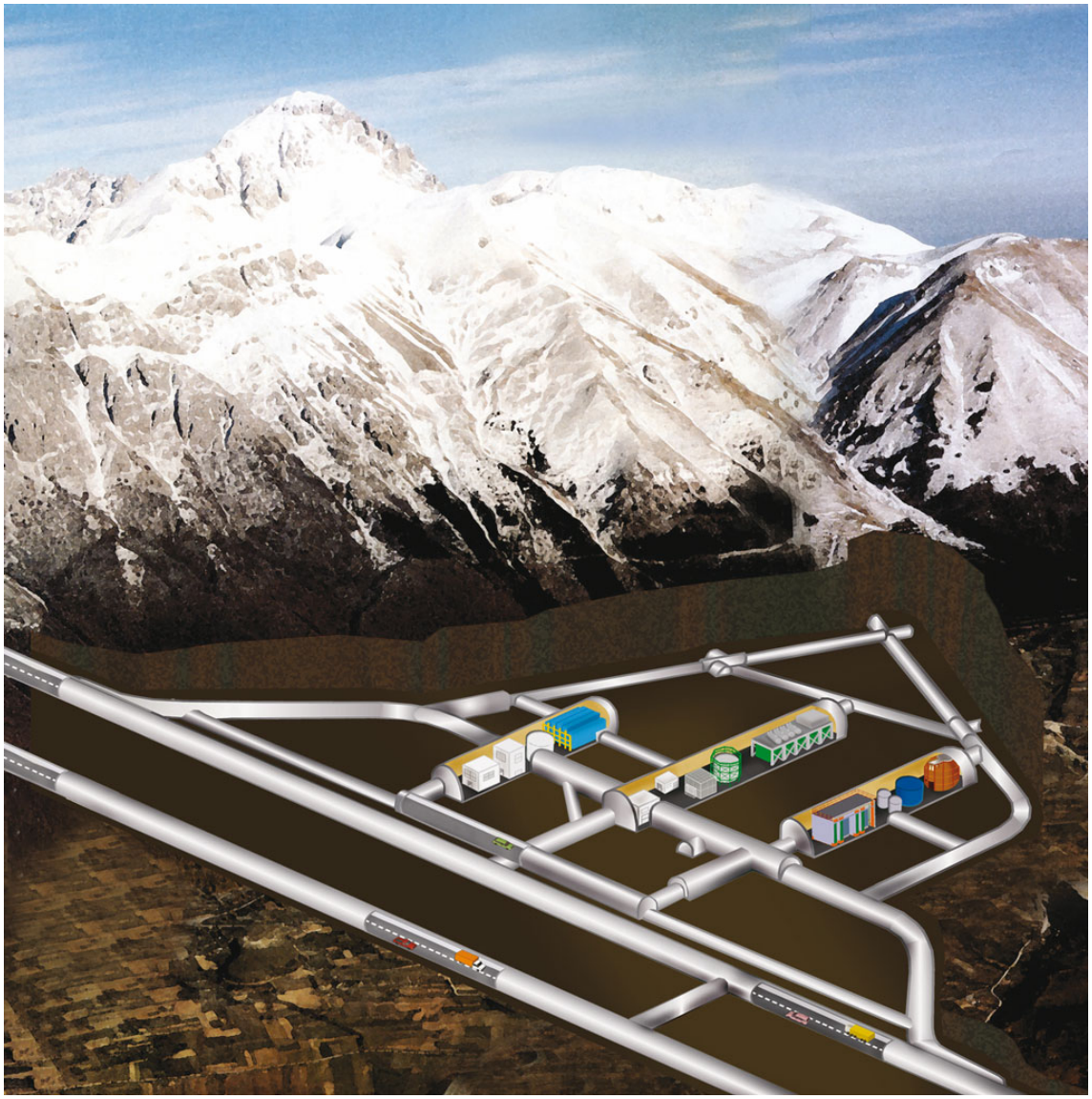

Figure 3.0.1: *Underground Laboratories at LNGS, hosting DarkSide-50 experiment.*

three tools for identifying nuclear recoils among the overwhelming electron recoil background: Pulse Shape Discrimination (PSD), ratio of ionization/scintillation and 3D reconstruction. The cryostat containing the TPC is located in the middle of a liquid scintillator sphere used to actively veto events in the TPC induced by neutron, likely to be captured in the scintillator. The scintillator is a mixture, in equal proportions, of PseudoCumene (PC) and TriMethylBorate (TMB) which favors the

Background source	Flux at surface m^{-2} h^{-1}	Flux at LNGS m^{-2} h^{-1}
μ	$3.1 \cdot 10^6$	1.227 ± 0.004
n termici	$5 \cdot 10^4$	73 ± 2
n epitermici	$4.5 \cdot 10^{-3}$	46 ± 11
$n(E > 0.5$ MeV)	$5.9 \cdot 10^{-8}$	92 ± 10
$n(E > 2.5$ MeV)		3.2 ± 2.1
γ		$\sim 10^7$

Table 3.0.1: *Comparison of cosmic ray backgroung a the surface and underground at LNGS.*

neutron capture. The sphere is then surrounded by a muon Cherenkov detector, a tank filled of ultra-pure water meant to tag neutron induced events associated to muon interactions. Both active vetoes serve also as passive shielding for gamma and neutron background coming from outside the detector. DarkSide is also provided with a recirculation system, that continuously filters the Ar, and of two clean rooms (CRH) of which one is on top of the water tank and the other one right next to it. This facilities are Radon suppressed with an upper limit on the residual Radon activity that reaches 5 mBq/m^3, a factor 20,000 suppression relative to ambient air in the underground laboratories at LNGS. Both CRH had a critical role during the TPC assembly phase because Radon could leave lead daughters on the TPC surface and this could produce surface events that can mimic a nuclear recoil. Moreover, to further remove α contaminants, responsible for (α, n) reactions producing dangerous neutrons, the detector components were carefully cleaned before the assemble. All three detectors were commissioned in October 2013 and have been operating since then, with the TPC filled with Atmospheric Ar (AAr). During this first period of data taking, while the UAr that will constitute the final target material for DM search has been extracted and purified, tests and calibrations have been performed for a more complete knowledge of the detector. In the meantime, a rate higher than expected has been observed in the liquid scintillator. ^{14}C, a radioactive isotope of ^{12}C contained in the TMB, has been identified as the source of this unexpected high rate. In the next few months a new provision of TMB, with a low level of ^{14}C, will substitute the present one in the liquid scintillator mixture.
Data taking, however, did not stop accumulating useful statistics in order to prove the performance of the detector.

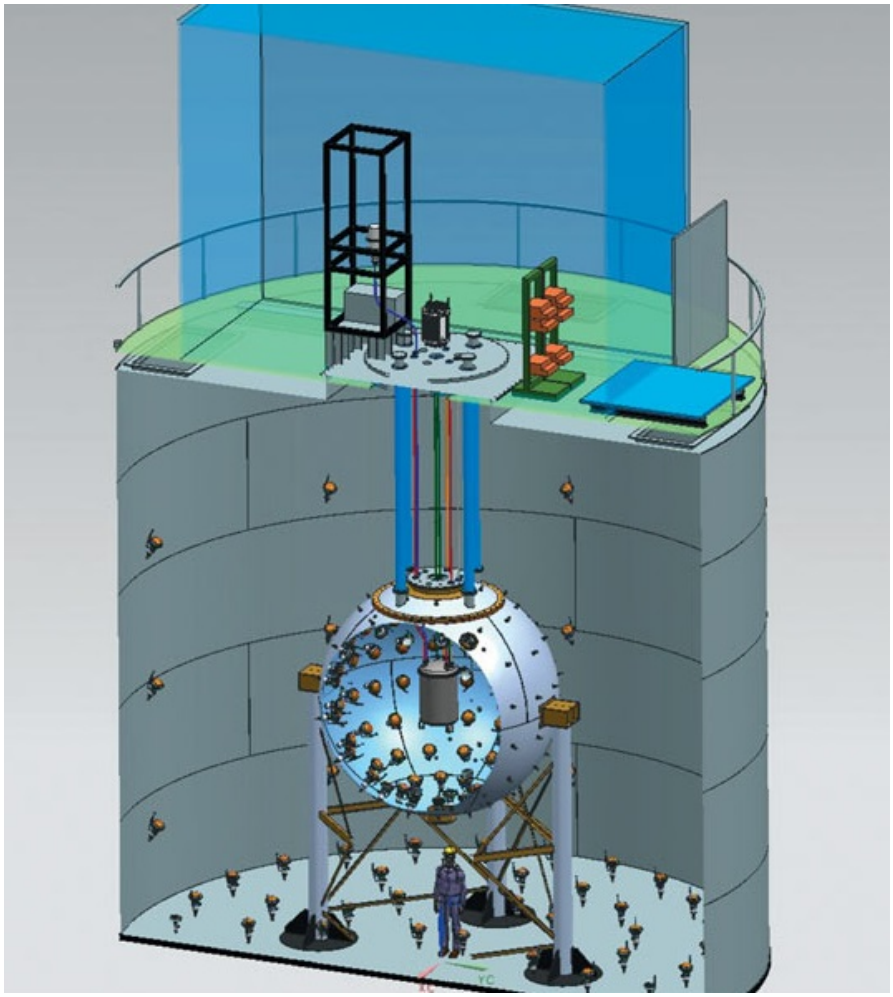

Figure 3.0.2: *DarkSide-50 layout. In the image the water tank with one of the CRH, the liquid scintillator veto. Inside the sphere is hosted the TPC.*

In this chapter both the inner and the outer detector will be described in detail, together with a discussion on the main features of Argon as a DM target.

3.1 Inner Detector

3.1.1 Two-Phase Argon Technology

In this experiment the active medium for WIMP detection is Liquid Argon (LAr). Noble gases are very suitable as target material for DM experiments because they have a high scintillation yield, are easily purified of radioactive impurities and are likely scalable to large masses with relative ease. Among the noble gases, LAr, the active medium for WIMP detection in this experiment, has also excellent ionization and scintillation properties. In fact, a particle can produce, in LAr, more than 10^4 photons per MeV of deposited energy; the time dependence of this scintillation light is different for heavy ionizers (α and n) compared to light ionizers (β and γ) and this can be used to determine which type of excitation occurred for a given event.
If WIMPs exist they are expected to collide with nuclei and produce a recoil nucleus with kinetic energies in the range 0-200 keV. The recoil nucleus causes both excitation of some Ar atoms and ionization of others [33]. The excited atoms produce scintillation through a series of loosely binded dimers

$$\begin{aligned} Ar^* + Ar &\rightarrow Ar_2^* \\ Ar_2^* &\rightarrow 2Ar + \gamma \end{aligned} \tag{3.1.1}$$

whereas ionized atoms, after a sequence of reactions involving electron-ion pairs recombination, de-excite via non radiative processes (releasing heat) and then the Ar_2^* dimers due to the combination of Ar with excited Ar atoms de-excite emitting scintillation light.

$$\begin{aligned} Ar^+ + Ar &\rightarrow Ar_2^+ \\ Ar_2^+ + e^- &\rightarrow Ar^{**} + Ar \\ Ar^{**} &\rightarrow Ar^* + \text{heat} \\ Ar^* + Ar &\rightarrow Ar_2^* \\ Ar_2^* &\rightarrow 2Ar + \gamma \end{aligned} \tag{3.1.2}$$

The processes in equations 3.1.1 and 3.1.2 show how both excitation and ionization mechanism lead to the formation of Ar_2^* dimers. This excited diatomic molecules then decay with the emission of 128 nm (VUV) scintillation photons. Those scintilla-

tion photons are originated from two nearly degenerate states, a long-lived ($\sim$1.6 μs) triplet state, and a short-lived ($\sim$6 ns) singlet state. It has been shown that different particles have different ratios of triplet/singlet states and therefore, the relative amplitude of this fast and slow components can discriminate a nuclear recoil from an electron recoil. The long-lived triplet state is found to be quenched in tracks with low ionization density, thus, electron recoils have a longer scintillation duration compared to nuclear recoils. The rejection and/or classification of events using the time profile of scintillation light is the Pulse Shape Discrimination (PSD). This feature belongs to several noble liquids but it is particularly promising in LAr, due to the large difference between the two decay constants [34].
The double-phase technology, that uses both scintillation light and ionization charge collection, can be exploited to further improve the discrimination between event classes thanks to the different charge to light ratio that they produce. In fact, according to the nature of the primary interaction and to the ionization density, the application of an electric field can affect the recombination probability, decreasing the amount of scintillation light associated to the interaction. The ionization electrons, under the effect of the field, escape from their parent ions, or from the surrounding one, and then are drifted in the TPC to the gas phase where, thanks to a higher electric field, they produce a secondary scintillation and, in this way, their charge can be measured. The efficiency with which the electrons are drifted depends strictly on the purity of LAr, hence the amount of impurities that contaminates the liquid becomes an important parameter of the experiment.
The double-phase technology allows also to identify the position of the interactions and thus, to perform a 3D position reconstruction of the events. Diffusion during the long drift is negligible in liquid noble gas, so the drift time gives the vertical position to sub-millimeter precision, while the pattern of photons on the top photo detector array gives the horizontal position to a precision of less than 1 cm. A 3D position reconstruction is crucial for a fiducialization on the active volume, essential to reject those events too close to the TPC surface. Those could indeed be background events from radioactivity on the TPC inner surfaces that are primarily associated with radon daughters.
Therefore, the combined characteristics of LAr as target material and of the double-phase technology permit to delimit a region in the TPC possibly free from surface events and maximize the ability of discriminating nuclear recoils from electron re-

coils that, in case of a DM experiment, form the most prominent fraction of the background.

A schematic example can be the case of an electron recoil, for which the low density of electron-ion pairs results in less recombination and therefore less scintillation and more free electrons, compared to a nuclear recoil track of high ionization density. Therefore, although electrons are minimum ionizing particles and hence they are expected to have a lower ionization/excitation, the ratio of ionization to scintillation is higher for them than for nuclear recoils. This occurs because the measured charge depends on the extracted ionization, so in a very dense track, such as the one of nuclear recoils, the local field dominate and there is more recombination and less drifting ionization. Clearly what happens in the detector is more complex than what just described in this naive model. The difference in ionization density between nuclear and electron recoils also produces a significant difference in the time profile of the scintillation light. In conclusion, the combination of discrimination by the ionization to scintillation ratio and by PSD provides in a dual-phase LAr-TPC a powerful background rejection [35].

However, the high performances of the background rejection is of little use, or at least not enough in a DM experiment, if together with the gas, a source of electron recoils is also introduced into the detector. Atmospheric Argon (AAr), produced industrially by distillation of liquid air, contains ^{39}Ar , an isotope made by cosmic ray activity. ^{39}Ar has, in air, a relative abundance $^{39}\mathrm{Ar}\ /\mathrm{Ar} = 8 \cdot 10^{-16}$ and it decays β^- ($Q = 565$ keV and $\tau = 388$ years) with an activity of $\sim$1 Bq/kg [36]. The presence of ^{39}Ar does not only increase the background rate, but acting as an impurity, it limits the sensitivity of the experiment because favors electron recombination.

To every problem there is also a solution: Ar extracted from underground sources (UAr) contains a factor of 150 less ^{39}Ar with respect to AAr [37]. The UAr that will substitute the AAr that presently fill DarkSide-50 detector, comes from Kinder Morgan Doe Canyon Complex, a CO_2 extraction plant in Cortez (Colorado). The residual activity of ^{39}Ar in the UAr is 6.5 mBq/kg [38]. The separation of the depleted Ar produced in the Cortez facility from the accompanying Nitrogen and Helium is accomplished by means of cryogenic distillation. The distillation plant, assembled at Fermilab, is currently operating and it is expected to reach the needed amount of Ar in a few months.

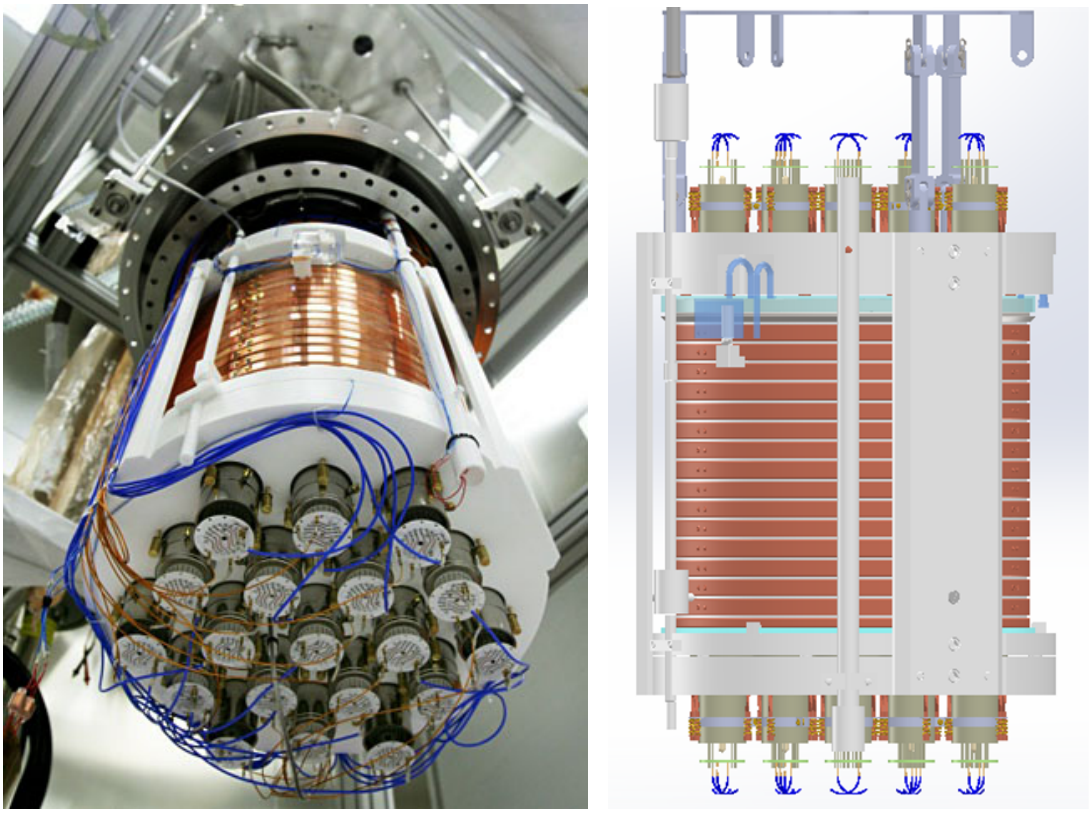

Figure 3.1.1: *On the left a photograph of the LAr-TPC: close-up of the bottom PMTs array and of the copper field shaping rings. On the right is displayed a schematic drawing of the TPC: the diving bel, the field-shaping rings and the PMTs are shown.*

3.1.2 TPC

The core of DarkSide-50 is a dual phase Time Projection Chamber (TPC) made of low radioactivity components and with high light and ionization collection efficiency.

This detector consists of a volume of LAr above which a region of Ar in gaseous phase is present. The equilibrium between the two phases is maintained by vapor pressure. The active volume is constantly monitored by 38 PhotoMultipliers Tubes (PMTs), 19 each on the top and the bottom, that detect the scintillation light produced during both the primary interaction in LAr and the secondary scintillation in the gas phase. The 38 PMTs view the active Ar through fused silica windows, of which the one on the top has a cylindrical rim extending downward to form the diving bell holding the 1 cm-thick gas layer of the LAr-TPC (see figure 3.1.1 right).

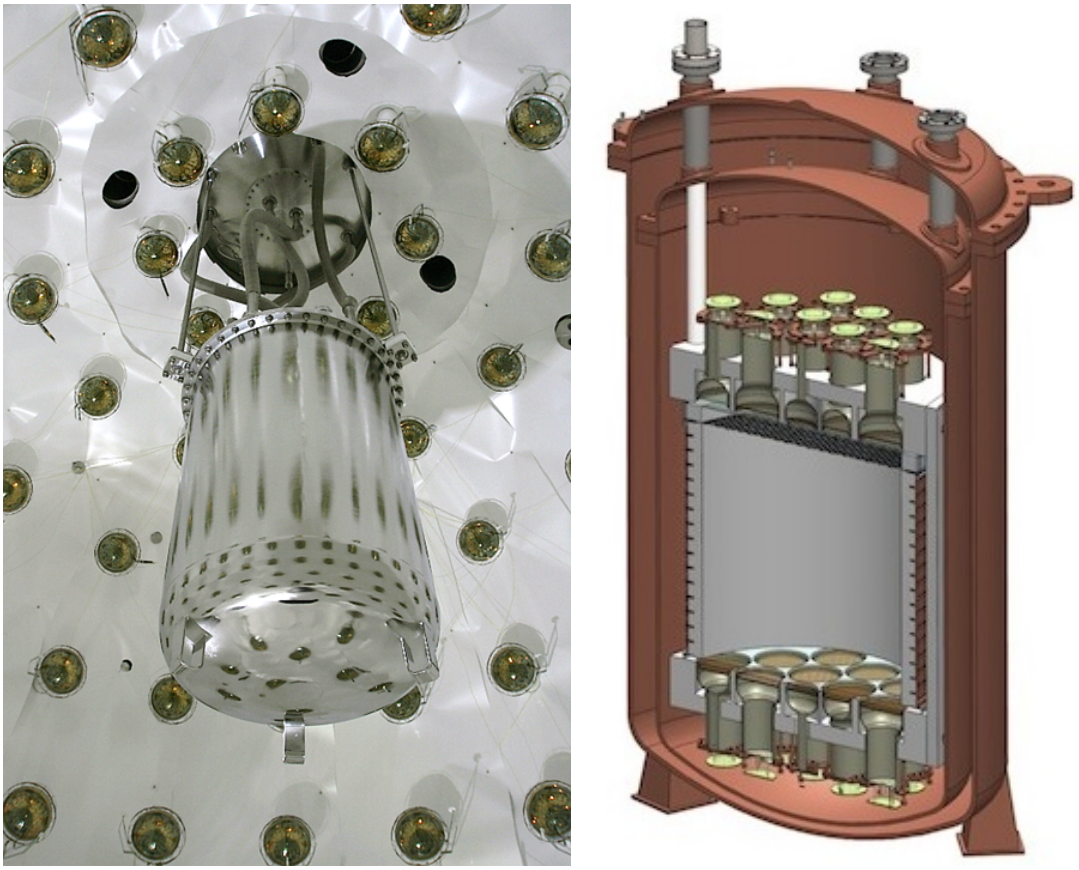

Figure 3.1.2: *Photograph and drawing of cryostat housing the LAr-TPC.*

As anticipated in section 3.1.1, the wavelength of photons due to scintillation in Argon is not within the visible range, where the PMTs are sensitive, and therefore the TPC needs a wavelength shifter. In DarkSide-50 TetraPhenylButadiene (TPB) was used, coated on both lateral surface and fused silica windows, that shift the 128 nm UV scintillation photons to the visible for detection. In figure 3.1.2 a picture and a schematic drawing of the cryostat housing the TPC are shown. The TPC itself and the PMTs are immersed in a buffer liquid Ar surrounding the detector.

In a two-phase TPC, an event is detected by observing both the scintillation photons and the free electrons produced by the primary particle. The scintillation photons are directly detected by the PMTs, while the electrons are drifted upward in the liquid under the influence of a uniform electric field. The electric field is produced by a "field cage" consisting of a cathode plane, field-shaping rings, and an

extraction grid. Anode and cathode consist of a layer of Indium Tin Oxide (ITO) on the top and bottom fused silica window. DarkSide-50 was originally designed to run with an electric drift field of about 1 kV/cm, but recent results from SCENE [39] drove the experiment to run with a much lower drift field of about 200 V/cm. SCENE is an experiment the findings of which have important implications for the DarkSide program and at the moment it is the only neutron calibration available[1]. An electric field of 2.8 kV/cm extracts the electrons into the gas phase, where they produce secondary scintillation photons by a process called "electrolumiescence" (EL) [40].
In figure 3.1.3, a functional scheme of the TPC is displayed. For every type of interaction, the PMTs array first detects the primary scintillation S1, then, after a drift time proportional to the distance between the event position and the gas pocket, a secondary scintillation signal S2. In the TPC the two signals S1 and S2 are recorded within the same acquisition window, where S2 appears as a delayed coincidence relative to S1:

- S1: signal produced by scintillation light due to both excited Ar atoms and recombination of ionization from the primary particle interaction. The amount of photons produced is proportional to the radiative energy deposited in Ar. S1 gives the trigger to both DAQ and vetos.

- S2: signal produced by the non recombined free electrons due to the primary ionization. The uniform drift field present in the TPC drift those electrons (with a speed of approximately 1 mm/μs) to the gas pocket. In this region, thanks to a higher electric field, the electrons, colliding and exciting the gas atoms, produce a second scintillation signal.

In order to reject the background (see section 4.2 for more details), there are three suppression methods applied to the events: the Pulse Shape Discrimination (PSD), the scintillation to ionization ratio and the fiducialization trough the 3D position reconstruction. The first one exploits the S1 photoelectron time distribution, while

[1] The SCENE collaboration has exposed a dual-phase LAr-TPC to a monochromatic, low energy, pulsed, neutron beam at the Notre Dame Institute for Structure and Nuclear Astrophysics to study the scintillation light yield of recoiling nuclei.

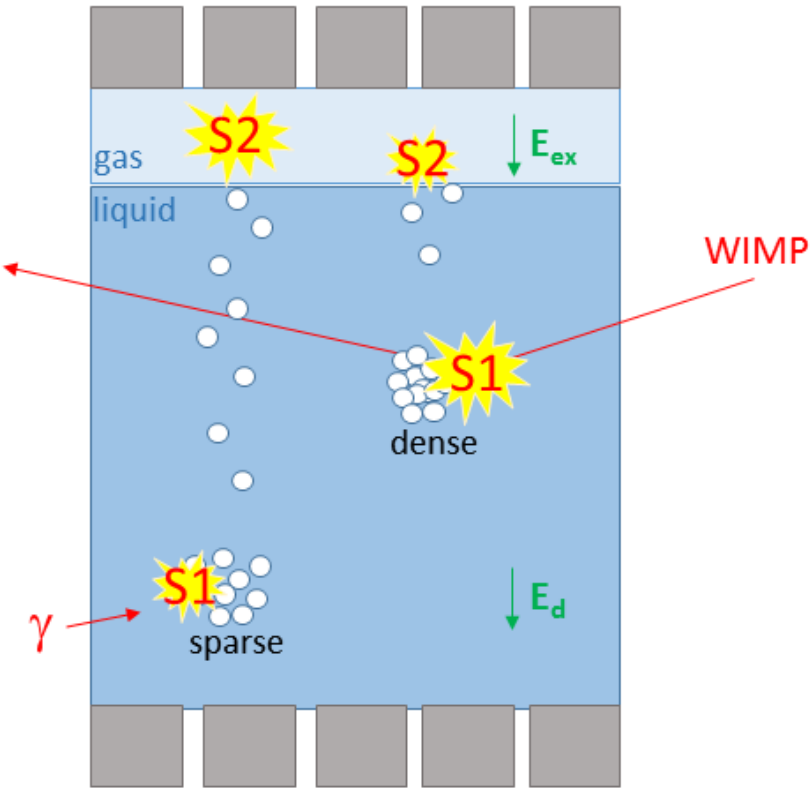

Figure 3.1.3: *Functioning scheme of scintillation and ionization in the TPC.*

the second one uses the ratio between S1 and S2 pulses, which depends on the recombination probability. For example, in case of a WIMP-nucleus interaction as in figure 3.1.3, the recombination probability of ionization electrons is higher than for a β or γ interaction and therefore the S2 signal will be proportional to the S1 instead than greater.

3.2 Outer Detector

The Outer Detectors (OD) consist of a water-based muon Cherenkov detector (WT) and a liquid scintillator one (LSV), serving respectively as muon and neutron active vetoes. The OD was conceived in the DarkSide-50 project in order to host the G2 upgrade without any major modification and with many advantages in terms of costs, detector and background understanding. In figure 3.2.1 an internal view of the muon veto and an external view of the neutron veto during the construction phase are shown.

Figure 3.2.1: *Internal view of the CTF muon veto. The LSV neutron veto that houses the TPC is situated in the center.*

3.2.1 Muon Veto

The muon veto is the most external part of the DarkSide-50 experiment. The cylindrical WT that constitute the muon veto is the former Counting Test Facility (CTF)

[41] of the Borexino experiment [42]. It is a Cerenkov detector 10 m high with a diameter of 11 m, filled with ultra-pure water and instrumented with 80 8–inch PMTs on the lateral walls and on the pavement.
The muon veto, as the name suggests, is used to identify energetic muons and acts also as passive shielding for external neutrons and gammas. Cosmogenic muons themselves do not represent, in general, a dangerous source of background because, having an energy in the GeV range, the energy that they release in the detector is higher compared to the region of interest. Muons, however, produce, via spallation processes, neutrons which energies are above those of radiogenic neutrons and therefore are more difficult to attenuate. Whereas at LNGS the expected rate of cosmogenic neutrons is about 10^{-33} Hz per target nucleus, the expected rate for WIMPs is approximately 10^{-34} Hz, from here the necessity to attenuate or tag those neutrons. Unlike radiogenic neutrons from the rock of the underground cavity and from the surrounding materials, cosmogenic neutrons have such high energies that cannot be always attenuated or captured by the neutron veto and therefore their detection relies on the detection of the parent muon passed through the water tank.
To enhance the light collection and increase the efficiency of this detector, a reflector made of a Tyvek-Polyethylene-Tyvek sandwich, covers the inner surface of the tank and the external surface of the neutron veto, as shown in figure 3.2.2.

3.2.2 Neutron Veto

The purpose of the LSV is to complement the WT in muon vetoing and to act as an active veto for neutron and gammas. It is extremely important for the experiment to be able to tag neutrons because they could produce a nuclear recoil and therefore a signal that mimic the WIMP-nucleus interaction. In fact, a nuclear recoil caused by a neutron cannot be rejected using the PSD or the ratio S2/S1, but it has to be rejected by the neutron veto.
The neutron veto is a 4 m stainless steel sphere filled with liquid scintillator (see figure 3.2.3 for an internal view). The sphere is instrumented with 110 8-inch low-radioactivity and high quantum efficiency PMTs, for a 7% photocathode coverage. The internal surface of the LSV sphere is covered with Lumirror, a high reflectivity (>95%) material used to collect the light that does not directly hit the PMTs and thereby maximizes their efficiecy.

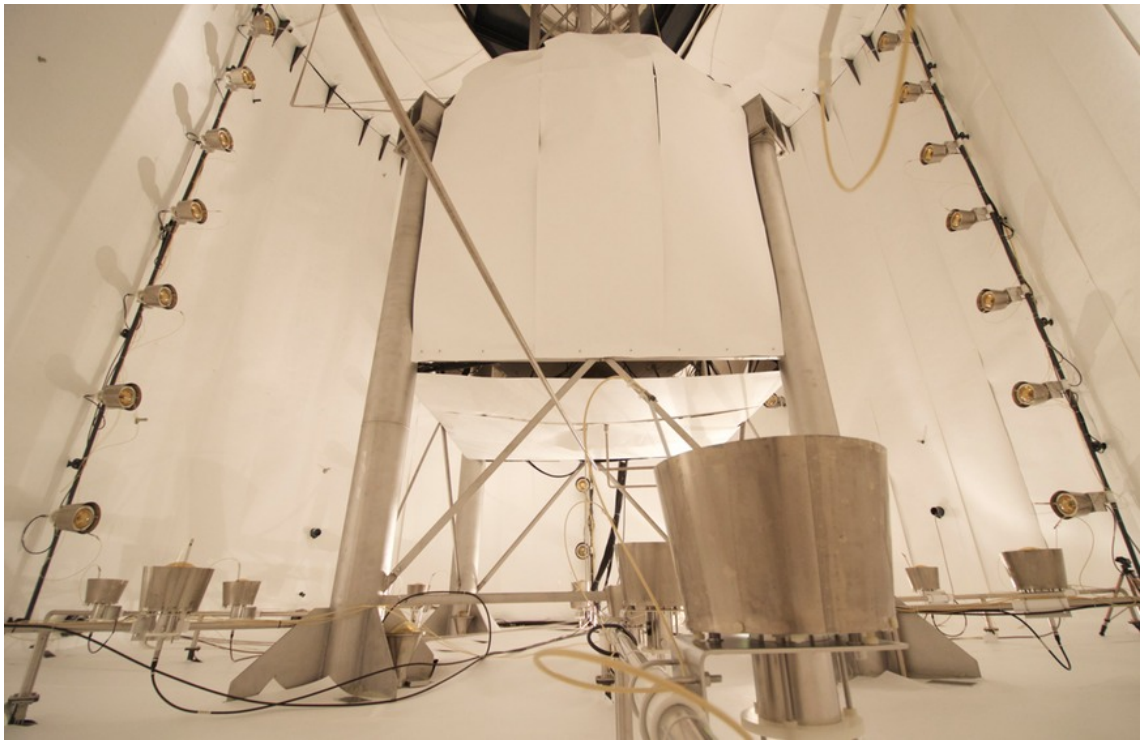

Figure 3.2.2: *Internal view of the CTF muon veto and LSV neutron veto. Almost the whole surface is covered with a white layer, a reflector made of Tyvek-Polyethylene-Tyvek sandwich.*

The liquid scintillator is a 1:1 mixture of a solution of PseudoCumene (PC, 1,2,4-trimetilbenzene) and TriMethylBorate (TMB). The PC has been doped with 3 g l^{-1} of PPO (2,5-difeniloxazolo). Charged particles loosing energy in the scintillator PC+PPO cause mostly excitation and ionization of PC molecules while PPO molecules are excited by energy transfer processes such as absorption of PC emitted photons and, more often, dipole-dipole interaction between excited PC molecules and a PPO molecule. Therefore, the fluorescence light is emitted from the de-excitation of PPO electrons. However, the amount of light is not proportional to the total energy deposited by the particle, but also depends on how this energy is dissipated: when the dE/dx is very high, some non radiative processes are favored. This behaviour is described by the quenching factor Q(E).
The role of TMB in the liquid scintillator mixture instead favors neutron capture on ^{10}B , producing α particles of energy 1.47 MeV or larger. This is the dominant process in the liquid, due to the large thermal neutron capture cross section on ^{10}B the

Figure 3.2.3: *Internal view of the neutron veto. In this photograph some of the 110 PMTs can be seen, together with the high-reflectivity Lumirror.*

natural abundance of which is 20%. The cross section for (α, n) reaction in ^{10}B is, in fact, three orders of magnitude greater than a neutron capture cross section on protons or on ^{11}B. The fact that α are very short range particles is a critical point in order to have an efficient neutron detection without requiring very large veto volumes. The energy deposition in the scintillator due to a neutron capture on ^{10}B is at least 60 keVee (keV β-equivalent) [43], which results in high detection efficiency. This, together with the short neutron capture time, makes it possible to operate the veto with a high event rate, allowing for a direct immersion of the PMTs in the scintillator without an additional inert buffer layer.
Considering the quenching factor and a quantum efficiency of about 35% for the PMTs, a light yield (LY) of 0.5 PE/keVee was obtained. This means that the average signal for a neutron capture is about 30 PE, ensuring very efficient neutron detection.

Chapter 4

Analysis of Early Data

Before the filling of the detector with UAr it has been taken advantage of the presence of AAr, with its high rate of electron recoils due to the decay of ^{39}Ar , to investigate aspects of the detector still not very clear. In fact, since AAr contains 150 times more ^{39}Ar than UAr, it is possible to accumulate in a short time the same amount of electron recoils that the one obtained in a future longer run with UAr. Particularly, in 6.3 days with AAr DarkSide-50 is expected to acquire a number of electron recoil events corresponding approximately at the amount of data that it will accumulate in 2.56 years with UAr. This means that with the statistics obtained in this short period of time it is possible to measure the capability of suppressing electron recoil background by PSD and to make predictions on the performance of the experiment over more than 2 years of data taking with UAr.
In this chapter a closer look at the first data acquired by DarkSide-50 is provided. An introduction on the main steps to arrive at the final reconstructed events starting from the raw data and then an over all overview of the quality cuts necessary to obtain the final set of data used in higher level analysis, is also discussed. It follow a detailed study of various kind of background and a dissertation on how DarkSide-50 rejects them and how to estimate the ^{222}Rn activity in the detector using the delayed coincidence method. The second half of this chapter is dedicated to the description of the main features of this experiment that influence the limit in the parameter space (σ_n, M_W), and then a projected sensitivity for DarkSide-50 based on the data taken so far is shown. Once a projection of DarkSide-50 sensitivity has been outlined, the same projection could be done also for DarkSide-G2, given a high

enough statistics to cover a period of time of 5 years. This is the reason why in the last section the feasibility study of an ^{39}Ar spike is presented: in case of a positive outcome, this spike would provide the statistics necessary to calculate a projected limit, in the exclusion plot, for DarkSide-G2.

4.1 Data Reconstruction and Quality Cuts

4.1.1 DarkArt

In DarkSide-50 the raw data coming from the TPC data acquisition system pass through a low-level reconstruction chain called DarkArt. The main role of DarkArt is therefore the translation of the digitized PMT traces into reconstruction variables that can later be utilized for high-level analysis such as energy calibration, single photoelectron studies, PMT stability, optimization of the cuts background rejection and, the most important, search for DM. The DarkArt software is organized in modules each one of which performs a specific task, from the decompression of the raw data files to the final data products that are stored in each art::Event.
The main steps that the reconstruction algorithm has to fulfill in order to return the final reconstruction variables, are, basically, the following:

- Decompression of the raw data files produced by ds50daq[1].
- Retrieval of raw data information for an event (number of samples for each channel, event ID, trigger time stamp and some other channel-level information).
- Search of the baseline with module BaselineFinder: because the DC offset level of the digitizer is semi-arbitrary and because of the presence of noise fluctuations with a time scale of the order of microseconds, this module can not simply assume that the baseline level is a constant but has to identify the baseline oscillations and interpolate over the signal regions (an example is shown in figure 4.1.1). Subsequently, after applying a drifting baseline algorithm to the raw data this module gives back a baseline-subtracted waveform.

[1]DAQ software package for DarkSide-50 built on FNAL's artdaq.

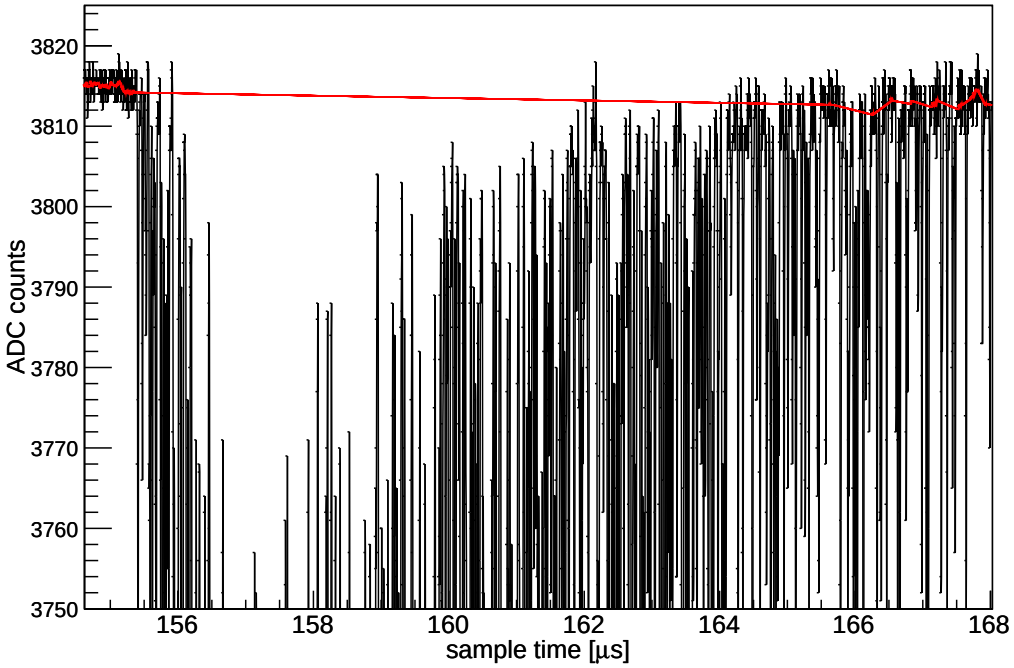

Figure 4.1.1: *Single channel waveform showing baseline interpolations over an S2 signal region.*

- Region of interest finder (RoiFinder) is a module the role of which is to define fixed regions in time and compute, for each channel, integral, maximum and minimum values and their correspondent times.

- Creation of a virtual sum channel scaling the signal of each channel by its mean single photoelectron response and storage of zero-suppressed waveforms: in this case the zero-suppression has been used because the baseline noise adds coherently across all channels and can easily bury single photoelectrons[2].

- Finding pulses with the module SumPulseFinder: it identifies signal regions using zero-suppressed sum channel, without making any assumptions on the number or duration of the pulses. A pulse is recognized by several photons

[2]The zero-suppressed waveforms are used only for pulse finding and not for computing any variables.

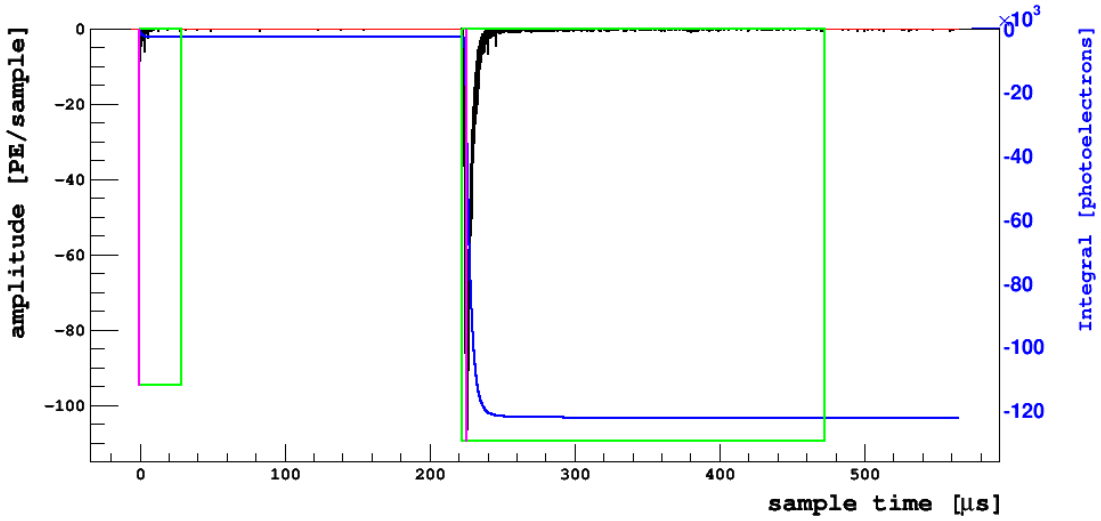

Figure 4.1.2: *Example of a waveform: sum channel of event 80 - run 5475. The blu line is the integral waveform; the two green boxes delimit the pulses found in this event; the two magenta vertical lines indicate the peak of each pulse.*

arriving within the same short time window that cause a sharp change in the slope of the integral waveform and in its first and second derivative. Once the pulse has been found, the algorithm goes back seeking for the value of the amplitude that overcomes a certain threshold and marks the start of the pulse, then it passes the maximum and, if no pile up is present, it looks for the end of the pulse where the curvature returns under a fixed threshold. In the case in which pile up is found, the module is more meticulous in looking for the end of the first and the beginning of the second pulse. In figure 4.1.2 is reported an example of the sum channel for a waveform where the two pulses have been found: in the figure each pulse is delimited by a green box.

- For each channel independently, computing with the PulseParameter module all the parameters of the pulses found on the sum channel. This physical variables, that will be discussed in detail in the next paragraph, are calculated for all pulses without questioning what type of pulse they are, to ensure that all necessary information is recorded. Some of the physical values of particular interest are the integral over the full range of the pulse and over some fixed ranges of time, the number of photoelectrons (integral scaled by the channel's

SPE mean) and few ratios of the first nanoseconds of the pulse to the total integral. The same variables are obtained also for the sum channel, but by a different module.

- Building the event-level by computing the same variable as in the previous step, but by summing the pulse values of all physical channels as shown below (the sums run over the physical channels):

$$\texttt{integral} = \sum_i \texttt{integral}_i \quad [\texttt{counts} \times \texttt{samples}] \tag{4.1.1}$$

$$\texttt{fixed\_int1} = \sum_i \frac{\texttt{fixed\_int1}_\texttt{i}}{\texttt{spe\_mean}_\texttt{i}} \quad [\texttt{counts} \times \texttt{samples}] \tag{4.1.2}$$

and so on for all the parameters.

4.1.2 Reconstructed Variables and Their Interpretation

The final product of DarkArt is a ROOT file. This file contains `EventData` where all the parameter values computed by DarkArt modules are stored and are easily accessible for the user who can then proceed with high-level analysis. It is only at this point of the analysis, after the reconstruction, that we start using physical variables.
From a standard event, such as an electron recoil in the bulk of the TPC, one expects two pulses: a first one (S1) due to the scintillation in LAr and a second one (S2) due to the scintillation in GAr, separated from S1 by a drift time (`t_drift`) proportional to the distance between the location of the interaction and the extraction grid; 10 μs corresponds to approximately 1 cm in the TPC z axis. The first pulse of each event (see for an example figure 4.1.3) is assumed to be an S1, thus the most useful parameters computed for this pulse at the event-level are:
`pulses[0].param.npe`: total number of PE within the pulse range;
`pulses[0].param.f90`: fraction of the total integral in the first 90 ns[3];
`total_s1 = pulses[0].param.fixed_int1`: integral of the pulse in a fixed window of 7 μs;

[3] Actually the f90 is the fraction of the first 88 ns, since the time resolution is 4 ns.

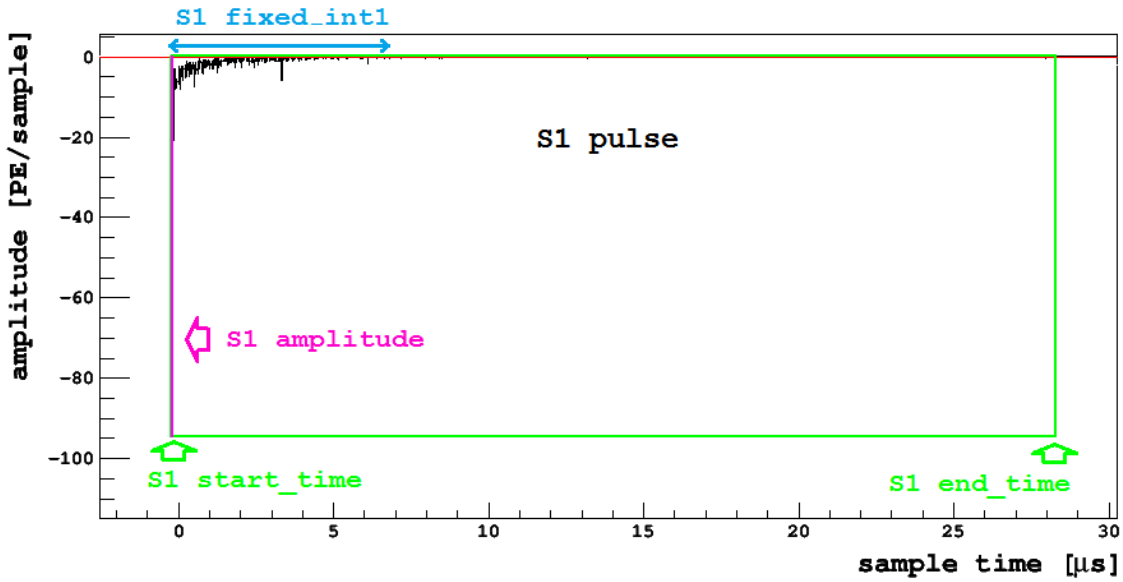

Figure 4.1.3: *This is the zoom in of the first pulse of the same waveform shown in figure 4.1.2: on the waveform are indicated some of the most important parameters.*

`total_f90` $= \frac{\texttt{pulses[0].param.f90} \times \texttt{pulses[0].param.npe}}{\texttt{total\_s1}}$: f90 with respect to the fixed 7 μs time window;

`pulses[0].pulse.start_time`: starting time of the S1 pulse in μs.

The second pulse (see for an example figure 4.1.4) is assumed to be an S2 for which the following parameters are computed:

`pulses[1].param.npe`: total number of PE within the pulse range;

`pulses[1].param.f90`: fraction of the total integral in the first 90 ns;

`total_s2 = pulses[1].param.fixed_int1`: integral of the pulse in a fixed window of 30 μs;

`total_f90` $= \frac{\texttt{pulses[1].param.f90} \times \texttt{pulses[1].param.npe}}{\texttt{total\_s2}}$: f90 with respect to the fixed 30 μs time window;

`pulses[1].pulse.start_time`: starting time of the S2 pulse in μs.

For each event the drift time and the ratio S2/S1 are also calculated, together with other variables apt to identify the channel that received a fraction of light higher than its neighbors. Note that the maximum drift time when the TPC is operated

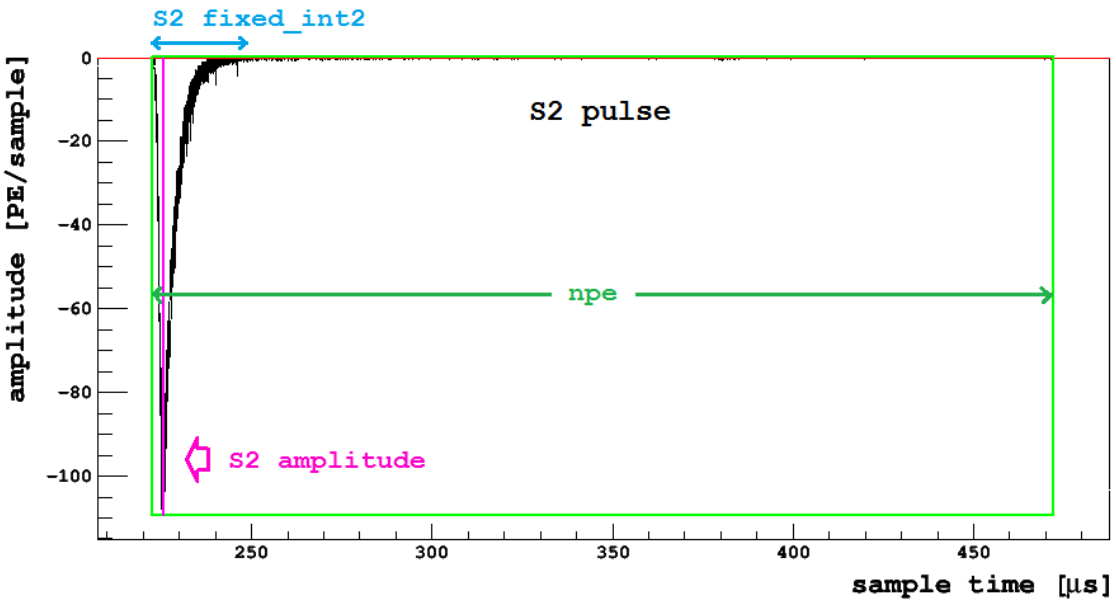

Figure 4.1.4: *This shows a zoom in of the second pulse of the same event of figure 4.1.2 and 4.1.3. Note that the time scales are different in the two images.*

at 200 V/cm is `t_drift_max = 376` μs.
`t_drift = pulses[1].pulse.start_time - pulses[0].pulse.start_time`: time between S1 and S2 due to the electrons drift time in the TPC;
`s2_over_s1 = total_s2 / total_s1`: ratio between the integral of the two pulses;
`max_s1`: maximum s1 integral found by looping over all the physical channels, from 0 to 37;
`max_s1_chan`: channel that received the maximum fraction of light for the event;

The last two variables are crucial to eliminate events which light is concentrated on a single channel, therefore, as described in the next paragraph, events that happen on the fused silica windows and on the PMT photocathodes. Figure 4.1.5 displays for one event all the waveforms of some of the channels separately; in particular one can notice that channel 25 receives more light than the others, meaning that the event happened close to that PMT.

There are of course events with more than two pulses: this is because of multiple

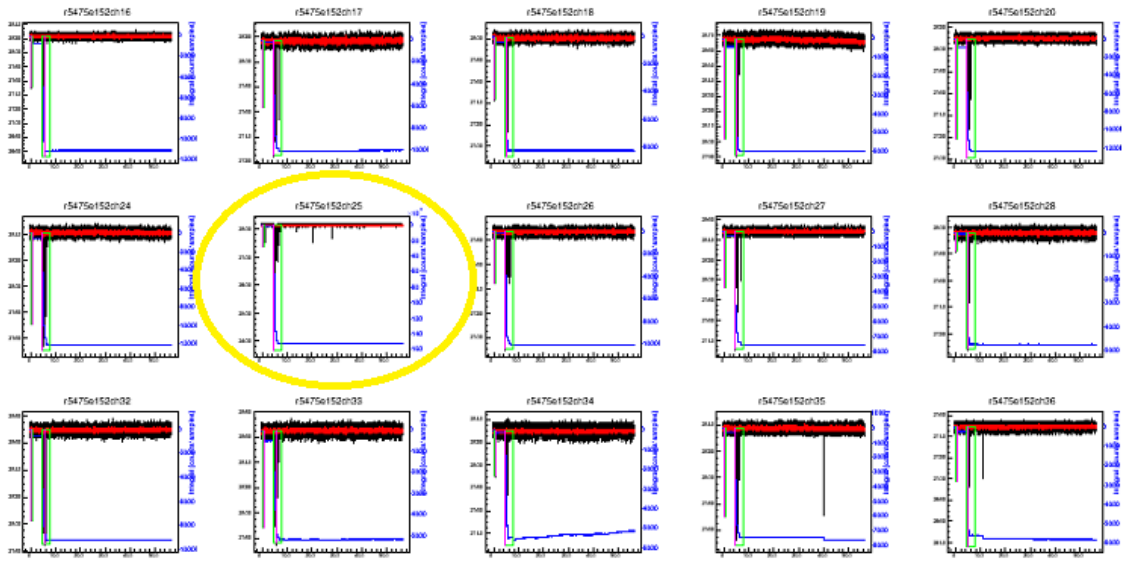

Figure 4.1.5: *The image displays some of the single channels for an event. The channel that received more light is circled in yellow: it is possible to state this because the amplitude is much bigger than all the others and therefore the baseline seems thinner.*

scatters or because of random pile up of events, due to the high rate of ^{39}Ar . These events are skipped by standard analysis. However, some specific analyses such as the delayed coincidence method, are designed to look at cases of more than three pulses and their pulse-identification algorithms will be described in the dedicated sections.

4.1.3 Standard Analysis Cuts

Higher-level analysis typically takes the form of various ROOT macros, each specialized to carry out specific analysis tasks. However, no matter what kind of analysis one wants to perform on the data, it is not possible to use all the events as they are. There are indeed events that miss a channel, or in which the baseline was not found, or more, there are many S2 due to multiple scattering and so on. Accordingly, there are some basic cuts that are applied to the events at the beginning of every macro, designed to ensure that the event does exist and that it is readable by the macro.

These first basic cuts will be described at the beginning of this paragraph. Then an overview of all the quality cuts will follow, after which it is already possible to fill the main plots used by DarkSide-50 in the search of DM.

- **Number of channels basic cut**: the events that do not have all channels available because one or more of them has not been stored in `EventData` are rejected with this cut.

$$\texttt{event.channels.size}() == 38$$

- **Baseline basic cut**: when the channel baseline is not found no reconstruction is performed and therefore there are no variables stored in the `EventData` for that channel.

$$\texttt{event.sumchannels.baseline.found\_baseline} == \texttt{true}$$

- **Trigger time cut**: events for which the start time of the first pulse falls outside the expected trigger position in the DAQ window are not suitable for high-level analysis. The events excluded by this cut have in the pre-trigger portion of the waveform some other pulse such as tails of previous events and therefore the `pulses[0]` is not an S1.

$$-0.25\mu\text{s} \leq \texttt{pulses}[0].\texttt{pulse.start\_time} \leq -0.18\mu\text{s}$$

- **Single hit cut**: events that fail this cut are the ones with a number of physical pulses different from two. This means that only events with one S1 and one S2 are allowed for standard analysis.

$$\texttt{n\_phys\_pulses} == 2$$

- **Max fraction of light cut**: only pure scintillation events will pass this cut. This will remove part of the interactions outside the fiducial volume (the rest will be eliminated by fiducialization), for example Cherenkov interactions in the quarz windows (of the TPC or PMTs) and combined events with both Cherenkov light and a Compton interaction in the sensitive volume. This cut,

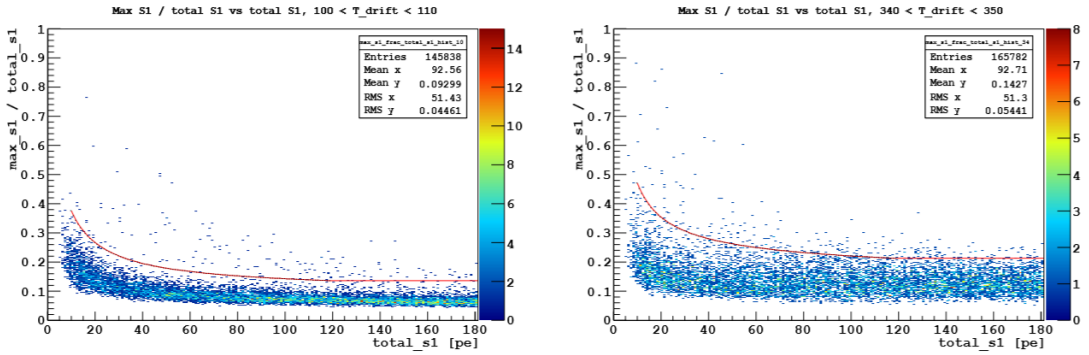

Figure 4.1.6: *Distribution of* `max_s1/total_s1` *as a function of* `total_s1`*. Two of the 35 slices in drift time are here displayed. The events above the red line fail the cut because they have a high fraction of light concentrated on one channel only.*

developed using all events that pass basic cuts, is based on the fraction of light concentrated on a single channel: this is a function of the z position (or equivalently of `t_drift`) of the event in the TPC and of its energy, therefore the distribution of the maximum fraction of light (`max_s1/total_s1`) has been sliced in z and for every slice an appropriate cut of the `max_s1/total_s1` for each `total_s1` interval has been performed. In figure 4.1.6 two of the 35 slices in drift time are displayed: the red line marks the bound beyond which the events fail this cut. The limit has been set in such a way that ony 2% of events in any given `total_s1` bin is expected to overcome the upper limit of the `max_s1` distribution just for statistical fluctuations, without taking any assumption on the behaviour of the distribution at all energies.

- **Saturated S1 cut**: events that saturate the ADC during the primary pulse are removed. Saturation could falsify the energy spectrum starting from a `total_s1` of about 1600 PE.

$$\texttt{event.pulses[0].param.peak\_saturated} == \texttt{false}$$

- **Livetime cut**: if two events are too close in time tails of the S2 of the first event, could cause the trigger of a second event. Figure 4.1.7 shows in red the logarithm of the livetime expressed in seconds. By requiring a value of the livetime above -3.75 the first peak can be removed and with it the events that do not trigger on S1.

$$\texttt{log10}(\texttt{event} \rightarrow \texttt{event\_info.live\_time\_20ns} * 20. * 1.\texttt{e} - 9) < -3.75$$

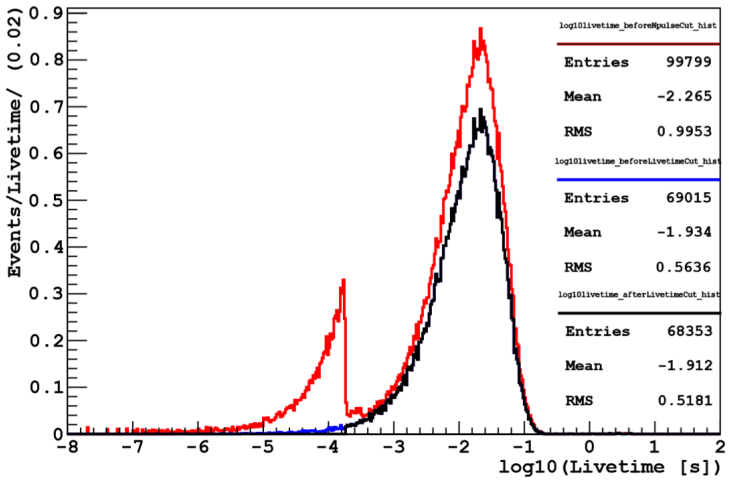

Figure 4.1.7: *Histogram of the logarithm of the livetime expressed in seconds. This cut removes the first smaller peak which are the events triggered on tails of previous S2.*

After this last cut it is possible to visualize the remaining events and study them via three plots: total spectrum, f90 and S2/S1. Due to the immaturity of the S2 analysis results related to S2/S1 rejection will not be presented: nevertheless information coming from secondary signals has been widely used to perform cuts. The scatter plot of f90 as a function of the S1 energy (in PE) will be widely discussed in the next section since it is the core of background rejection. Here in figure 4.1.8 the total energy spectrum is presented after all the cuts have been applied to the data collected during the first 6.3 days (livetime) of data taking with AAr.

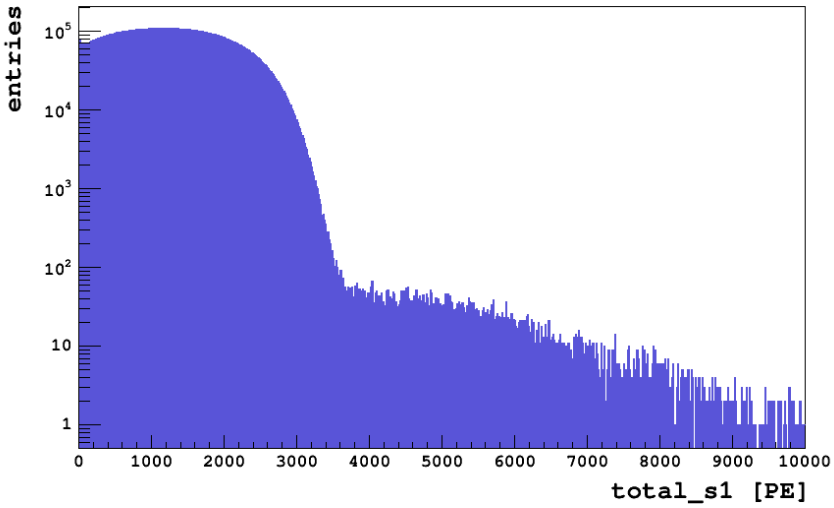

Figure 4.1.8: *Spectrum of the events passing all the standard analysis cuts. As expected this spectrum is dominated by* ^{39}Ar β *decays.*

4.2 Background Rejection

In this section the pulse shape discrimination (PSD) performance for DarkSide-50 and its efficiency in background rejection will be presented. The PSD in Argon and the low ^{222}Rn activity are two of the strongest points of DarkSide-50, thus they deserve particular attention.
Although there are some promising techniques for DM searches in the presence of background, the best sensitivities have been achieved with experiments that try to suppress the background to negligible levels. The DarkSide program is one of those experiments: it expects DM signals (nuclear recoils) in a background free region, where no other signal is expected. Therefore, since the predicted collision rate of WIMPs on target nuclei is very low, DarkSide-50 requires an ultra-low background level in the detector.
The underground location and the careful cleaning in clean room of all the detector materials already eliminated most of the cosmogenic and radiogenic background respectively. A small fraction of the background is then due to residual cosmogenic muons and neutrons. Most of the cosmogenic neutrons are arrested by the water tank, that acts as passive shielding; the rest of the cosmogenic background is rejected thanks to coincidences with the OD (muon and neutron veto).
However, this is not enough to have a background free experiment: there are still many background sources that are inside the detector, such as decays from ^{39}Ar and radioactive contaminants, and can not be eliminated ahead of the data taking. Accordingly, the main part of background rejection occurs during high-level analysis of TPC data using PSD, as it will be demonstrated in the next two paragraphs.

4.2.1 Pulse Shape Discrimination (PSD)

In DarkSide-50, the PSD is performed using the prompt fraction of pulses via the parameter f90. The f90, already mentioned in paragraph 4.1.2, is defined as the fraction of total number of PE included in the first 90 ns of S1 pulses.

$$f90 = \frac{\int_0^{90ns} npe}{\int_0^{endofpulse} npe} \tag{4.2.1}$$

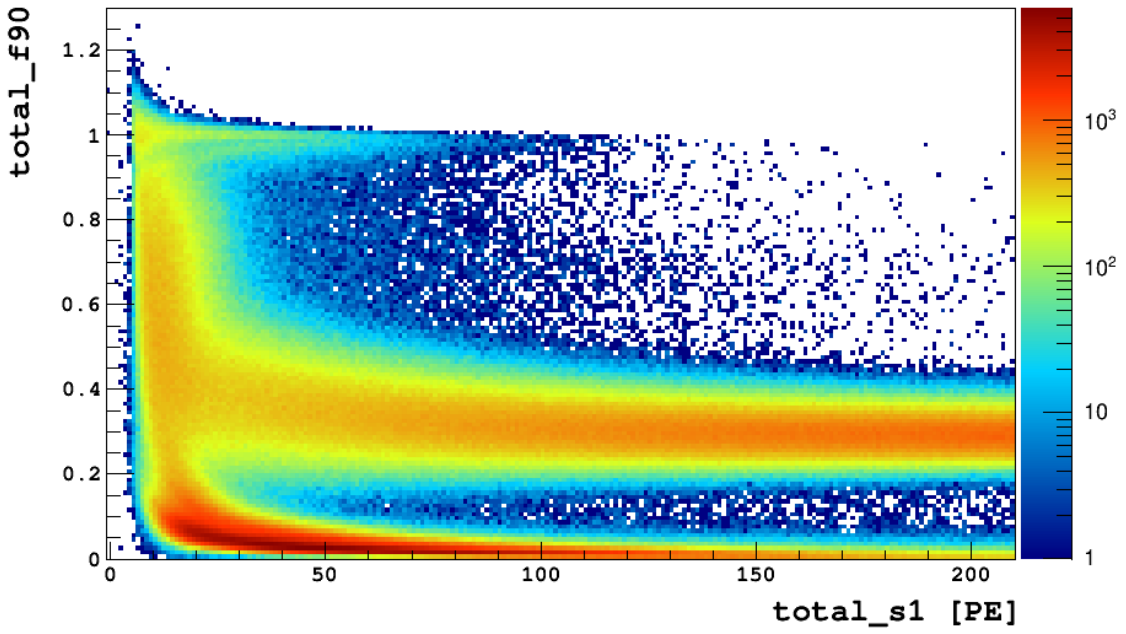

Figure 4.2.1: *This plot represents the distribution of the events in the f90 versus S1 integral, before any cut. The total entries for this histogram are 30 million events. The z axis is set in logarithmic scale.*

It is important to underline that PSD using f90 is only valid for S1 pulses, whereas S2 can contribute at the PSD through the parameter S2/S1. In any case it can be interesting to know that the f90 of S2s ranges from orders of 10^{-5} up to 0.1.
Distinct particles interact with different speeds in LAr, hence f90 takes advantage of the variation of rise time that characterizes S1 peaks caused by various background sources. We will refer to fast events as the ones with a high f90 (closer to unity) while we will call slow events those with a low f90. For example nuclear recoils are considered fast events since their f90 is approximately around a value of 0.7 while β and γ events are slower and their f90 value sets around 0.3. Following the same criteria, Cherenkov events can be isolated because they are so fast that their f90 often get a value around 1.

In order to give a better idea of what we are referring to, one can observe the next two plots annexed to this section: the first plot here presented, figure 4.2.1,

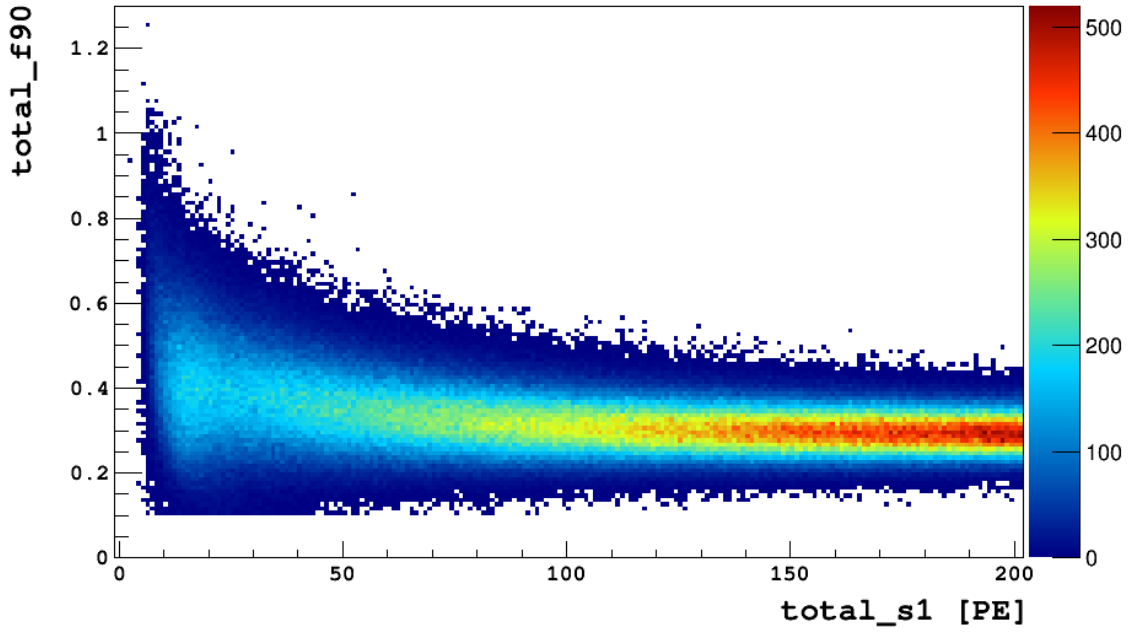

Figure 4.2.2: *This second f90 versus S1 integral plot shows the distribution of the events after all cuts have been applied.*

shows the 6.3 days campaign data before any cuts in a plot of f90 as a function of S1 energy (in PE) , while the second plot, figure 4.2.2, displays the same histogram as before, but obtained with the final set of data, after all the cuts enumerated in section 4.1 have been applied. Both distributions display only the first 200 PE of the total S1 energy range. In the first plot three bands can be clearly distinguished: from the bottom, the first band consists of events triggered on S2; the second one is the electron recoil band; and the top one is probably caused by Cherenkov events. A nuclear recoil band has not been observed yet nor single nuclear recoils.
β and γ radiation are potentially the most problematic background for direct dark matter experiments, because of its penetrating power and because of ^{39}Ar high rate. In the specific case of this first phase of DarkSide-50, the internal component of the rate due to ^{39}Ar β decay (exposed in figure 4.1.8) is about 1 kg^{-1} s^{-1} and therefore dominates by a factor 100 the external component, which is about 10^{-2} kg^{-1} s^{-1}. However, thanks to the discrimination power of PSD in LAr the electron recoil band is well separated from the nuclear recoil one as determined by other experiments us-

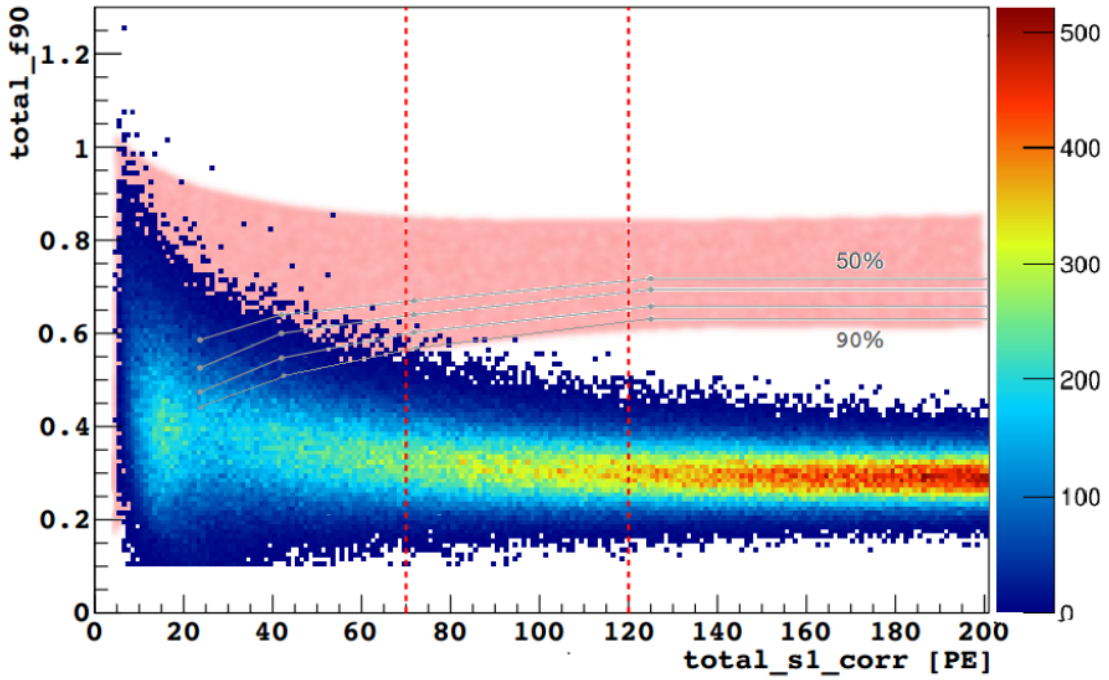

Figure 4.2.3: *Distribution f90 versus energy, obtained by the DarkSide collaboration after 6.3 days of data taking. In red a qualitative projection of the nuclear recoil band is superimposed to the electron recoil band recoil band; the nuclear recoil band correspons to the expected WIMP signal region.*

ing LAr TPC and performing a neutron calibration. Figure 4.2.3 shows the f90 distribution as a function of energy obtained so far by DarkSide-50: the red band superimposed to the scatter plot is a qualitative interpretation of the nuclear recoil band obtain by SCENE, which acceptances curves are reported in gray. The gray lines represent from top to bottom the median and the 65%, the 80% and the 90% of the SCENE nuclear recoil distribution. The nuclear recoil band represents the region of interest for the WIMP search. It is noticeable that at low energies the nuclear recoils band has a descendant trend and, below 60 PE, it merges with the electron recoils one and therefore, below a certain energy threshold, it is not possible to perform any background rejection.

4.2.2 Alpha Background

In principle α decays are the easiest background component to remove because, even though their f90 is in the range of nuclear recoils, the energies involved are out of the region of interest. In addition, with a good x-y reconstruction, which is still under development, it is possible to exclude all those events not coming from the fiducial volume, included αs from TPC surface. Nevertheless, until the x-y reconstruction is fully operative, the presence of α decays remains a problem, hence studying the α background inside the TPC remains an essential task. Furthermore, this study can help in identifying contamination from natural radioactivity in the LAr or on the surface of detector materials.

Naturally occurring radioactivity is dominated by ^{40}K decays and from the ^{238}U and

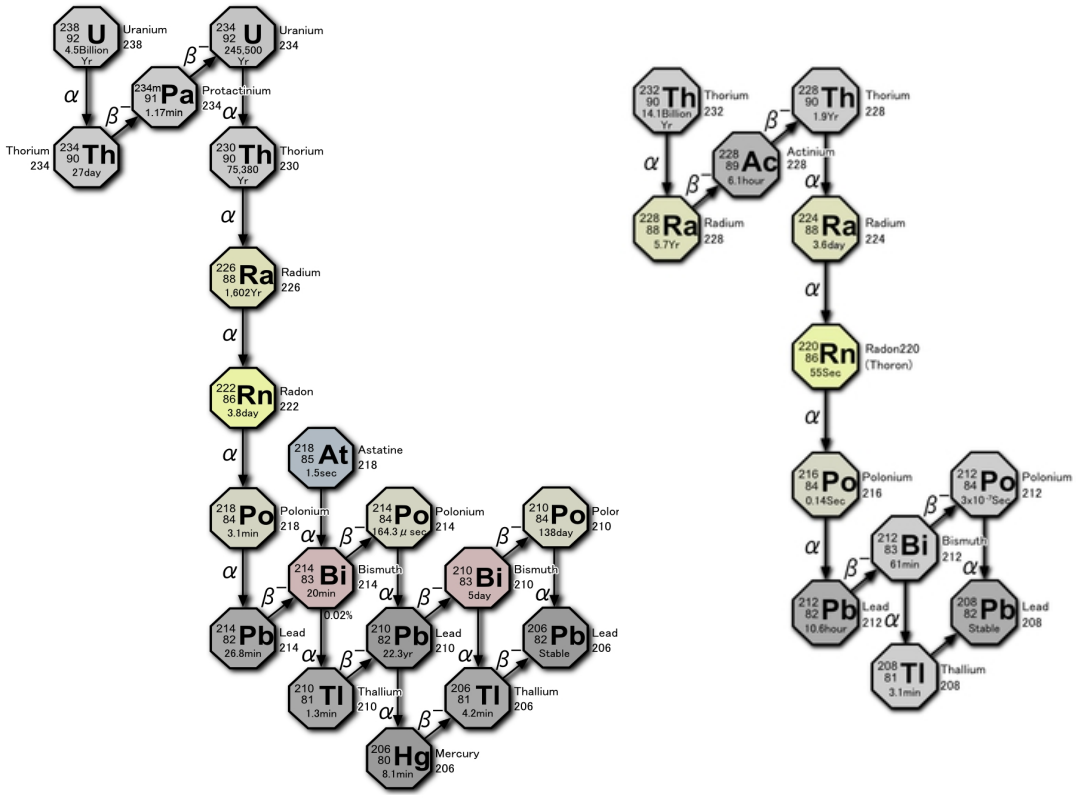

Figure 4.2.4: ^{238}U and ^{232}Th chains

^{232}Th chains, which include several long-lived isotopes. Figure 4.2.4 shows the

^{238}U and ^{232}Th chains, featuring isotopes emitting γ radiation up to 2.6 MeV in energy, α particles between 5 and 8 MeV, β and neutron radiation. Within the α-emitting radioactive background, particular attention will be given, in the next section, to ^{214}Po decays which identification permits to estimate the presence of ^{222}Rn in the detector.
Moreover, α decays on the surface of detector materials can produce a dangerous background source, in cases in which the α is absorbed by an inactive material such as the side reflector by emitting a neutron, which is then released into the LAr providing a signal that mimics a WIMP recoil.

Runs

The runs used in this analysis are of background type, acquired between November 2013 and the end of January 2014. They all have a majority trigger of 3 channels, a drift field of 0.2 kV/cm and an extraction field of 2.8 kV/cm but they were acquired with different DAQ windows, with length varying in the range 470 μs - 570 μs.
The total livetime for these runs is approximately 151 hours, or 6.3 days.

Cuts

As far as the cuts applied in this analysis are concerned, in this section are described only those that differ from the standard analysis cuts described in section 4.1.3.

- **Number of pulses**: contrary to the standard analysis where the cut on the number of pulses allow only events with one S1 and one S2, this time the number of pulses cut has been relaxed and set to a maximum of four pulses allowing not only single hits with S1 and S2 but also random coincidences with other events.

  ```
  event.sumchannel.pulses.size() < 5
  ```
  (4.2.2)

- **Max fraction of light cut**: this cut is implemented for the same purpose as in section 4.1.3, to remove non pure-scintillation events in which part or all the light produced does not come from the sensitive volume. However, here we loosen this cut somewhat for two reasons: one, there is only a small population of αs to study and so we would rather prefer more bad events to pass the cut

than lose any alphas to it, and two, these α events may produce light that is distributed differently over the PMTs than typical backgrounds.

```
max_s1/total_s1 < 0.45
```
(4.2.3)

- **f90 cut**: a cut has been applied on f90 to avoid events triggered on S2 or tails of S2 from previous events. This cut somehow mimics the one based on the livetime. We chose to be more rought because we are not interested in the lower region of f90.

```
pulse[0].f90 > 0.1
```
(4.2.4)

The saturation cut, which is applied in the typical analysis, is not used here because almost all α events saturate the ADC for one or more channels.
After these general cuts, a second set of cuts is performed to isolate possible αs. In order to do so, we rely on the information inferred from figure 4.2.5: the population in which we are interested has high energy and high f90, represented in this plot by the population on the upper right of the image. It is noticeable that their distribution has a diagonal trend in the range $20{\cdot}10^3$ - $35{\cdot}10^3$ PE and that there are no high f90 events after $\sim 35{\cdot}10^3$ PE. This features is due to the ADC saturation.

- **f90 alpha cut**: the identification of α particles relies on this cut on f90, because α produce a S1 with a different f90 than electron recoils. Figure 4.2.5 shows the f90 parameter versus S1.

```
pulse[0].F90 > 0.4
```
(4.2.5)

- **S1 integral cut**: at low S1, the distinction in f90 between the alpha and electron recoil populations is not as clear, so a cut on the S1 integral was applied to the events. In order to pass this selection, the S1 integral must be greater than 2000 PE.

```
pulses[0].param.fixed_int1 > 2000
```
(4.2.6)

Once we selected α candidates with the f90 and S1-based cuts described above, we further refine our sample by classifying the events according to the breakdown

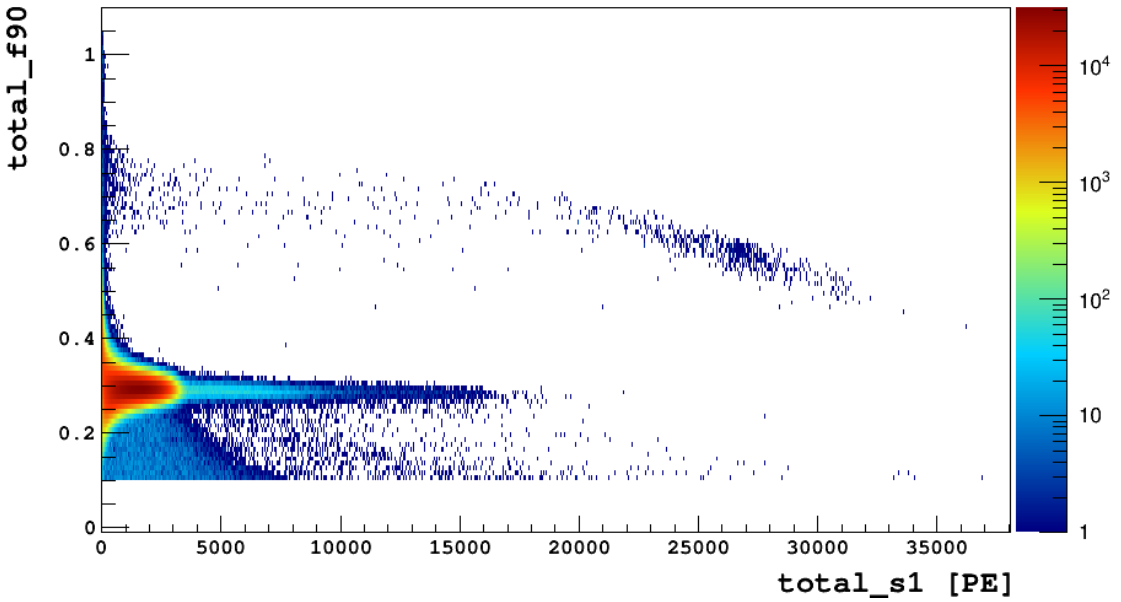

Figure 4.2.5: *f90 parameter versus S1 integral. We observe two distinct populations: the lower band (at f90* ≈ 0.3*) is due to electron recoils, while the higher band (f90* ≈ 0.7*) is dominated at high energy by* α*. The total entries of this histogram are 27 million events.*

summarized in table 4.2.1.

The first category includes events with an S1 and S2 pulses, shown as red dots in figure 4.2.6. The second category contains events which drift time is greater than 366μs and therefore on the cathode, shown as blue dots in figure 4.2.6. In the third category fall all the other kinds of events: events with four pulses, or only one pulse, shown as green dots in figure 4.2.6. Figure 4.2.6 shows the selected events in a f90 versus S1 integral plot. The majority of the events are situated in the region of energy between 20000 and 35000 PE, which ordinarily we would read as approximately 3 to 7 MeV. However, these α saturate the digitizer, so the true amount of energy is unknown and in general higher than measured.

The same events displayed in figure 4.2.6 are plotted also in figure 4.2.7, which shows the ratio of the integral of the second pulse (which for the red points is S2) over S1, plotted against S1. Most red points show an S2/S1 ratio of order of 1, as expected for α events.

Type	S2	S2 on cathode	others
# of pulses	2 pulses	2 pulses	1 or ≥ 4 pulses
Drift time cut	drift time $< 366\mu$s	drift time $> 366\mu$s	N/A
S2 peak amplitude	or S2 peak > 10	or S2 peak > 10	N/A
# of entries	238 entries	252 entries	289 entries

Table 4.2.1: *Classification of α candidates into categories, according to the number of pulses.*

In conclusion, α background is not as trivial as was assessed at the beginning of this section. This study about α background will be extremely useful when, in the next two sections, other original analyses will be presented.

4.3 Delayed Coincidence Method: ^{222}Rn Activity

Within the radioactive contaminants, ^{222}Rn , daughter of ^{238}U , deserve particular attention because it is present in gaseous form in the underground laboratory at LNGS and, in spite of the many precautions taken, it can diffuse from the surface of detector components (such as PMTs) into the LAr. Because of ADC saturation, which affects high energy decays, the evaluation of ^{222}Rn activity cannot be done using the energy spectrum but it has to be done using some other methods.
One of the ^{222}Rn daughters is ^{214}Po (see figure 4.2.4). ^{214}Po decays into ^{210}Pb with a mean-life of 164.3 μs, and therefore ^{214}Bi-Po decays can be identified via a delayed coincidence method. ^{222}Rn reaches secular equilibrium with ^{214}Bi in approximately 30 minutes, which means that the rate of ^{214}Bi-Po events gives a good estimate of the ^{222}Rn contamination in a given volume. Delayed coincidences are indeed a powerful tool with which to identify specific background sources from natural and artificial radioactivity. In this analysis, the delayed coincidence method to assess the contamination from ^{222}Rn and its daughters has been successfully applied and will be here described in all its steps.
A delayed coincidence search consists in looking for two consecutive decays, the second of which needs to have a mean-life τ which is shorter than the acquisition window ($\tau \ll 560\mu$s): in this case, both decays in the coincidence will be observed in the same event.

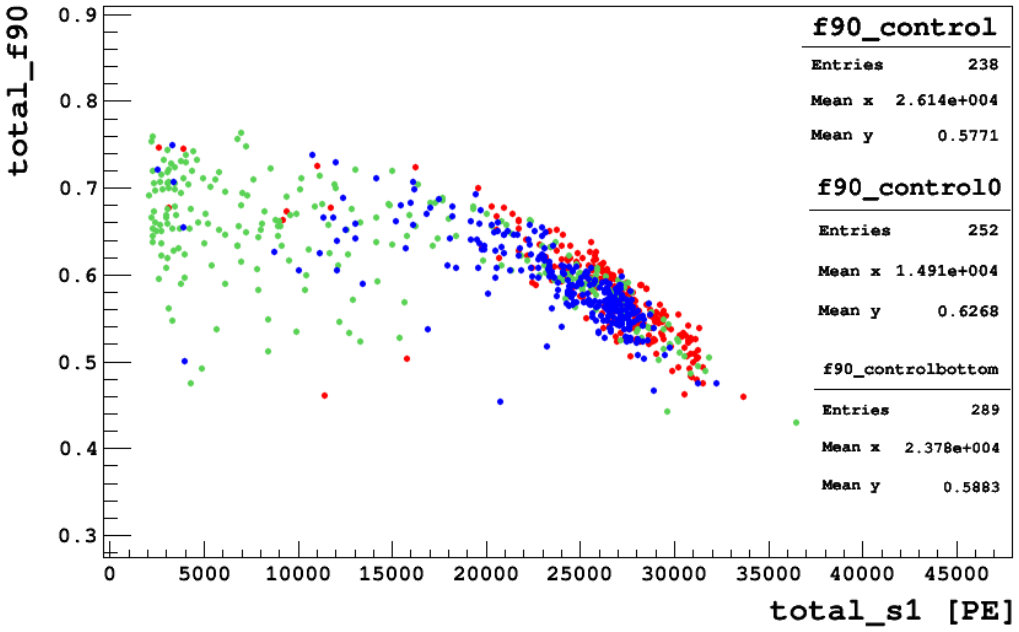

Figure 4.2.6: *F90 parameter for α candidates as a function of the S1 integral in PE.*

This analysis method provides a very clear signature for the presence of two isotopes in coincidence. This study has been attempted on both ^{214}Bi-Po and ^{85}Kr as described in table 4.3.1. However, several factors make the search for ^{85}Kr too difficult in this case:

- The pulse finding algorithm cannot presently identify separate pulses less than 2.5 μs apart, while the mean-life for ^{85}Kr is $\tau = 1.46$ μs.
- The two energy deposits do not happen in the same location because the ^{85m}Rb nucleus will not move before decaying to ^{85}Rb, however the γ from ^{85m}Rb is likely to travel a significant path before interacting with Argon. This removes

Nuclide	Decay Mode	$Q_0[MeV]$	$Q_0[MeV]$	Mean-life [μs]	BR
^{214}Bi-Po	$(\beta+\gamma) \rightarrow \alpha$	3.20	7.69	236	100%
^{85}Kr	$\beta \rightarrow \gamma$	0.17	0.51	1.46	0.43%

Table 4.3.1: *Main features of the isotopes for which we attempted a delayed coincidence analysis.*

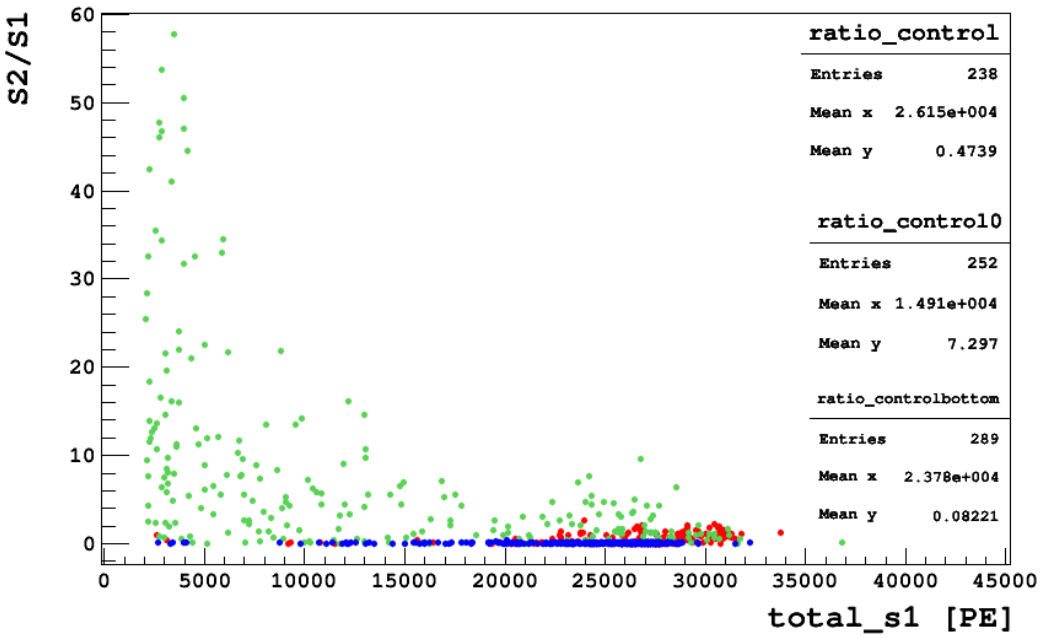

Figure 4.2.7: *S2/S1 ratio for α candidates as a function of the S1 integral in PE. For blue and green events, "S2 integral" refers to the integral of the second pulse.*

the possibility of using a powerful same-z cut.

- The β-γ decay has a very small branching ratio for ^{85}Kr (0.43%), and therefore produces an extremely low rate, which in our case is completely overwhelmed by the rate of accidental coincidences in AAr.

4.3.1 ^{214}Bi-Po Cuts

^{214}Bi-Po decays are fairly easy to identify because the ^{214}Po decays by emitting an α particle, and α decays have a distinctive signature in Ar. In the α background section the peculiar characteristics of α particles have been widely described and now this information will be put into practice. Additionally, since the α does not travel any significant distance before interacting with Argon, it is possible to perform a cut on the z position (or equivalently on the drift time difference) for the two decays in the coincidence.
The cuts applied to identify ^{214}Bi-Po candidates are listed below and summarized

in Table 4.3.2.

- **Number of pulses**: only events with at least three pulses will be accepted at this time. Indeed, in order to select ^{214}Bi-Po candidates, events with two S1s and one or more S2 pulses are selected. The freedom on the number of S2 pulses comes from the expectation of seeing a pulse from the ^{214}Bi decay and one from the ^{214}Po decay, but the S2 from the ^{214}Po decay may come too late to appear in the 500 μs window. On the other hand, it is possible to have more than two S2s when the pulse finder identifies both β and γ from the ^{214}Bi decay. Thus, a lower limit to the number of pulses can be set, but not an upper limit.

  ```
  event.sumchannel.pulses.size() > 2
  ```
  (4.3.1)

- **f90 Cut**: the cut on f90, performed on the first pulse, is once again crucial to remove events which trigger on S2 or on the tail of S2.

  ```
  event.pulses[0].param.f90 > 0.1
  ```
  (4.3.2)

  When applied to subsequent pulses, this parameter is also used to distinguish S1-like pulses from S2-like pulses.

General Cuts		
# of pulses > 2	f90 first pulse > 0.1	Found Baseline in Sum Channel true

^{214}Bi-Po Cuts			
# of S1 pulses > 2	# of S2 pulses ≥ 1	Second S1 f90>0.4 and S1>1000 PE	Cut in z <5 μs

Table 4.3.2: *Cuts applied to all events to identify ^{214}Bi-Po candidates.*

For the analyzed data, about 30% of the events overcoming the basic quality cuts survive this general set of cuts. For the remaining events, each pulse is tagged as an S1 or S2 with the following rules:

- **S1 tag**: pulses are tagged as S1 if f90 > 0.1 and the S1 amplitude is at least 5 counts.

```
pulses.param.f90 > 0.1
sumchannel.pulses.peak_amplitude > 5
```

- **S2 tag**: S2 pulses are pulses with f90 < 0.1, amplitude > 3 counts and total integral > 2000 PE, so that the small pulses or tails of S2, that are considered by the pulse finder as separate pulses, will be discarded.

```
pulses.f90 < 0.1
sumchannel.pulses.peak_amplitude > 3
pulses.npe > 2000
```

A final selection is performed to identify ^{214}Bi-Po candidates:

- **Possible ^{214}Bi-Po event**: this cut selects only events in which the second S1 is α-like, as described in Section 4.2.2. For all the data analyzed, 190 events survived the cuts.

- **Same-z ^{214}Bi-Po event**: for events with two S2 pulses, we can compare the drift time of the two decays, and make a same-z position cut by requiring that the drift times be less than 5 μs different. In this case also the S2/S1 ratio was checked requiring it to be less than 10. This cut found 6 events.

It is important to notice that the **Possible ^{214}Bi-Po events** category includes events with only one S2, for which it is impossible to evaluate the z position of both decays; events with four pulses, for which it is immediate to compare both position and S2/S1 ratio; and finally events containing more than 2 S2 pulses because of multiple scattering or random coincidences. In this last case a further step is needed: the S2s were paired trying different combinations and it is checked if their distances were compatible with those of their S1s. This permitted to find two of the 6 **Same-z ^{214}Bi-Po events**.

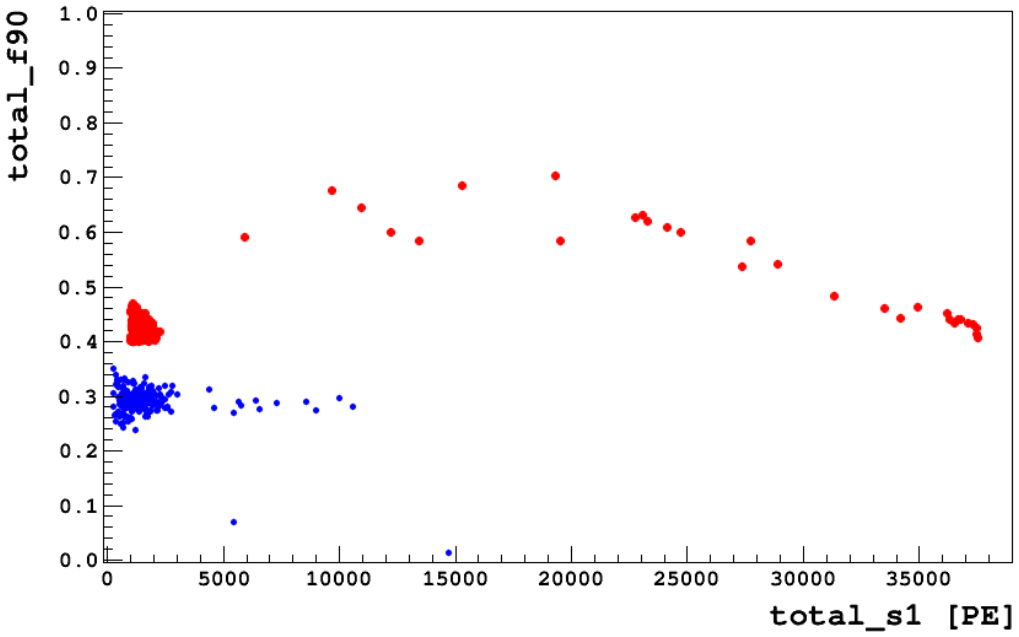

Figure 4.3.1: *The f90 parameter as a function of the the S1 integral, for the 190 events classified as possible ^{214}Bi-Po candidates, meaning that they already passed all the cuts with the exception for the same-z cut. Here are displayed both S1 pulses in each event: blue dots show the β decay and red dots show the α decay.*

4.3.2 ^{214}Bi-Po candidates

Out of the 30% of events that pass the general cuts, 190 fulfill all the requirements to be identified as ^{214}Bi-Po candidates. Figure 4.3.1 shows the f90 parameter as a function of the S1 integral for the 190 ^{214}Bi-Po candidates. Of these, 6 were immediately recognized as ^{214}Bi-Po from the analysis macro, while for the other events it was necessary make some assumptions about the energy of the first S1 and to scan the waveform visually.

The events not identified automatically have more or less that four pulses, so it is necessary to first look for an α-like S1 anywhere after the trigger time. Then, the five waveforms can be examined, seeking for two S2 pulses, when it is possible, with the same drift time difference as the two S1 pulses. If both conditions are true, it means that the two decays are a $\beta \rightarrow \alpha$ pair, happening at the same z, and thus the event is likely to be a ^{214}Bi-Po . About the energy of the first S1, it is assumed that

its spectrum is all above the ^{39}Ar end-point. While scanning the remaining waveforms, 7 more ^{214}Bi-Po candidate were found, while the other waveforms contained probably accidental coincidences with α events.
Three waveforms for the ^{214}Bi-Po events identified in this analysis are shown in figure 4.3.2. Of the 13 final ^{214}Bi-Po candidates, one was reconstructed on the cathode, while for the other 12 further investigation is needed. For this first approximate estimation the position of the remaining 12 ^{214}Bi-Po events was supposed to be in the bulk of the detector.

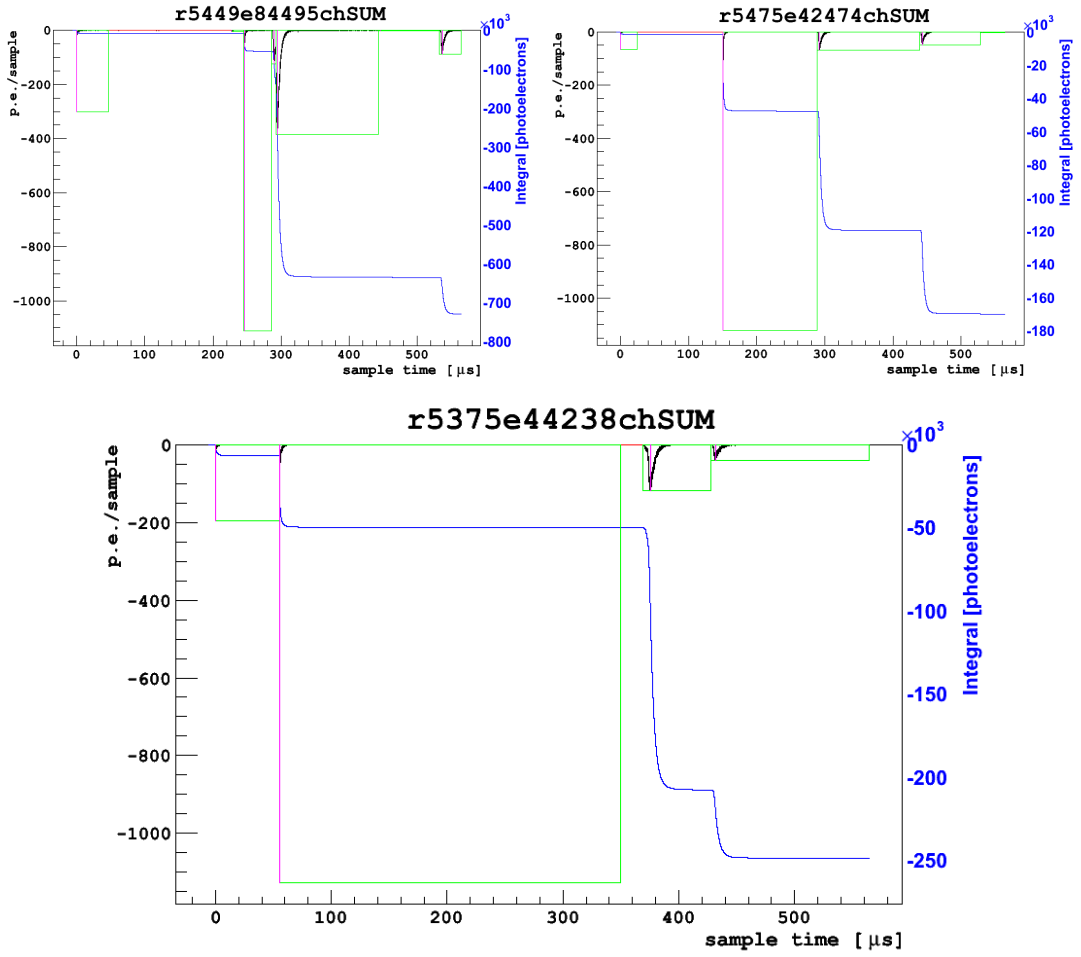

Figure 4.3.2: *Waveforms of ^{214}Bi-Po candidates found in the bulk of the detector (top) and on the cathode (bottom).*

4.3.3 The ^{222}Rn Contamination

An upper limit to the ^{222}Rn contamination in Argon can be computed from the number of ^{214}Bi-Po candidates. This is however only a first estimate: for a final value of the ^{222}Rn activity further investigation is needed. In particular, to obtain a more accurate value, the efficiencies with which ^{214}Bi-Po events are identified must be calculated.
For this calculation, the event detected on the cathode has been excluded because it is situated outside the fiducial volume (1 cm from the cathode). This fiducial volume was chosen because the efficiency for detecting ^{214}Bi-Po coincidences on the cathode cannot be accurately determined at the present moment. However, the addition of one event and the relative increase in fiducial volume does not change the upper limit on ^{222}Rn activity by more than 8%.
An upper limit to the ^{222}Rn activity in Argon can be computed by performing the following steps:

- given the small statistics on the ^{214}Bi-Po sample, we will compute the upper limit at the 90% C.L. via Poisson statistics. With an observation of 12 events, the 90% C.L. upper limit is 16.6 events.
- corrections are made by considering that only 90.7% of ^{214}Po decays occur within the data taking window. This efficiency correction raises the upper limit on the number of events to 18.3.
- the number of events are divided by the 6.3 days of livetime, obtaining an upper limit to the total activity of 33.6 μBq.
- finally, the total activity is divided by the 45.7 kg of fiducial volume.

After all the above calculations, the upper limit for ^{222}Rn activity yields 0.74 μBq/kg at 90% C.L.: this can be compared with results from other experiments such as Xenon100, LUX and DEAP-1, which all quoted a ^{222}Rn activity in the tens of μBq/kg.

4.4 From the Data to the Exclusion Plot

If one supposes that DM exists, that it takes the form of WIMPs and that its cross section does not depend on the spin, then one presumes for the galaxy a standard halo model with the parameters given in table 4.4.1, the main two elements that remain unknown are WIMPs cross section and WIMPs mass. These two quantities are not independent but they are strictly related as appears in equations 2.2.4 and 2.2.10 of the second chapter.
A wide range of direct detection DM experiments have scanned the parameter space (σ_n, M_W) starting from high values of the WIMP-nucleon cross section. Some of them saw signs of DM and marked the areas at issue; some other experiments instead have only negative results hence they can set a line that delimits the region already explored.
Once a region has been surveyed by more than one experiment, using different techniques for a long exposure time, there is little interest in continuing to look at the same area. Therefore, the aim of every new experiment is to explore new regions by increasing in sensitivity and lowering that line in this way. The list of factors that contribute more or less to this progress is not very long and the effort invested in the various collaborations to gain territory in the parameter space is incommensurate compared to the award. Nevertheless, this seems to be the direction to undertake. The factors, on which new experiments can play, are:

- target material, through the form factor that depends on the size and therefore on the atomic mass of the nucleus;
- energy resolution of the detector, through the light yield and the quenching factor, measured during neutron calibration;
- efficiency of detecting the nuclear recoil, obtained from acquired data and neutron calibration and strongly dependent on the capability of the PSD to reject electron recoil background;
- minimum and maximum detected energies, also fixed by the efficiency;
- exposure, given by the exposure time and the total target mass.

Whereas in the previous sections the reconstruction and analysis of the data were discussed in detail, here in this section, the main steps to obtain from those data a

projection sensitivity will be presented. The factors listed above will be described and their numerical values will be given from the results that DarkSide-50 obtained so far. Notice that since DarkSide-50 has not had a neutron calibration yet, some of the information needed is provided by the SCENE experiment [39].

4.4.1 Parameters of the Standard Galactic Halo

Once the target material, its active volume (or its total mass) and the exposure time are specified and once few parameters from independent measurements are given, it is indeed possible to draw a first projection of the sensitivity plot in the parameter space (σ_n, M_W). The parameters needed are: ρ_0, the local density of DM; v_0, the average speed of WIMPs; v_{esc}, the escape velocity of the galaxy; v_E, the orbital speed of the Earth about the galactic center; and v_{min}, the minimum velocity that a WIMP needs to cause a nuclear recoil. The parameters enumerated are summarized in table 4.4.1.

The local DM density is determined by galaxy rotation curves and even if it is still being debated, the community has adopted a value of ρ_0 =0.3 GeV cm^{-3} [20]. The galactic escape velocity v_{esc} is estimated around 544 km s^{-1} [44], though it can reach an upper limit of about 600 km s^{-1} if one considers an uncertainty of 9%. About the local rotation velocity, the discussion on its value is still open: recent measurements claim a value of approximately 250 km s^{-1} while many earlier measurements indicated a lower velocity of about 220 km s^{-1}; here, in this thesis the value given by reference [20] of 230 km s^{-1} will be adopted

The parameter v_E varies throughout the year with an annual modulation of ∼7% and a maximal velocity approximately at June 2nd. However, investigations on the annual modulation of WIMPs rate is not the object of this work nor of the DarkSide-

Parameter	Definition	Value	Uncertainty	Ref.
ρ_0	local DM density	0.3 GeV cm^{-3}	∼factor 2	[20]
v_{esc}	galactic escape velocity	544 km s^{-1}	∼9%	[44]
v_0	dispersion velocity of DM	230 km s^{-1}	∼10%	[20]
v_E	average Earth speed	263 km s^{-1}	∼10%	[45]

Table 4.4.1: *Galactic halo and velocity parameters needed to determine the expected WIMP-induced nuclear recoil spectrum.*

50 experiment, hence, for the Earth speed, an average value of 263 km s^{-1} will be adopted. The only parameter left is the minimum velocity of the incident WIMP necessary to produce a recoil of energy E_R: in case of forward scattering of the nucleus, cosθ =1 in equation 2.2.11 and therefore v_{min} is given by

$$v_{min} = \sqrt{\frac{M_t E_R}{2\mu^2}} \tag{4.4.1}$$

4.4.2 Null Experiment

Given the velocity distribution by equation 2.2.7 and the cross section by equation 2.2.4 we can now rewrite equation 2.2.1, that indicates the number of nuclear recoils due to WIMPs interaction, in its explicit form:

$$N_{rec} = M_t T \frac{N_0}{A} \frac{\rho_0}{M_W} \sigma_n A^2 |F(q)|^2 \frac{\mu^2}{\mu_n^2} \int_{v_{min}}^{\infty} \frac{f_D(v)}{v} dv \tag{4.4.2}$$

Up to now numerous experiments, besides DarkSide-50, have searched for DM signal, but all of their results, apart for DAMA, are consistent with a no WIMP signal. However, having a null number of observed events does not imply that there are no nuclear recoils due to WIMPs interactions. In fact for DarkSide-50 we use the Poisson statistics to exclude parameter space as follows: the parameters that predict an average value μ in a single bin are excluded at a level of 1-α if the probability of seeing as few as observed is less then α. In particular, for zero observed events the correspondent upper limit on the mean μ is 2.3 events at a 90% exclusion level.
The number of events to which the expression of N_{rec} is comparable, is obtained thanks to the Poisson statistics. Consequently, the WIMP-nucleon cross section can be written as a function of all the other parameters. Nevertheless, there are still two factors that have to be calculated: the form factor $|F(q)|^2$ and the inverse average speed.

Form Factor

The form factor is due to the finite size of the target nucleus. Thus, to obtain the form factor, the amplitude $f_i(\vec{p}, \vec{p}')$ of the wavefunction for a WIMP scattering off a given nucleon i should be considered ($\vec{q} = \vec{p}' - \vec{p}$ is the momentum transfered to

the nucleus). Then, the total amplitude for scattering from all nucleons adds up together as follows:

$$F(\vec{p},\vec{p}') = \sum_{i=1}^{A} f_i(\vec{p},\vec{p}')e^{i\vec{q}\cdot\vec{r}_i} \tag{4.4.3}$$

where the exponential is the associated phase factor. Accordingly, one can obtain from equation 4.4.3 the total square scattering amplitude, since the cross section depends on it.

$$|F(\vec{p},\vec{p}')|^2 = \sum_{i=1}^{A} |f_i(\vec{p},\vec{p}')|^2 + \sum_{i,j\neq i}^{A} f_i(\vec{p},\vec{p}')f_j^*(\vec{p},\vec{p}')e^{i\vec{q}\cdot(\vec{r}_i-\vec{r}_j)} \tag{4.4.4}$$

Making the assumption that the momentum transfer is small, then the phase factor reduce to unity and the scattering amplitude can add coherently. This condition holds on well up to recoils energies of about 50 keV; but above it, the difference in the phase factors become more significant: in this case the gradual effect of loss of coherence can be modeled using the Helm parametrization [46]

$$F(q) = 3\,\frac{j_1(qr_n)}{qr_n}\,e^{-q^2s^2/2} = 3\,\frac{sin(qr_n) - qr_ncos(qr_n)}{(qr_n)^3}\,e^{-q^2s^2/2} \tag{4.4.5}$$

where j_1 is a spherical Bessel function of the first kind, s is the nuclear skin thickness, typically ~ 0.9 fm, and r_n is the nuclear radius that for Ar is $r_n = 1.29A^{1/3}$ fm $\simeq$ 4.40 fm.

In figure 4.4.1, the form factor as a function of the recoil energy is shown for three different target materials: Argon, Xenon and Germanium. From this plot it is clear why it is mandatory, for experiments using heavy nuclei as target material, to have a low threshold: the high part of the spectrum is strongly depleted due to the form factor that decrease sharply with the recoil energy. Experiments using lighter nuclei instead, such as Argon, have a good sensitivity also at high energy because the curve of the form factor is less steep and therefore it is greater than zero for a wider energy range.

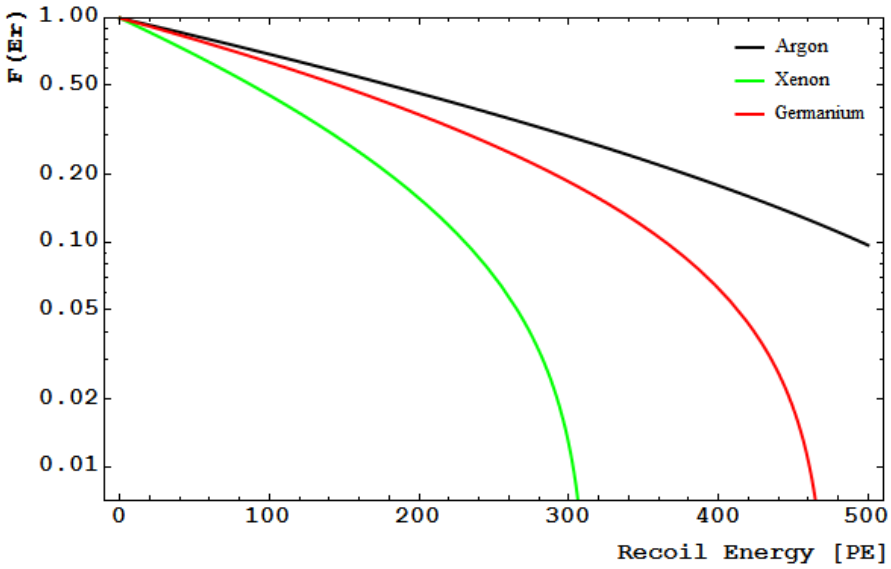

Figure 4.4.1: *Form factor as a function of the recoil energy for three different target materials: Argon, Xenon and Germanium. Note that the slopes are steeper for the last two elements.*

Inverse Velocity

The inverse velocity is easily obtainable by integrating the velocity distribution function (equation 2.2.7) divided by the velocity itself, between the minimum velocity and infinity. The resulting quantity is divided into three expression depending on the value of v_{min}

$$\int_{v_{min}}^{\infty} \frac{f_D(v)}{v} dv = \frac{\pi^{3/2} v_0^3 k}{2 v_E} \times$$
$$\begin{cases} \operatorname{erf}\left(\frac{v_E - v_{min}}{v_0}\right) + \operatorname{erf}\left(\frac{v_E + v_{min}}{v_0}\right) - \frac{4 v_E}{\sqrt{\pi} v_0} e^{-\frac{v_{esc}^2}{v_0^2}}, & v_{min} \leq v_{esc} - v_E \\ \operatorname{erf}\left(\frac{v_E - v_{min}}{v_0}\right) + \operatorname{erf}\left(\frac{v_{esc}}{v_0}\right) - \frac{2(v_E + v_{esc} - v_{min})}{\sqrt{\pi} v_0} e^{-\frac{v_{esc}^2}{v_0^2}}, & v_{esc} - v_E < v_{min} \leq v_{esc} + v_E \\ 0, & v_{min} > v_{esc} + v_E \end{cases} \tag{4.4.6}$$

4.4.3 Instrumental effects

During this dissertation the instrumental effects have been ignored. But DarkSide-50 is a real experiment and therefore the instrumental effects need to be considered in order to move from the observation of a given number of pure nuclear recoils in the Argon detector to an iso-rate curve on the WIMP mass-cross section space.
For example the resolution of the detector has to be accounted for. The resolution at the energies of interest is dominated by the statistical fluctuation in the number of photo electrons (PE) produced during the interaction. In this first estimate of the energy resolution of the detector, a Poisson distribution for the fluctuations in the number of PE corresponding to a fixed nuclear recoil energy has been assumed. Other parameters needed to evaluate the projected sensitivity are the PE threshold, the light yield and the f90 acceptance curves for nuclear recoils. Since DarkSide-50 did not have a neutron calibration yet, and the neutron background is fortunately very low, the last two parameters are extrapolated from SCENE [39], after a careful cross-calibration of the two detectors. The SCENE collaboration exposed a dual-phase LAr-TPC to a low energy pulsed narrow-band neutron beam, to study the scintillation light yield of recoiling nuclei. It is important to remark that the projected sensitivity obtained with these parameters from SCENE is preliminary because there are still effects and systematic uncertainties to be reviewed.
The TPC has a certain light yield that has been measured, for electron recoils, with dedicated calibration studies. The light yield is an important scintillator parameter that indicates the amount of collected light (in PE) per keV of recoil energy. In DarkSide-50 the calibration was performed using a source of ^{83m}Kr that was introduced into the system and that decays monocromatically with an half life of less then two hours and using the ^{39}Ar , naturally present in the AAr. For the energy scale measurement, the light yield obtained with the ^{39}Ar was chosen because it is more reliable[4] and the value of which is

$$LY = 8.040 \pm 0.006(\text{stat}) \pm 0.020(\text{sys}) \text{ PE keV}^{-1} \tag{4.4.7}$$

[4]Since the light collection efficiency of the detector varies with position, the light yield obtain from the uniformly distributed ^{39}Ar is more appropriate as a calibration for the expected uniform distribution of WIMP interactions.

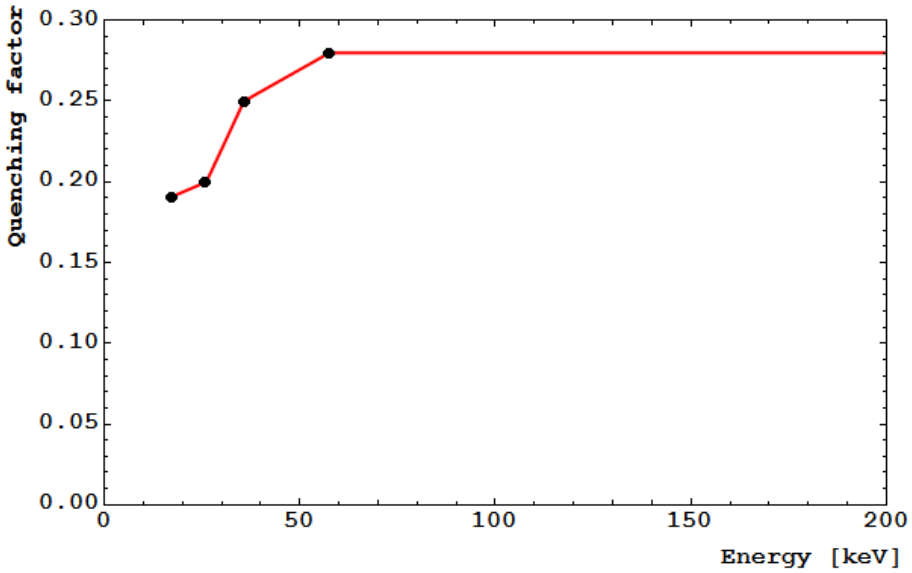

Figure 4.4.2: *Quenching values given by the SCENE experiment for five different recoil energy values.*

However, the scintillation yield for nuclear recoils differs from that of electron recoils. This is because nuclear recoils induce a diminished response in target materials, when compared to electron recoils of the same energy. In scintillators this is mainly due to the small fraction of recoil energy that is transferred to electron excitation while the rest is dissipated through nonradiative energy transfer: an energy-dependent quenching factor can be defined as the ratio of the light yield from a nuclear recoil to that from an electron recoil of the same energy. The quenching factor contributes to the decrease of sensitivity at low energies (see figure 4.4.2). For DarkSide-50, the amount of quenching for five different energy values was measured by SCENE. It is noticeable that the major effect of the quenching factor is at low energies, while for energies greater than 60 PE it is constant.

Another information coming from SCENE is the f90 values of nuclear recoils. Their distribution in the `total_f90` versus `total_s1` plot is similar to the distribution of electron recoils, but shifted upward with an average f90 value of 0.7. Furthermore, at low energies, both distributions are wider because of statistical fluctuations and, whereas the electron recoil band has an increase in the f90 average, the nuclear recoil band decreases: below a certain energy (set as the threshold) the electron recoil

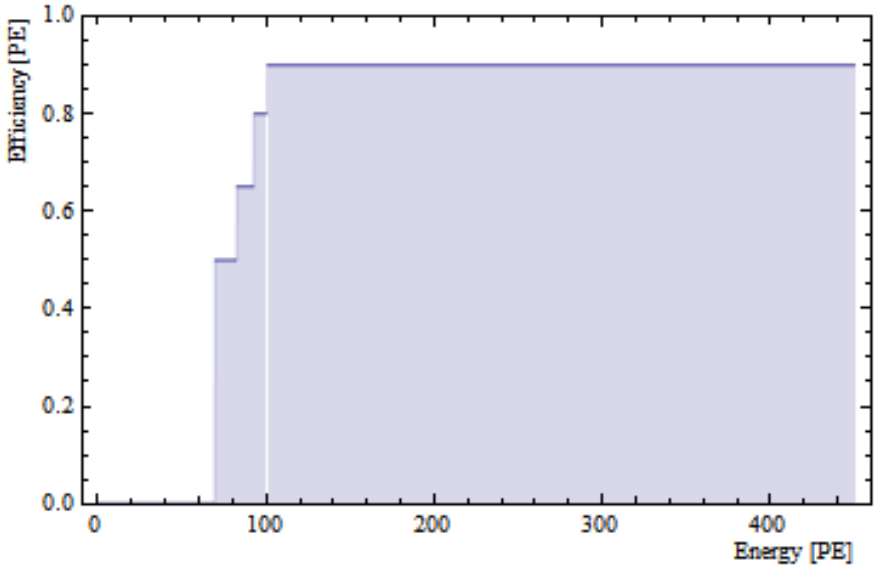

Figure 4.4.3: *Efficiencies given by the comparison of SCENE nuclear recoils data with the one coming from DarkSide.*

band start leaking into the nuclear recoil region and eventually the two distributions merge so that it is not possible to distinguish nuclear recoils from electron recoils. In order to obtain the efficiencies of detecting a WIMP-like event, reported in the plot of figure 4.4.3, the nuclear recoil acceptance curves from SCENE were superimposed to the DarkSide-50 event distribution in the f90 plot as a function of the S1 integral. The nuclear recoil acceptance curves, in gray in figure 4.4.4, follow respectively from top to bottom the 50%, 65%, 80% and 90% of the nuclear recoil distribution from SCENE. The last three curves from SCENE are conservative since they were calculated for data acquired at a much lower light yield than DarkSide-50, which leads to a much broader distribution. The efficiencies were extrapolated by comparing these two distributions so that for each energy bin they would not overlap. The dark blue isolated points in figure 4.4.4, in this way rejected, have a probability of about 1% of producing an actual event during the entire DarkSide-50 exposure and are considered outliers of the electron recoil distribution.
Finally, assuming that additional terms such as geometrical disuniformities are subdominant, the energy resolution is a function only of the quenching factor and varies with the square root of the energy, given by

$$\sigma_E(E_r) = \sqrt{E_r LYQ(E_r)} \tag{4.4.8}$$

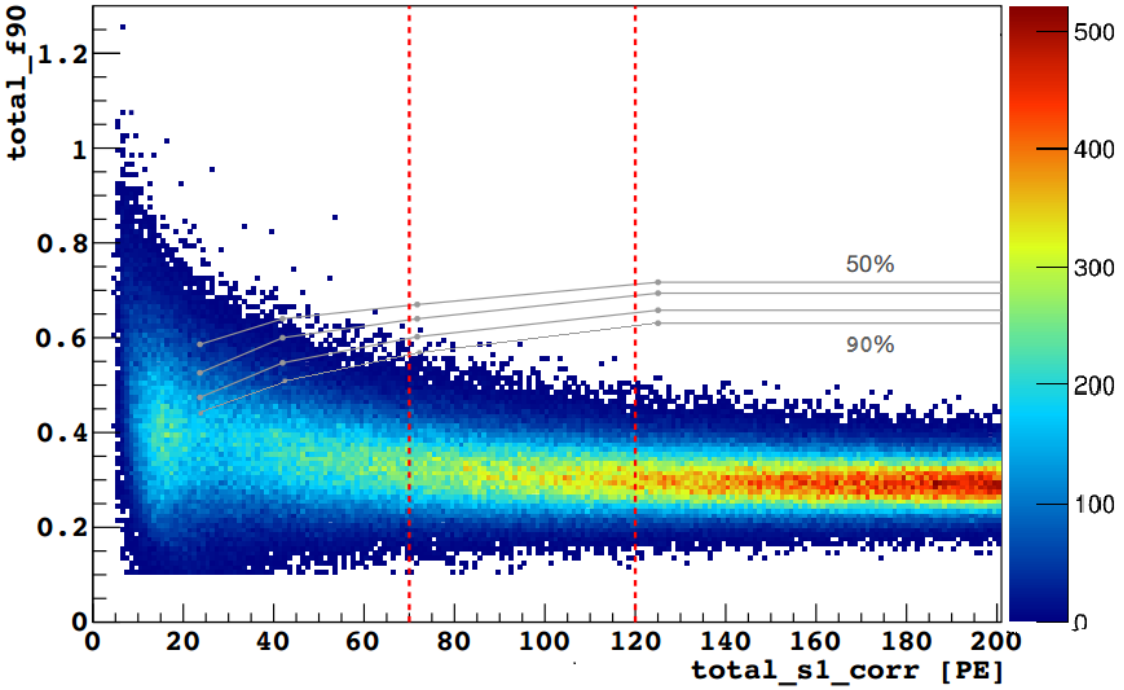

Figure 4.4.4: *Plot of the f90 versus the total S1 integral. In this same plot are marked out in gray the nuclear recoil acceptance curves from SCENE. From top to bottom are reported 50%, 65%, 80% and 90% acceptances. From the comparison of these two data sets both efficiencies and energy thresholds can be inferred. The red dotted line on the left indicates indeed the energy thresholds chosen for DarkSide-50: below this line there are outliers events leaking out of the electron recoil band into the WIMP, or nuclear recoil, region.*

Lastly, gathering all the steps done in this section, we get the expression of the WIMP-nucleon cross section for the DarkSide-50

$$\sigma_n = 2.3 \left(M_t T N_0 A \frac{\rho_0}{M_W} \frac{\mu^2}{\mu_n^2} \int_q \int_{E_r} \int_v \frac{f_D(v)}{v} \frac{|F(E_r)|^2 F(q)}{\sqrt{2\pi}\sigma_E(E_r)} e^{-\frac{(q-Q(E_r)LYE_r)^2}{2(\sigma_E(E_r))^2}} \right)^{-1} \tag{4.4.9}$$

where F(E_r) is the form factor, F(q) is the detection efficiency and where the integral in q is carried out between DarkSide-50 threshold energy of 70 PE (or equivalently

35 keV) and about 430 PE (200 keV); the integral on the recoil energy is done from 0 to 500 keV; and the integral on the velocity is performed from v_{min} to infinity. The comparison between simulated data and the acceptance curves show that there are no events occurring above the 50% acceptance curve starting from an S1 integral of 60 PE. Nevertheless, a value of 70 PE has been chosen instead for the energy threshold, in order to be conservative.
Finally the curve reported in figure 4.4.5 represent the projected sensitivity obtained assuming no events in the nuclear recoil acceptance region.

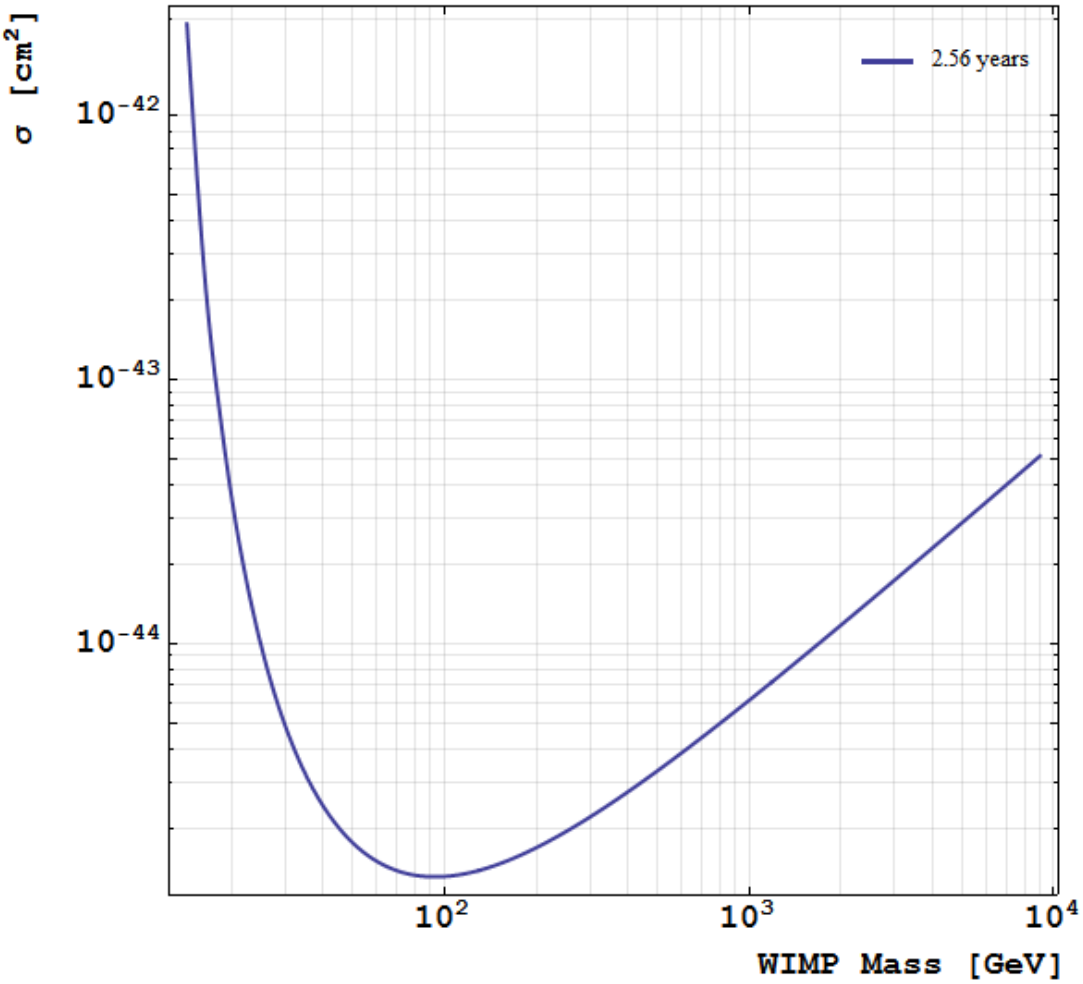

Figure 4.4.5: *Exclusion plot showing the projected limit obtained by DarkSide-50 in the parameter space σ-M_W, exposing 44.1 kg of LAr for a period of 2.56 years, collecting a total exposure of ∼113 kg×year.*

4.5 Feasibility Study of ^{39}Ar Spike

The wait for UAr opened a wide range of possible studies which aim to better understand the detector and to give a projection of the background rejection performance with almost the full statistics of DarkSide-50 (3 years).
One of the possible studies that came up following the "accumulation of statistics" trend is the ^{39}Ar spike. The purpose of the ^{39}Ar spike is to accumulate in a "short" time ("short meaning", for example, one month of data taking) a number of electron recoil events corresponding to the full statistics expected in DarkSide-G2 [48] exposure (18 tons×year). This is done in order to probe the PSD performance and check if with such high statistics the tails of f90 distribution for electron recoils would leak into the high f90 region (WIMPs region). A statistics that covers the full 5 years of exposure of DarkSide-G2 with UAr would also allow to calculate the projected sensitivity and set the possible limit that this experiment could reach in the DM search.
DarkSide-G2 is the second generation experiment still in the planning phase, designed to continue the DarkSide program on double-phase LAr-TPC. This will consists of a dual phase TPC filled with UAr for a total active mass of 3.8 tons which will have the sensitivity at the level of 2×10^{-47} cm^2 in a background-free run of 5 years.
It is obvious that the collaboration, before embarking itself on such an ambitious program, would like to have some valid way to verify the DarkSide-G2 sensitivity expectations. The ^{39}Ar spike could be the answer to this need.

4.5.1 Simulation with Real Data

In order to perform an ^{39}Ar spike it is necessary to add ^{39}Ar to the AAr already present inside the detector. There has to be enough ^{39}Ar so that the increase of the event rate will allow the accumulation of the needed statistics in the desired time. A high event rate will increment the total number of events acquired, but at the same time it will cause pile up. Pile up occurs when two or more interactions are temporally close, they appear in the same DAQ window of the second, causing the discard of both events. This happens because, in order to detect the full S2 scintillation, the DAQ window has to be at least 400 μs long.

The innovative solution that this study proposes is to take data with only S1 avoiding in this way the pile up problem. In fact, since the PSD involves only S1, it is possible to operate the TPC in the same conditions of normal runs, with a drift field of 200V/cm, but without an extraction field and hence no S2. This would allow for a much shorter DAQ window (for example 20 μs) and not having to worry about pile up or triggering on S2.
However, this shortcut has its consequences: the S2 signal, even if it is not exploited yet for S2/S1 background rejection, is still used by offline analysis. For example the drift time, on which all the fiducial cut and maximum fraction of light cut are based, is calculated with the S2 start time. Another complication can arise from the impossibility of identifying the number of pulses within the event. In the new TPC configuration, with no extraction field, all the events would have only one pulse and therefore it would be impossible to eliminate single pulses or multiple scattering events.
Among other purposes, in normal runs, all this information from S2 is used to reject events populating high f90 regions and interfering with the WIMP region of interest. In any case, there could be other methods to succeed in this task. Thus, before proceeding with the ^{39}Ar spike, the question that this analysis tries to answer is: will the absence of S2 in the ^{39}Ar spiked run preclude the possibility of rejecting events at high f90?
The sake of this analysis is to confirm or deny the feasibility of the ^{39}Ar spike with the S1-only data taking mode. In order to do so, data from 6.3 days of livetime have been analyzed pretending they did not have an S2 acquired and therefore without S2-based cuts. Information from S2 has been used only to cross check and tune the cuts. Only one cut deceives this rule and it is the one on the livetime designed to avoid triggers on S2. This cut is applied only because in a real ^{39}Ar spike there would be no S2 associated at each S1, hence this cut would be useless.
By applying only the basic cuts to events with one or two pulses what obtained is a "dirty" distribution of f90 as a function of S1 integral, shown in figure 4.5.1, with all kinds of events populating the high f90 region, even at high energies. The aim of this analysis is to "clean out" the region of interest in the f90 versus S1 integral plot obtaining a result similar to the one of the standard analysis presented in section 4.1.

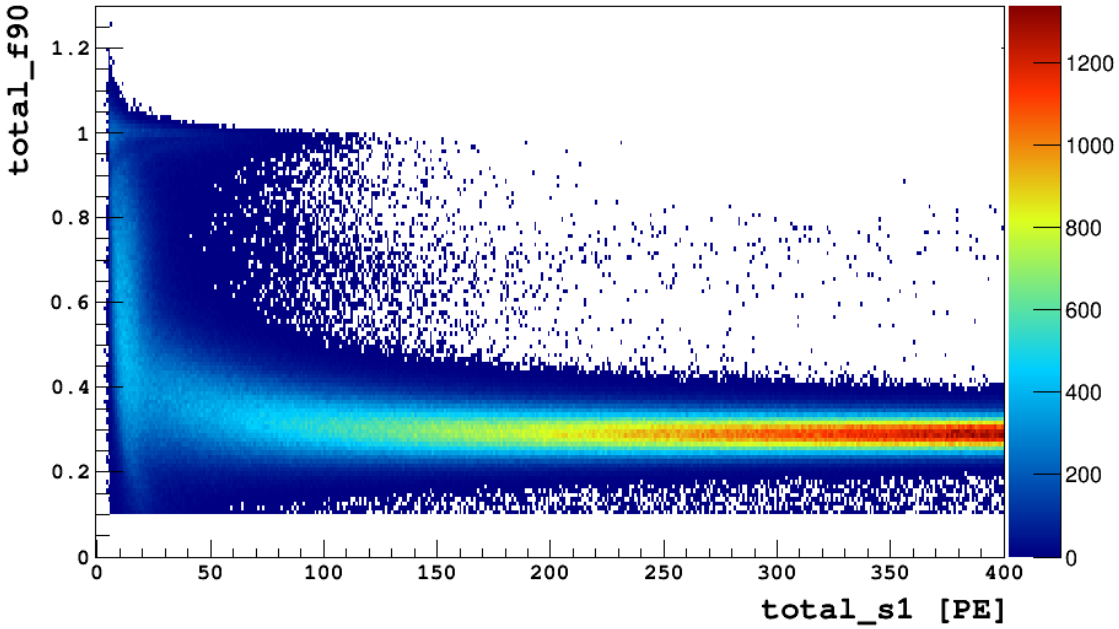

Figure 4.5.1: *F90 versus S1 integral of all the events with one or two pulses, passing the basic cuts. This plot contains approximately 25 million of events.*

4.5.2 S1 Only Analysis

The vast majority of events at high f90 of figure 4.5.1 are removed in standard analysis, by the request of having one S1 and one S2 and by the fiducial cut (1 cm from the cathode and 1 cm from the grid). Since this is not a standard analysis in order to eliminate those events it is first necessary to understand what they are and their origin, and second to find an alternative cut that will reject them.

Exploiting information about S2, events with one pulse only can be easly isolated. By plotting them in an f90 versus S1 integral distribution it is immediately clear that single pulse events are the most significant background source for this type of analysis. In figure 4.5.2 a distribution of single pulse events is presented. The most striking feature of this plot at high f90 is the presence of two distributions of unknown origin: the first one at f90∼1 that fades at approximately 150 PE; the second one at f90∼0.7, less sharp, but distributed up to the MeV scale.

Even though there is still a lot of uncertanty about the origin of these two bands of

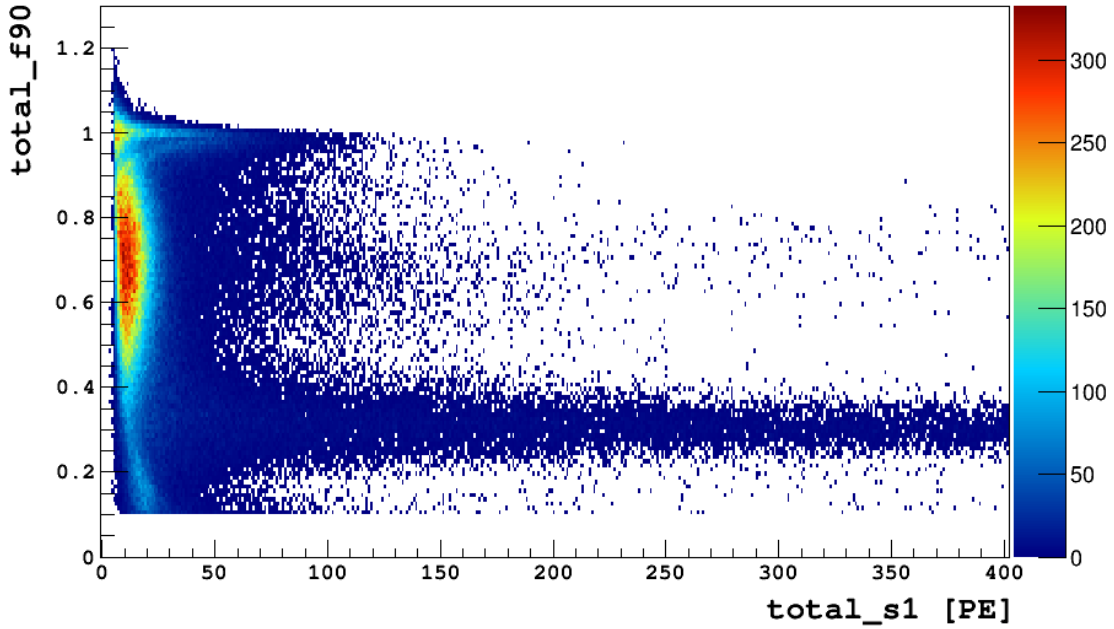

Figure 4.5.2: *F90 versus S1 integral displaying single pulse events only, passing the basic cuts. This plot contains about 275 thousand of single pulse events.*

single pulse events, it is possible to speculate on their nature, keeping in mind that these are all hypotheses. The two bands at very high and high f90 have been studied separately and in the rest of this section will be referred to as Cherenkov-like events (for f90∼1) and Alpha-like events (for f90∼0.7).

Cherenkov-like events

These events are too fast to be caused by scintillation. The rise time of the pulse is typically between 10 and 20 ns and they do not show a slow component. There are two possible explanations:

- they are pure Cherenkov events, in the quarz windows of PMTs or in the fused silica windows of the cathode and anode;
- they are due to light entering the TPC trough the optical fiber.

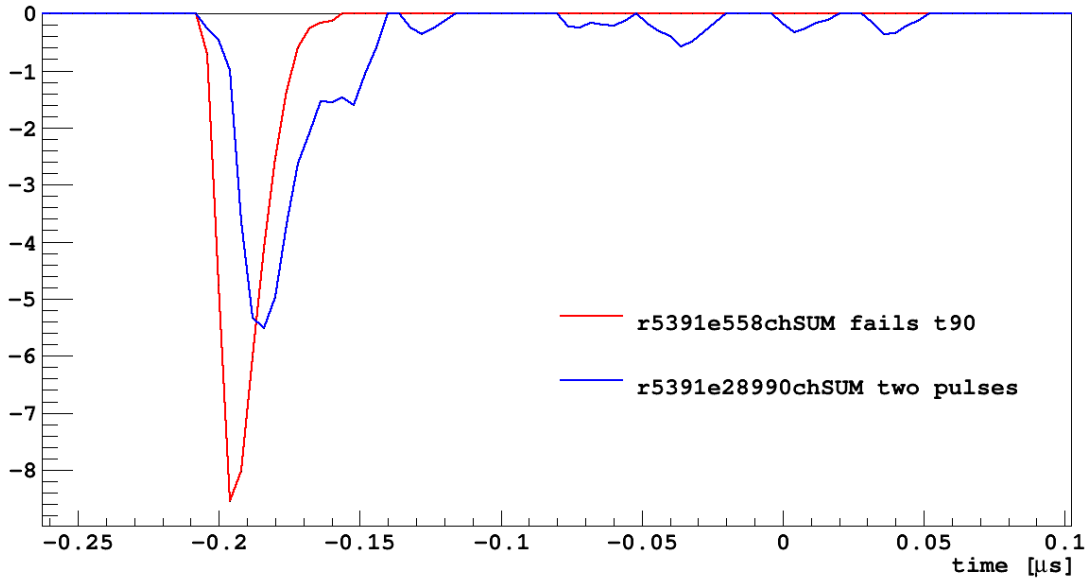

Figure 4.5.3: *Waveforms of two events with f90 above 0.9. In blue, an event with two pulses; in red, an event with only one pulse.*

In figure 4.5.3 a zoom-in of the waveforms of two events is reported. They both have an f90 above 0.9 and similar energies, but the one in blue has two pulses whereas the one in red only has one pulse (here only the first pulse is shown). It is noticeable that the red pulse does not have any slow component, leading to the idea that it is not a scintillation event.

These Cherenkov events would be very easy to reject requiring the existence of S2, but without this information and the events being very fast, a variable never used before can be appropriate for this case. This variable is the t90, defined as the time needed for each pulse to reach 90% of its total integral. In practice, as the f90, it indicates the speed of an event, but this time instead of having a fixed time window on which the integral is performed, it is the integral to be fixed and the time changes. The histogram on the left in figure 4.5.4 shows the t90 distribution of all initial events (one and two pulses) and of single pulse events (in blue). The red line at t90=0.1 μs marks the cut that has been applied. The cut has been set to this value because on the left of the red line almost all the events have only one pulse. This cut is a little risky because it cuts almost directly close to the WIMP region.

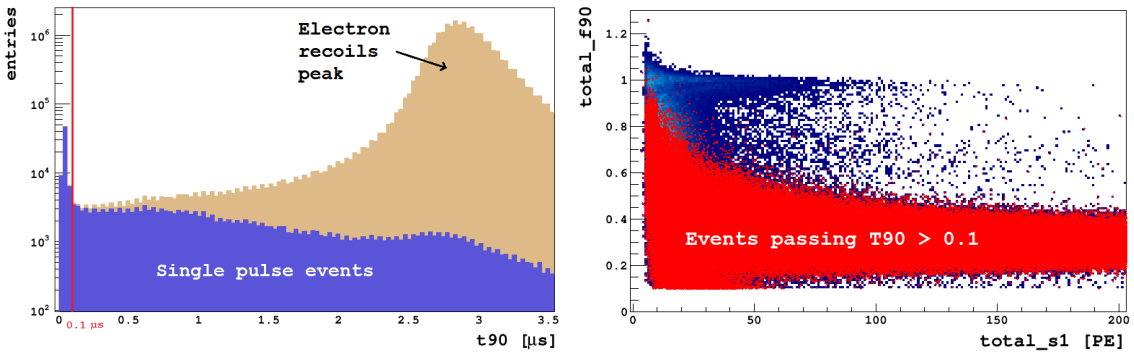

Figure 4.5.4: *On the left: distribution of t90 for events with one or two pulses (in brown) and for events with one pulse only (in blue). On the right: overlap of f90 versus S1 integral distribution before (in blue) and after (in red) the t90 cut.*

However, at low energies, the nuclear recoil band decreases in f90 and therefore this cut should not touch the region of interest. The plot on the right of figure 4.5.4 displays, in red, the events passing the t90 cut that seems to be effective on the Cherenkov-like events.

Alpha-like events

Fast single pulse events occupy the f90 band between 0.6 and 0.8 up to energies higher than 10000 PE as shown in figure 4.5.5.

Those events clearly belong to a different population than the one discussed before, but again their origin is not known. Among various conjectures, three hypotheses could satisfy the features of these pulses and therefore they could be a possible explanation for the presence of this population:

- alpha-like events without an associated S2 because the events are close enough to the surface that electrons from ionization are reabsorbed;
- Cherenkov+Compton events without an associated S2 because near the surface: the sum of a Cherenkov interaction in the fused silica window makes the f90 value of the subsequent Compton scattering in the Ar to increase;
- electron recoils near the lateral walls: part of the energy is released in LAr and part is absorbed by the TPB that has a fast scintillation (very close to the

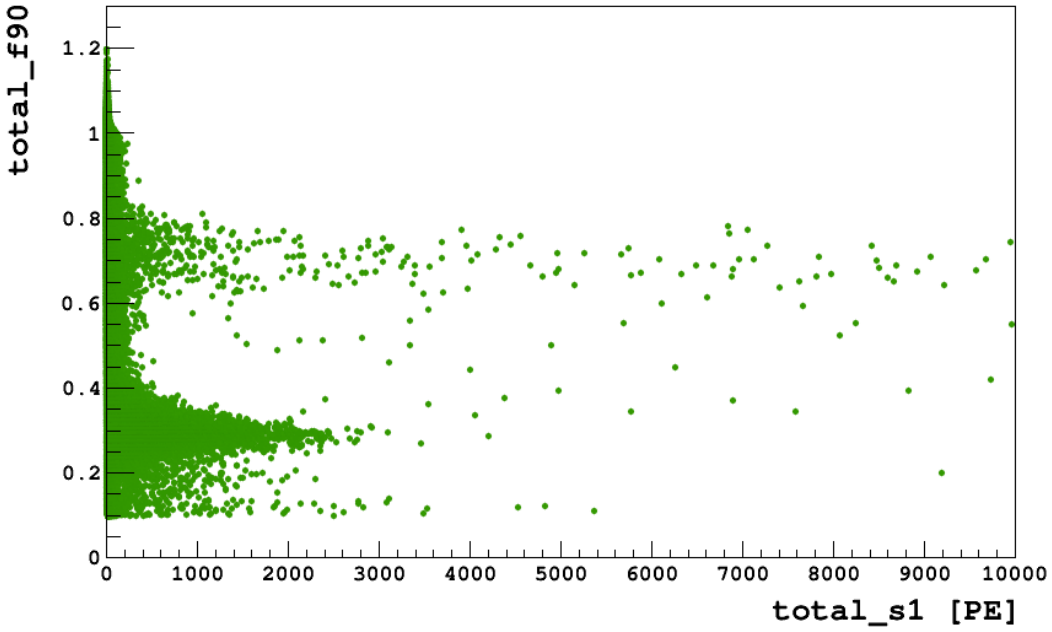

Figure 4.5.5: *Single pulse events in an energy range from 0 to 10000 PE. This plot contains about 275 thousand of single pulse events.*

neutron one [49]). The scintillation from TPB would increase the f90 value, shifting an event belonging to the electron recoil band up to f90∼0.7. Again the S2 is absorbed by the surface.

From the study of the waveform of these events with S1 only and f90 in the 0.6 - 0.8 range, it can be asserted that they seem regular scintillation events without S2. In figure 4.5.6 two waveforms in the time range of the first μs are displayed: in red is a typical single pulse event from the alpha-like population while in blue one of the few regular events with two pulses is shown and in the same f90-energy range, surviving the cuts. The similarity of these two waveforms is noticeable.

If the hypothesis of electron recoils near the surface together with TPB scintillation was the only origin for the alpha-like events, one would expect a spectrum related to the ^{39}Ar spectrum, but since this is not the case, those events are more likely to be degraded αs without an associated S2.

However, postponing to future studies the debate on where those events originate,

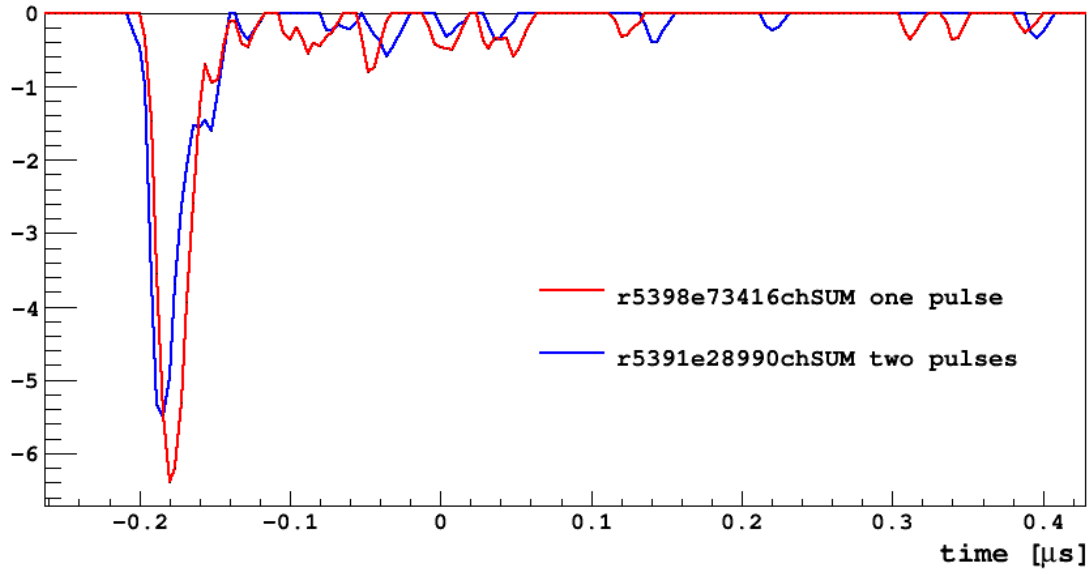

Figure 4.5.6: *Waveforms of two events with f90 in the 0.6 - 0.8 range. In blue, an event with two pulses; in red, an event with only one pulse.*

this analysis will focus now on how to reject them. There are two main techniques used to remove alpha-like events without any S2 information:

- maximum fraction of light to reject Cherenkov+Compton events;
- fiducialization along z-axis, useful for α cuts in the cathode.

In order to achieve a fiducialization without the drift time information, the top/bottom asymmetry of the detector can be exploited. Because of the gas pocket and the extraction grid, the top PMTs collect less light than the bottom ones giving origin, in this way, to a small asymmetry that can be used to define a new variable called `z_bis`

$$\texttt{z\_bis} = 30\ \texttt{log(max\_ratio + sum ratio)} \tag{4.5.1}$$

where `max_ratio` is the ratio of the light collected by the maximum top PMT over the bottom one; and `sum_ratio` is the ratio between the sum of S1 of all the top PMTs over the bottom ones. The factor `30` has been found empirically to maximize the `z_bis` range. In figure 4.5.7 the distribution of the new variable is presented as a function of the drift time for all the events passing the basic cuts. Here the

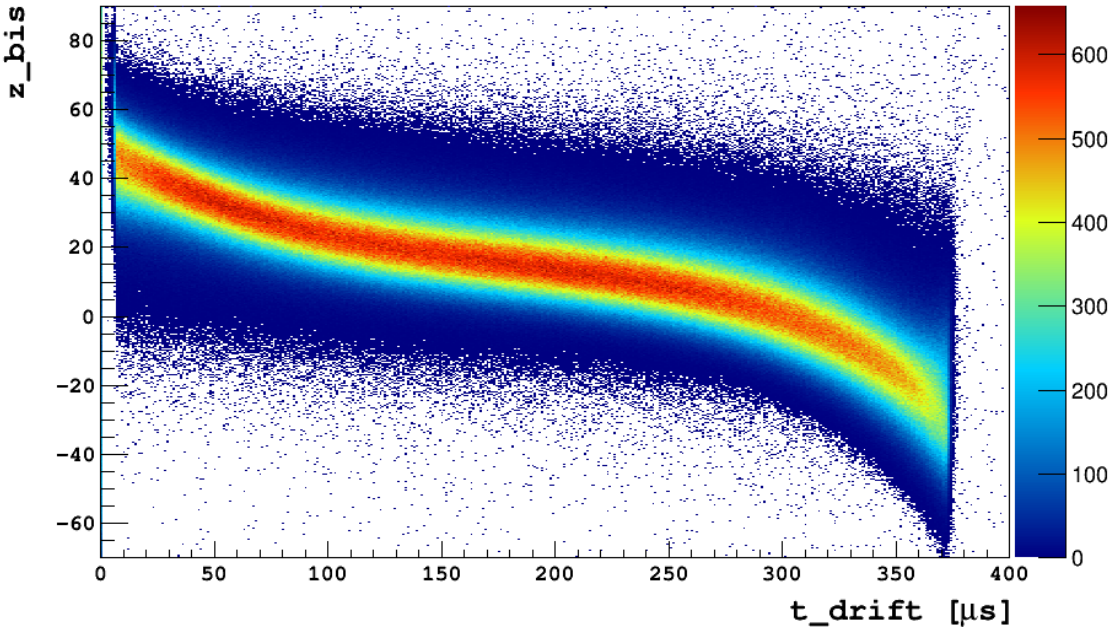

Figure 4.5.7: *Distribution of the variable as a function of the drift time.*

drift time has been used only to show the correlation between these two variables, especially at the top and the bottom of the TPC, and for a tuning of the cut. In fact, a cut in the `z_bis` variable roughly corresponds to a cut in drift time and, therefore, to a fiducialization along the x-axis. This fiducialization is not, however, very efficient because while some events from the bulk are removed, some others from the top and bottom of the TPC remain in the set of data that will be used for further analysis.

The other cut performed on the data is the maximum fraction of light cut, particularly useful to eliminate Cherenkov+Compton events having the Cherenkov on the PMT quartz or on the fused silica window. This cut is very similar to the one used by the standard analysis, described in section 4.1.3, but this time instead of the drift time the `max_s1/total_s1` versus `total_s1` distribution has been sliced for different `z_bis` values and on each of these slides the cut has been tuned.

Cut	Events 2 pulses passing	Events 1 pulse passing
Total events	24711944	275379
t90 > 0.1	96.6%	29.3%
`max_s1_frac`	96.6%	32.3%
-15 < `z_bis` < 35	80.7%	16.8%
All cuts	80.2%	16.5%

Table 4.5.1: *Summary of the cuts applied and their results on the events.*

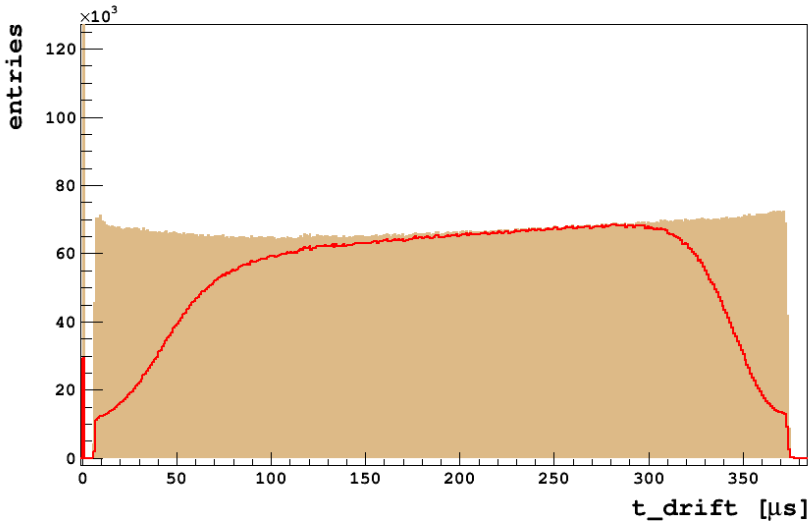

Figure 4.5.8: *In brown the distribution of the drift time before the cuts, showing about 25 million events. The red line represents the same distribution after all the cuts have been applied: the remaining events are less than 20 million.*

4.5.3 Results

All the cuts described above have been applied to the original set of data including both one and two pulses events. Table 4.5.1 summarizes all the non basic cuts and the percentages of events with one and two pulses passing each cut (the percentages are calculated on each cut separately, so some events are removed from more than one cut). The effect that the cuts had on the total events can be cross-checked on the drift time distribution, in order to visualize whether the fiducialization had the desired effect. Figure 4.5.8 shows the drift time histogram before (in brown) and after (red line) the cuts. From this histogram, it can be inferred that even though a

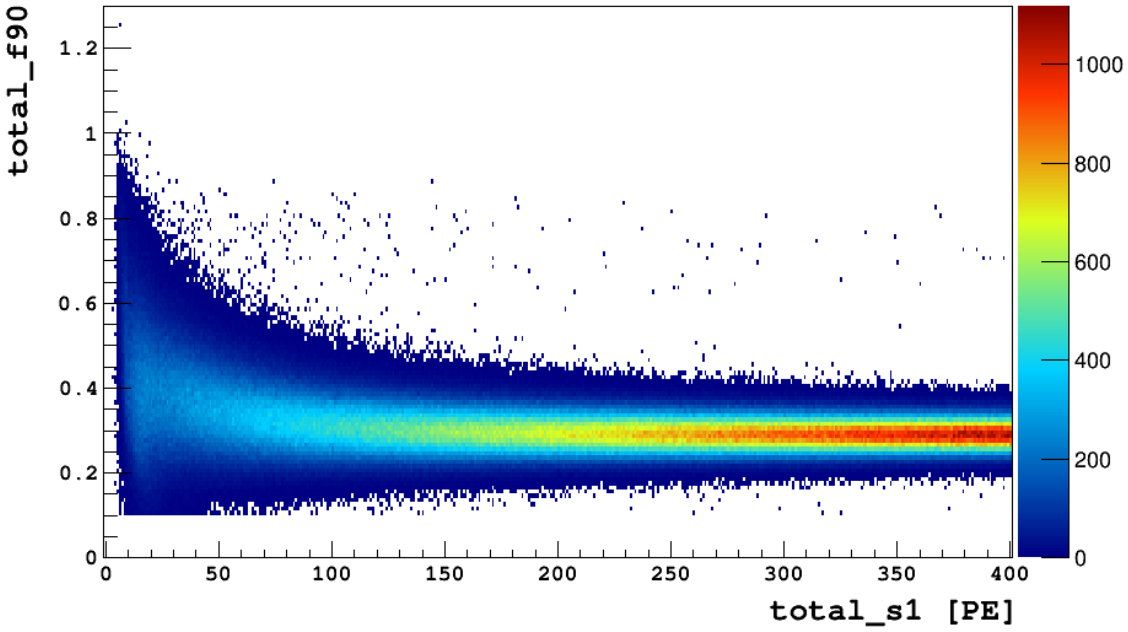

Figure 4.5.9: *F90 versus S1 integral of all the events with one or two pulses, passing all the cuts. The events surviving all the cuts are about 20 million, 5 million less than the initial ones.*

significant part of the single pulse events have been removed, there is still a part of this population that compromise the positive outcome of this analysis. Furthermore, the cut in `z_bis` and in `max_s1_frac` are not very efficient because they also remove events in the bulk of the detector that would usually be classified as good events. Nonetheless, the results from this analysis are incredible, considering that the starting point was figure 4.5.1 and that without any information about S2, the plot displayed in figure 4.5.9 has been obtained. The remaining background in the 0.6 - 0.8 f90 range is dominated by single pulse events (see figure 4.5.10) that cannot be rejected even when trying to do so with more selective cuts. They are probably due to degraded alpha near the lateral surface in the central regions of the TPC, so that top and bottom PMTs collect approximately the same amount of light.

In conclusion, this feasibility study on the ^{39}Ar spike demonstrated that it is not possible to collect the needed statistics for the full DarkSide-G2 exposure, by introducing ^{39}Ar in the detector and operate in an S1-only mode. Nevertheless, it still

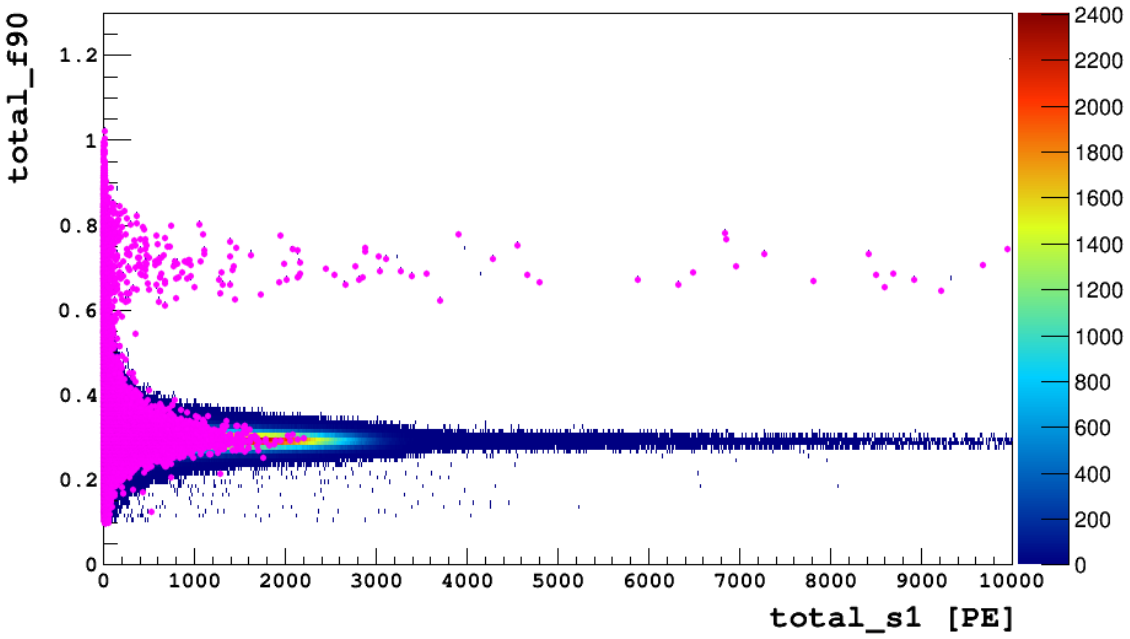

Figure 4.5.10: *F90 versus S1 integral of all the events with one or two pulses passing all the cuts, with superimposed in magenta, the same distribution but for single pulse events passing all the cuts. At all energies the background in the region of interest is dominated by single pulse events.*

leaves the possibility of an ^{39}Ar spike with a moderate increase of the rate open, in which case the pile up would not be a limiting factor and thus, it would be possible to run with a DAQ window long enough to include the full length of S2 signals. Therefore, the failure of this feasibility study for the ^{39}Ar spike does not sign the end of every attempt to accumulate the DarkSide-G2 statistics, but it only close one of the possible way to obtain it, returning at the same time a better understanding of the complexity of the DarkSide-50 detector.

Chapter 5

Results and Perspectives

5.1 Results

Before the beginning of this thesis DM was just an exotic and mysterious branch of astroparticle physics. After facing some of the theoretical and experimental aspects of this impervious subject, DM and the technology that aims at its direct detection sound surely more familiar.
During this work the evidences and motivations that lead to speculate about the existence of DM and its possible candidates have been described, followed by an overview of the techniques for its detection. DarkSide-50, the youngest experiment within the family of direct dark matter experiments, plays a central role in this search and of course in the development of this study. The layout with which this experiment is running has been detailed, together with the configuration of the TPC and the way the dual-phase argon technology works.
Data from the firsts months of DarkSide-50 data taking was analyzed starting from the main steps with which `DarkArt` reconstructs the events, followed by a description of the PSD and the background rejection. Particular attention was posed on the radioactive component of the background and on alphas. The alpha distribution, believed to be very easy to isolate, appeared more complex than expected. The method of delayed coincidences (^{214}Bi-Po) was then illustrated and applied to estimate the activity of ^{222}Rn contaminant in the detector. Its value resulted to be 0.74 μBq/kg, but further investigation is needed in order to calculate the efficiency with which ^{214}Bi-Po events are identified, hence the definitive figure of ^{222}Rn activity.

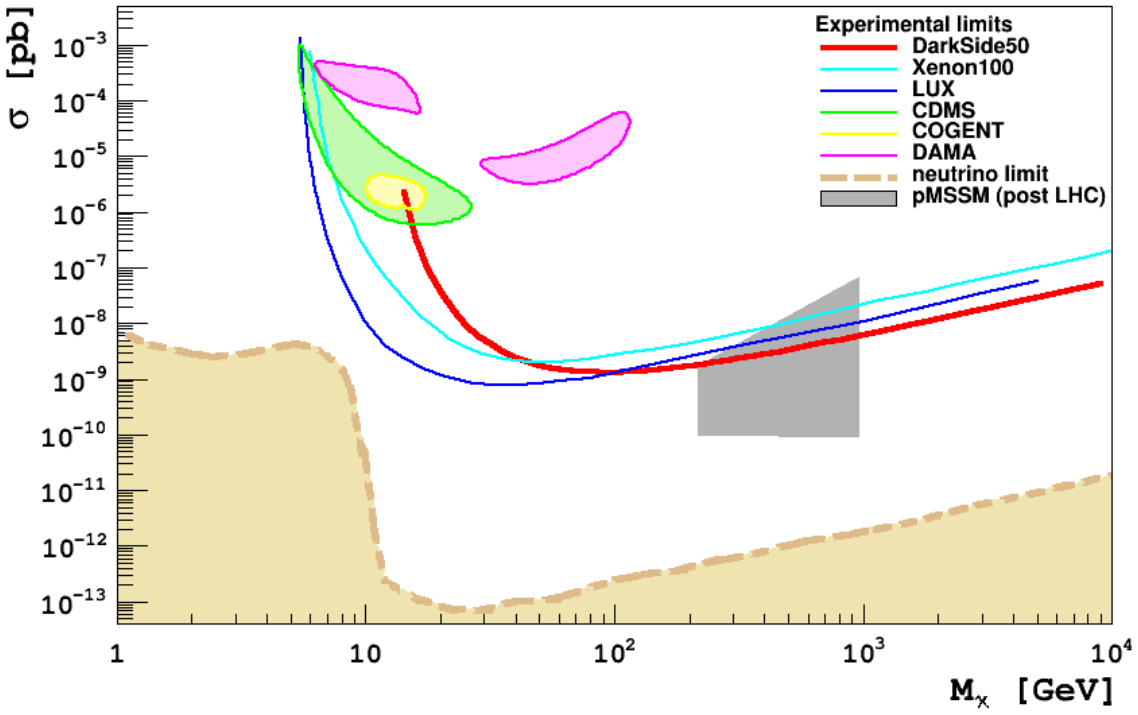

Figure 5.1.1: *Projected sensitivity curve obtain for 2.56 years of exposure for DarkSide-50, compared with the results of other direct dark matter experiments.*

Every new DM experiment aims at the detection of a DM signal or, at least, to set the lowest possible limit in the parameter space (σ, M_W), called exclusion plot. After the analysis of the early data, this thesis walks through all the steps to obtain a projection of the sensitivity curve for DarkSide-50, starting from considerations about WIMP flux and WIMP-nucleon cross section, and ending with the instrumental effects responsible for energy threshold and detection efficiency. In order to compute this sensitivity curve, data from the first 6.3 days of livetime with AAr, corresponding to 2.56 years with UAr have been used. The best sensitivity, reached for WIMP masses around 100 GeV, is approximately 1.3×10^{-45} cm^2.

Lastly, a feasibility study for an ^{39}Ar spike concludes this work. In case of a positive outcome the high statistics accumulated thanks to the ^{39}Ar spike could allow to compute a sensitivity projection for the full statistics of DarkSide-G2 and to probe the PSD of this experiment. However, the presence of unexpected single pulses events, probably caused by Cherekov scintillation in the fused silica or quartz windows, or by alpha particles or caused by TPB scintillation, demonstrated that at

the moment the implementation of an ^{39}Ar spike would not give an outcome comparable with the data obtained by normal running. Nevertheless, the failure of this feasibility study does not completely preclude the possibility of an ^{39}Ar spike, but it limits the system with which obtain it.

5.2 DarkSide-G2

Although DarkSide-50 demonstrates the good outcome of this project on both radioactive background and PSD sides, even better results are expected from the next generation detector.
As already mentioned more than once in this work, DarkSide-50 was designed and built with in mind the upgrade to a multi-ton detector [50] that the collaboration plans to develop in the next 2-3 years. This intermediate phase is not only important for DM search, but it is also crucial to tackle technical issues that, by the time in which DarkSide-G2 will be committed, will be completely solved.
DarkSide-G2 is a LAr-TPC that will be hosed in the already existing LSV and CTF, therefore it will substitute the present TPC. The cryostat will be bigger in order to contain 3.8 tons of liquid UAr as target material and 556 low-background PMTs, 278 each on the top and the bottom. Other features of the future TPC will be very similar to the ones of the TPC already in use, such as the wavelength shifter covering the surface and the fused silica windows covered by ITO, acting as anode/cathode. Again there will be an electric field applied in the TPC in order to have both S1 and S2 signals.
Whereas DarkSide-50 data taking is ongoing, there are, however, few important points to assess for the next phase. Among these, there is the radioactivity that the additional material could introduce in the detector. The main concern comes from the PMTs radiopurity that at the moment does not fulfill the requirements for DarkSide-G2. Thanks to the continuing R&D by Hamamatsu and the careful studies carried on by the DarkSide collaboration, the leading source of radioactivity in the photomultiplier was identified and this problem is on its way to be solved, hence, the needed radiopurity is within reach. Another important point for the future of DarkSide is the extraction and purification of UAr. There are some improvements needed in terms of velocity and efficiency of the process at both the extraction plant and the distillation column that separates the Ar from He and N_2. The goal for

DarkSide-G2 is to reach a production of 50 kg/day and perform the purification with a distillation column directly at Kinder Morgan Doe Canyon facility in Colorado instead that at FNAL.
Finally, DarkSide-G2 will need an exceptional background reduction. The neutron and muon veto can reject completely cosmogenic neutrons, while the surface contamination, due mainly to radioactive daughters of ^{222}Rn will be significantly reduced by carrying out precision cleaning and assembly in the two Rn-suppressed clean rooms. Concerning the rejection of β/γ background, for which PSD plays a key role, even without a dedicated study with the ^{39}Ar spike, early data from DarkSide-50 seems to indicate that the experiment will remain background-free for the full exposure of DarkSide-G2 of 18 tons$\times$year.
In conclusion, when DarkSide-50 will be over, DarkSide-G2 will carry forward the WIMP search exploiting a greater target mass and a very low and well known background. Based on the predicted backgrounds, in 5 years of data taking, DarkSide-G2 will reach, at 90%C.L., a projected sensitivity of 2×10^{-47} cm^2 for 100 GeV WIMPs, as shown in figure 5.2.1, taking the LAr technology to a level never seen before.

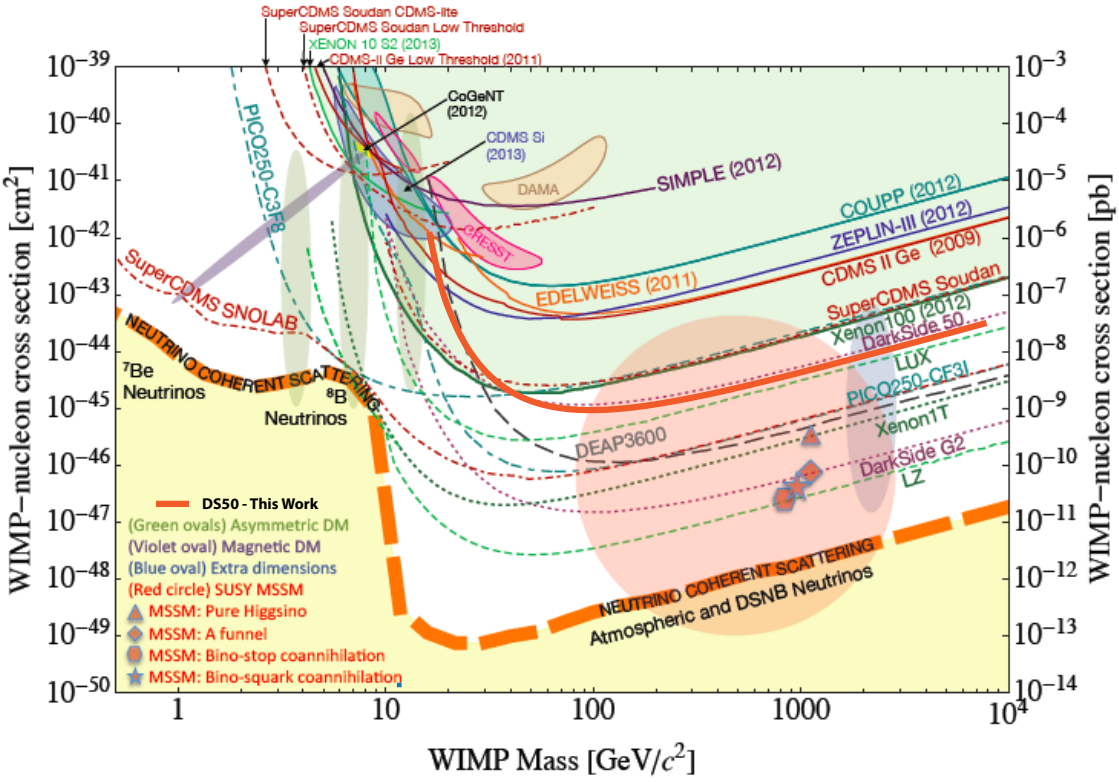

Figure 5.2.1: *Current status of direct dark matter searches results and sensitivity of future experiments. Shaded bounded areas represent claims for dark matter observations or regions of interest compatible with observation of a few events. The red line indicates the sensitivity of DarkSide-50 for an exposure of 2.56 years, obtained with the steps illustrated in this thesis. Among the dashed lines, which show the projected sensitivity of future experiments, is the red dashed line that shows the sensitivity of DarkSide-G2 for zero detected events in 18 tons-years.*

Conclusions

In conclusion, this work of thesis contributes to a better understanding of the detector background. In particular this is the first study of DarkSide-50 α background and radioactive contamination. The dominant and more dangerous contaminants are radon and his daughters. As a result of this study, the ^{222}Rn activity has been estimated to be 0.74μBq/kg, using the identification of ^{214}Bi-Po through the delayed coincidence method.
Using the data acquired during the first 6.3 day of livetime, a projection of DarkSide-50 sensitility has been computed including both theoretical predictions on DM flux and instrumental effects. This projection anticipates that in less than three years DarkSide will reach a sensitivity of the order of 10^{-45} cm^2.
A second study was performed on the feasibility of ^{39}Ar spike (increment of ^{39}Ar in the detector to accumulate statistic). This spike would have allowed to calculate a projected sensitivity for DarkSide-G2 and to prove the PSD performances. Unfortunately, due to unexpected single pulse events, this study lead to the conclusion that it is not possible at the moment to perform the ^{39}Ar spike.

Bibliography

[1] Oort - K. Freeman and G. McNamara, "In Search of Dark Matter." Springer, Berlin, 2006

[2] F. Zwicky, "The Redshift of Extragalactic Nebulae," Hel- vetica Physica Acta, Vol. 6, 1933, pp. 110-127.

[3] J. Feng and M. Trodden, "Dark worlds", Scientific American, 2010

[4] Planck Collaboration et al. "Planck 2013 results. I. Overview and scientific results." In: (mar. 2013). eprint: 1303.5062. url: http://arxiv.org/abs/1303.5062.

[5] V Trimble. "Existence and nature of dark matter in the universe." Annu. Rev. Astron., 25(1):425–472, 1987

[6] S. M. Carrol, "Spacetime and Geometry: An Introduction to General Relativity." San Francisco: Addison Wesley, 2004. Print.

[7] R. Wilson and A. Penzias, "Isotropy of Cosmic Background Radiation at 4080 Megahertz", (1967) Science 156 (3778): 1100–1101.

[8] Planck Collaboration et al. "Planck 2013 results. XVI. Cosmological parameters." In: (mar. 2013). eprint: 1303.5076. url: http://arxiv.org/abs/1303.5076.

[9] L. Bergstrom,J. Edsjo and P. Ullio, arXiv:astro-ph/9902012

[10] H. V. Klapdor- Kleingrothaus and A. Staudt, "Non-accellerator Particle Physics." Institute of Physics Publishing Bristol and Philadelphia, 1995

[11] S. Braibant, G. Giacomelli and M. Spurio, "Particelle e interazioni fondamentali." Springer

[12] K. N. Abazajian at al. , "Light Sterile Neutrino: A White Paper", arXiv:1204.5379v1, 2012

[13] G. Bertone, "Particle Dark Matter: Observations, Models and Searches." Cambridge, UK: Cambridge UP, 2010. Print.

[14] B. Dutta, "Dark Matter Searches at Accelerator Facilities." In: (mar. 2014). eprint: 1403.6217v1. url: http://arxiv. org/abs/1403.6217v1

[15] ATLAS collaboration, "Observation of a New Particle in the Search for the Standard Model Higgs Boson with the ATLAS Detector at the LHC", (2012) Physics Letters B 716 (1): 1–29. arXiv:1207.7214

[16] J. Beringer et al. "Particle Data Group", Phys. Rev. D 86, 010001 (2012)

[17] D. R. Smith and N. Weiner, Phys. Rev. D 64, 043502 (2001), arXiv:hepph/0101138

[18] H. Ziaeepour, "Searching the footprint of wimpzillas", Astroparticle Physics 16 (2001) 101-120

[19] I. Albuquerque and L Baudis, "Direct Detection Constraints on Superheavy Dark Matter", Phys.Rev.Lett. 90 (2003) 221301

[20] J. D. Lewin and P. F. Smith, "Review of Mathematics, Numerical Factors, and Corrections for Dark Matter Experiments Based on Elastic Nuclear Recoil." Astroparticle Physics 6.1 (1996): 87-112. Print.

[21] B.M.Loer, "Towards a depleted argon time projection chamber WIMP search: DarkSide Prototype analysis and predicted sensitivity", Doctoral Thesis, Princeton University (nov. 2011)

[22] S. Matarrese, V. Gorini, and U. Moschella. "Dark Matter and Dark Energy." Dordrecht: Springer, 2011. Print.

[23] R.W. Schnee, "Introduction to dark matter experiments", arXiv:1101.5205v1 [astro-ph.CO], 2011

[24] PNNL: CoGeNT Dark Matter Experiment. url: http://cogent. pnnl.gov

[25] R.Bernabei et al. "DAMA/LIBRA results and prospectives", arXiv:1301.6243v1 [astro-ph.GA], 2013, The DAMA Project. url: http://people.roma2.infn.it/ dama/ web/home.html

[26] Super Cryogenic Dark Matter Search. url: http://cdms.berkeley. edu

[27] EDELWEISS - Experiment for direct detection of dark matter. url: http://edelweiss.in2p3.fr

[28] CDMS Collaboration et al. "Dark Matter Search Results Using the Silicon Detectors of CDMS II". In: (apr. 2013). eprint: 1304.4279. url: http://arxiv.org/abs/1304.4279

[29] CRESST - Searching for Dark Matter. url: http://www.cresst.de/ index.php

[30] XENON100 Collaboration et al. "Dark Matter Results from 225 Live Days of XENON100 Data". In: (lug. 2012). eprint: 1207.5988. url: http://arxiv.org/abs/1207.5988

[31] LUX Collaboration et al. "First results from the LUX dark matter experiment at the Sanford Underground Research Facility." In: (oct. 2013) eprint:1310.8214v2. url: http:// arxiv.org/abs/1310.8214v2

[32] S.P. Ahlen et al. "Study of penetrating cosmic ray muons and search for large scale anisotropies at the Gran Sasso Laboratory". In: Physics Letters B 249.1 (1990), pp. 149–156. issn: 0370-2693.

[33] T. Doke, K. Masuda and E. Shibamura, "Estimation of absolute photon yields in liquid argon and xenon for relativistic (1 MeV) electrons". In: Nuclear Instruments and Methods in Physics Research Section A: Accelerators, Spectrometers, Detectors and Associated Equipment 291.3 (1990), pp. 617–620. issn: 0168-9002

[34] W. H. Lippincott et al. "Scintillation time dependence and pulse shape discrimination in liquid argon", arXiv:0801.1531v4 [nucl-ex], 201

[35] M.G. Boulay and A. Hime, Astropart. Phys. 25, 179 (2006)

[36] P. Benetti et al. "Measurement of the specific activity of 39Ar in natural argon". In: Nuclear Instruments and Methods in Physics Research Section A: Accelerators, Spectrometers, Detectors and Associa- ted Equipment 574.1 (2007), pp. 83–88. issn: 0168-9002.

[37] C. Galbiati e R. Purtschert. "Discovery of underground argon with low level of radioactive 39Ar and possible applications to WIMP dark matter detectors". (dic. 2007). eprint: 0712.0381

[38] H.O. Back et al. "Depleted Argon from Underground Sources". In: Physics Procedia 37 (2012). Proceedings of the 2nd International Conference on Technology and Instrumentation in Particle Physics (TIPP 2011), pp. 1105–1112. issn: 1875-3892

[39] T.Alexander et al. (SCENE Collaboration), "Observation of the Dependence of Scintil lation from Nuclear Recoils in Liquid Argon on Drift Field", arXiv:1306.5675 (2013)

[40] L. Grandi, University of Pavia, Doctoral Thesis, pages 178-179 (2005)

[41] G. Alimonti et al. [Borexino Collaboration], Astropart. Phys. 8, 141 (1998)

[42] G. Alimonti et al. [Borexino Collaboration], Nucl. Instrum. Meth. A 600, 568 (2009)

[43] R. Greenwood and N. R. Chellew, Rev. Sci. Instrum. 50, 466 (1979)

[44] M. C. Smith, et al., Monthly Notices of the Royal Astronomical Society 379, 755 (2007), ISSN 1365-2966, url: http://dx.doi.org/10.1111/j.1365-2966.2007.11964.x

[45] C. Savage, et al., Journal of Cosmology and Astroparticle Physics 2009, 036 (2009), url: http://stacks.iop.org/1475-7516/2009/i=09/a=036

[46] R. H. Helm, Phys. Rev. 104, 1466 (1956)

[47] W. H. Lippinco et al. microCLEAN at Yale, Phys. Rev. C78.035801 (2008)

[48] DarkSide Collaboration, G2 proposal for NSF and DOE (nov. 2013)

[49] T. Pollmann, M. Boulay and M. Kuzniak, "Scintillation of this tetraphenyl butadiene films under apha particle excitation". arXiv:1011.1012v1 [physics.ins-det], (2010)

[50] DarkSide Collaboration, "The DarkSide multi-ton detector for the direct dark matter search", submitted to the journal "Advances in High Energy Physics" (2014)

Acknowledgment

This is probably unusual, but foremost, I would like mention and thank my high school math and physics teacher, Prof. Lucia Nasoni. Without the great enthusiasm for science that she transmit to me during my last year of high school, there will be no thesis on DarkSide to read, but instead I would probably be working in some hospital or trying to give my lasts exams for medical school. Sometimes it is incredible how such a little choice can change your entire existence.
Then, I would like to express my sincere gratitude to my advisors Prof. Stefano Maria Mari and Prof. Luca Grandi, Stefano for the continuous support during my career, starting from my bachelor thesis up to now, for his patience, motivation and enthusiasm for the astroparticles; Luca for his careful guidance into the world of data analysis, his suggestions during the drafting of this thesis and his immense knowledge from which I benefited. Besides my advisors, I would like to thank the rest of the DarkSide collaboration, starting from Cristiano Galbiati who introduced me into this experiment, Peter Mayer and the rest of the Princeton Group. A particular thanks goes to Jason who guided me in the first steps of this adventure, and tutored me until I was able to walk with my legs; and also a special thank to all the people from LNGS with who I spent a wonderful time at Assergi. I found into this collaboration admirable guides, colleagues and friends and I'm glad for their encouragement and insightful comments.
My sincere thanks also goes to my friends Federica, Martina and Flavia, for all the time spent together around a table with piles of books and notes and cups of tea, and to Andrea, my companion of adventure into the universe of dark matter. Last but not the least, I would like to thank my family: my parents Luciana and Giorgio, for giving birth to me at the first place and supporting me spiritually throughout my life, for tolerate my mood swings and for being such wonderful people.